

¹ Study of the multi-strange resonance $\Xi(1530)^0$ production
² with ALICE at the LHC energies

³ Jihye Song

4 Contents

5	List of Figures	4
6	List of Tables	8
7	1 The physics of relativistic heavy-ion collisions	9
8	1.1 Standard model	9
9	1.2 QCD and Quark-Gluon plasma	10
10	1.3 Heavy Ion Collisions	15
11	2 Theoretical models	17
12	2.1 Statistical-Thermal model	17
13	2.1.1 Calculations	19
14	2.1.2 Results and comparison with data	21
15	2.2 EPOS, UrQMD	23
16	3 Production of resonance with strangeness	25
17	3.1 Strange quark and hyperons	27
18	3.2 Resonance production	29
19	4 A Large Ion Collider Experiment at the LHC	31
20	4.1 The Large Hadron Collider	31
21	4.2 The ALICE project	34
22	4.2.1 ALICE detector	34
23	4.2.2 Data Acquisition (DAQ) and trigger system	44
24	4.2.3 ALICE offline software frame work	46
25	5 Measurement of $\Xi(1530)^0$ production in p-Pb and Pb-Pb	48
26	5.1 $\Xi(1530)^0$ -reconstruction	48
27	5.1.1 Data sample and event selection	48
28	5.1.2 Track and topological selection	52
29	5.1.3 Particle identification	55
30	5.1.4 Signal extraction	58
31	5.2 Efficiency correction	67
32	5.3 Corrected p_T -spectra	70
33	5.4 Systematic uncertainties	72
34	5.5 $\Xi(1530)^0$ transverse momentum spectra	77
35	6 Further results and discussion	80
36	6.1 Mean transverse momentum	80
37	6.2 Particle yield ratios	84

38	6.2.1 Integrated yield ratios of excited to ground-state hadrons	84
39	6.3 Integrated yield ratios to pion	87
40	References	91

41 **List of Figures**

42 1	QCD coupling constant as a function of momentum transfer. Experimental 43 data and also theoretical prediction are presented. [1]	13
44 2	Hydrodynamic evolution of a heavy ion collision with and without the for- 45 mation of a QGP.	15
46 3	Grand canonical thermal fit of 0-10% central Pb-Pb collisions, with 3 models 47 (THERMUS, GSI, SHARE).	17
48 4	Ratio of baryonic and mesonic resonances over their stable partner as a 49 function of temperature.	22
50 5	Ratio of resonances over their stable partner as a function of $\sqrt{(s)}$	23
51 6	The $J^P = 1/2^+$ ground state baryon octet	26
52 7	The $J^P = 3/2^+$ baryon decuplet	26
53 8	Enhancements in the rapidity range $ y < 0.5$ as a function of the mean 54 number of participants $\langle N_{part} \rangle$, showing LHC (ALICE, full symbols), RHIC 55 and SPS (open symbols) data. Boxes on the dashed line at unity indicate 56 statistical and systematic uncertainties on the pp or p-Be reference. Error 57 bars on the data points represent the corresponding uncertainties for all the 58 heavy-ion measurements and those for p-Pb at the SPS.	28
59 9	Hadronic phase	29
60 10	The CERN accelerator complex [2]	32
61 11	The ALICE detector	36
62 12	Schematic view of the ITS [3]	37
63 13	Track impact parameter resolution in the transverse plane ($r\phi$) vs p_T for 64 charged particle	38
65 14	Schematic view of the TPC	39
66 15	Specific energy loss (dE/dx) in the TPC vs. particle momentum in Pb-Pb 67 collisions at $\sqrt{s_{NN}} = 2.76$ TeV. The lines show the parametrisations of the 68 expected mean energy loss.	40
69 16	Correlation between the sum and difference of signal times in V0A and V0C. 70 Three classes of events collisions at (8.3 ns, 14.3 ns), background from Beam 71 1 at (-14.3 ns, -8.3 ns), and background from Beam 2 at (14.3 ns, 8.3 ns) 72 can be clearly distinguished.	42
73 17	Distribution of the V0 amplitude (sum of V0A and V0C in top, V0A in 74 bottom). The inset shows a magnified version of the most peripheral region.	43
75 18	The overall architecture of the ALICE DAQ and the interface to the HLT 76 system.	44
77 19	Schematic view of the AliRoot framework	47
78 20	Vertex-z coordinate distribution of the accepted events in p-Pb collision(Left) 79 and in Pb-Pb collisions(Right). The red dashed line indicates vertex cut .	50

80	21	Multiplicity distribution of accepted events in p–Pb collision in percentile. The each color and labels define the four intervals in which the analysis is performed.	50
81	22	Centrality distribution of three different trigger classes.	51
82	23	Sketch of the decay modes for Ξ^{*0} and depiction of the track and topological selection criteria.	53
83	24	TPC dE/dx as function of transverse momentum for total (top) and selected first emitted π in 3σ (bottom)	55
84	25	TPC dE/dx as function of transverse momentum for total (top) and selected second emitted π in 3σ (bottom)	55
85	26	TPC dE/dx as function of transverse momentum for total (top) and selected last emitted π in 3σ (bottom)	56
86	27	TPC dE/dx as function of transverse momentum for total (top) and selected proton in 3σ (bottom)	56
87	28	TPC dE/dx as function of transverse momentum for total (top) and selected first emitted π in 3σ (bottom)	56
88	29	TPC dE/dx as function of transverse momentum for total (top) and selected second emitted π in 3σ (bottom)	57
89	30	TPC dE/dx as function of transverse momentum for total (top) and selected last emitted π in 3σ (bottom)	57
90	31	TPC dE/dx as function of transverse momentum for total (top) and selected proton in 3σ (bottom)	58
91	32	The $\Xi^\mp\pi^\pm$ invariant mass distribution (Same-event pairs) in $1.8 < p_T < 2.2 \text{ GeV}/c$ and for the multiplicity class 20-40%. The background shape, using pairs from different events (Mixed-event background), is normalised to the counts in $1.49 < M_{\Xi\pi} < 1.51 \text{ GeV}/c^2$ and $1.56 < M_{\Xi\pi} < 1.58 \text{ GeV}/c^2$	59
92	33	The $\Xi^\mp\pi^\pm$ invariant mass distribution (Same-event pairs) in $3.0 < p_T < 3.5 \text{ GeV}/c$ and for the centrality class 0-10%. The background shape, using pairs from different events (Mixed-event background), is normalised to the counts in $1.49 < M_{\Xi\pi} < 1.51 \text{ GeV}/c^2$ and $1.56 < M_{\Xi\pi} < 1.58 \text{ GeV}/c^2$	60
93	34	The invariant mass distribution after subtraction of the mixed-event background in p–Pb collisions. The solid curve represents the combined fit, while the dashed line describes the residual background.	61
94	35	The invariant mass distribution after subtraction of the mixed-event background in Pb–Pb collisions. The solid curve represents the combined fit, while the dashed line describes the residual background.	62
95	36	σ fit parameters as a function of p_T in MB in p–Pb collisions (top) and in Pb–Pb collisions (bottom).	64
96	37	$\Xi(1530)^0$ -mass obtained from fit of the Voigtian peak as a function of p_T in each multiplicity classes in p–Pb collisions (top) and the different centrality classes in Pb–Pb (bottom).	65

121	38	$\Xi(1530)^0$ -raw spectra obtained from fit of the Voigtian peak and a polynomial residual background for different multiplicities in p–Pb collisions (top) and Pb–Pb collisions (bottom). Only the statistical error is reported.	66
122			
123	39	$\Xi(1530)^0$ -raw spectra obtained from fit of the Voigtian peak and a polynomial residual background for different multiplicities. Only the statistical error is reported.	67
124			
125	40	Real corrected $\Xi(1530)^0$ spectrum (black) for the minimum bias with Levy fit (black curve). Also shown are the unweighted generated (blue) and reconstructed (red) $\Xi(1530)^0$ spectra.	68
126			
127	41	Efficiency as a function of p_T in minimum bias events in p–Pb collisions.	69
128			
129	42	Efficiency as a function of p_T in different centrality classes in Pb–Pb collisions	70
130			
131	43	Corrected p_T -spectra of $\Xi(1530)^0$ in NSD and different multiplicity classes in p–Pb collisions.	71
132			
133	44	Corrected p_T -spectra of $\Xi(1530)^0$ in different centrality classes in Pb–Pb collisions.	71
134			
135	45	Summary of the contributions to the systematic uncertainty in minimum bias events in p–Pb collisions. The dashed black line is the sum in quadrature of all the contributions.	75
136			
137	46	Systematic uncertainties for each multiplicity classes in p–Pb collisions.	75
138			
139	47	Summary of the contributions to the systematic uncertainty in minimum bias events in Pb–Pb collisions. The dashed black line is the sum in quadrature of all the contributions.	76
140			
141	48	Systematic uncertainties for each multiplicity classes.	76
142			
143	49	Corrected yields as function of p_T in NSD events and multiplicity dependent event classes in p–Pb collision system. Statistical uncertainties are presented as bar and systematical uncertainties are plotted as boxes.	78
144			
145	50	Corrected yields as function of p_T in different centrality classes in Pb–Pb collision system. Statistical uncertainties are presented as bar and systematical uncertainties are plotted as boxes.	79
146			
147	51	Mean transverse momenta $\langle p_T \rangle$ of Λ , Ξ^- , $\Sigma^{*\pm}$, Ξ^{*0} and Ω^- in p–Pb collisions at $\sqrt{s_{NN}} = 5.02$ TeV as a function of mean charged-particle multiplicity density $\langle dN_{\text{ch}}/d\eta_{\text{lab}} \rangle$, measured in the pseudorapidity range $ \eta_{\text{lab}} < 0.5$. The results for Λ , Ξ^- and Ω^- are taken from [4, 5, 6]. Statistical and systematic uncertainties are represented as bars and boxes, respectively. The Ω^- and Ξ^- points in the 3rd and 4th lowest multiplicity bins are slightly displaced along the abscissa to avoid superposition with the $\Xi(1530)^0$ points.	81
148			
149			
150			
151			
152			
153			
154			
155			
156			

157	52	Mass dependence of the mean transverse momenta of identified particles for the 0 – 20% V0A multiplicity class and with $-0.5 < y_{\text{CMS}} < 0$ in p– Pb collisions at $\sqrt{s_{\text{NN}}} = 5.02$ TeV [4, 6], and in minimum-bias pp collisions at $\sqrt{s} = 7$ TeV [7] with $ y_{\text{CMS}} < 0.5$. Additionally, D^0 and J/ψ results are plotted. The D^0 and J/ψ were measured in different rapidity ranges: $ y_{\text{CMS}} < 0.5$ [8] ($ y_{\text{CMS}} < 0.9$ [9]) for D^0 (J/ψ) in pp and $-0.96 < y_{\text{CMS}} <$ 0.04 [8] ($-1.37 < y_{\text{CMS}} < 0.43$ [10]) for D^0 (J/ψ) in p–Pb. Note also that the results for D^0 and J/ψ in p–Pb collisions are for the 0–100% multiplicity class.	82
166	53	Ratio of $\Xi(1530)^0$ to Ξ^- measured in pp [7], p–Pb [4, 6] and Pb–Pb collisions as a function of $\langle dN_{\text{ch}}/d\eta_{\text{lab}} \rangle$ measured at midrapidity. Statistical uncer- tainties (bars) are shown as well as total systematic uncertainties (hollow boxes) and systematic uncertainties uncorrelated across multiplicity (shaded boxes). A few model predictions are also shown as lines at their appropriate abscissa.	85
172	54	Ratio of $\rho/\pi(\text{Up})$, K^*/K , $\phi/K(\text{Left bottom})$ and Λ^*/Λ with system size measured at mid-rapidity. Statistical uncertainties (bars) are shown as well as total systematic uncertainties (hollow boxes) and systematic uncertainties uncorrelated across multiplicity (shaded boxes). A few model predictions are also shown as lines at their appropriate abscissa.	86
177	55	Ratio of $\Xi(1530)^0$ to π^\pm , measured in pp [11] and p–Pb [7] collisions, as a function of the average charged particle density ($\langle dN_{\text{ch}}/d\eta_{\text{lab}} \rangle$) measured at mid-rapidity. Statistical uncertainties (bars) are shown as well as total systematic uncertainties (hollow boxes) and systematic uncertainties uncor- related across multiplicity (shaded boxes). A few model predictions are also shown as lines at their appropriate abscissa.	88
183	56	Particle yield ratios to pions of strange and multi-strange hadrons normal- ized to the values measured in pp collisions, both in pp and in p–Pb colli- sions. The common systematic uncertainties cancel in the double-ratio. The empty boxes represent the remaining uncorrelated uncertainties. The lines represent a simultaneous fit of the results with the empirical scaling formula in Equation ???.	89
189	57	p_{T} -integrated yield ratios of strange and multi-strange hadrons to $(\pi^+ + \pi^-)$ as a function of $\langle dN_{\text{ch}}/d\eta_{\text{lab}} \rangle$ measured in the rapidity interval $ \eta < 0.5$. The empty and dark-shaded boxes show the total systematic uncertainty and the contribution uncorrelated across multiplicity bins, respectively. The values are compared to calculations from MC models and to results obtained in Pb–Pb and p–Pb collisions at the LHC.	90

¹⁹⁵ **List of Tables**

196	1	Constituents of matter in the Standard Model	9
197	2	Fundamental forces	10
198	3	Parameters used in the thermal-model calculations.	18
199	4	Properties of particles used in the ratio calculations.	20
200	5	Difference of mass (ΔM), baryon number (ΔB), strangeness (ΔS) and charge (ΔQ) of the ratios.	21
201	6	Quantum numbers and masses associated to the three lighter quarks: u, d and s	25
202	7	Lifetime of hadronic resonances	27
203	8	Number of accepted and analyzed events per multiplicity/centrality interval	52
204	9	Track selections common to all decay daughters and primary track selections applied to the charged pions from decays of Ξ^{*0}	52
205	10	Topological and track selection criteria.	53
206	11	Summary of the systematic uncertainties on the differential yield, $d^2N/(dp_T dy)$. Minimum and maximum values in all p_T intervals and multiplicity classes in p–Pb, centrality classes in Pb–Pb are shown for each source.	77

212 **1 The physics of relativistic heavy-ion collisions**

213 The main objective of relativistic heavy ion physics is to study the nuclear matter under
 214 extreme conditions which are high temperature and energy density. In these conditions,
 215 the Standard Model anticipates that the nuclear matter undergo a new phase, where the
 216 quarks and the gluons are expected to be de-confined called quark-gluon plasma (QGP)
 217 and to freely move.

218 **1.1 Standard model**

219 If one have question "what the world is made of", our current answer to the question is
 220 Standard Model (SM) families [12] reported in Table 1. The SM explains the way how
 221 those basic blocks of matter interact and how they are ruled by four fundamental forces.
 222 In this explanation, the matter consist of 12 particles, which have a spin of 1/2 (fermions)
 223 and can be categorized in accordance with way how they interact or equivalently to what
 224 charges they carry. The basic particles are six quarks (up, down, charm, strange, top and
 225 bottom) that carry fractional charge of $+\frac{2}{3}e$ or $-\frac{1}{3}e$, and six leptons (electron, electron
 226 neutrino, muon, muon neutrino, tau, tau neutrino) with integer charge.

Family	Quarks			Leptons		
	Name	Charge[e]	Mass	Name	Charge[e]	Mass
1	u	2/3	$2.2^{+0.6}_{-0.4}$ MeV/c ²	e^-	-e	0.511 MeV/c ²
	d	-1/3	$4.7^{+0.5}_{-0.4}$ MeV/c ²	ν_e	0	< 2 eV/c ²
2	c	2/3	$1.27^{+0.03}$ GeV/c ²	μ^-	-e	105.66 MeV/c ²
	s	-1/3	96^{+8}_{-4} MeV/c ²	ν_μ	-e	< 0.19 eV/c ²
3	t	2/3	173.21 ± 1.22 GeV/c ²	τ^-	-e	1.777 GeV/c ²
	b	-1/3	$4.18^{+0.04}_{-0.03}$ GeV/c ²	ν_τ	-e	< 18.2 MeV/c ²

Table 1: Constituents of matter in the Standard Model

227 The interactions between elementary particles are described by the exchange of gauge
 228 bosons(gluon, photon, Z-boson, W-boson), reported in Table 2 together with their relative
 229 coupling strengths. The leptons are governed the weak force and the electromagnetic force.
 230 Quarks have color property which is the character of charge in the strong force. The color
 231 could take one out of three possible values (conventionally red, green and blue). The color
 232 can not be appeared freely. After they are confined they come out in the form of hadron
 233 which are colorless. Further explaination on color is described in Section 1.2. Then, the
 234 hadrons are grouped into baryon and mesons. Baryons consist of three quarks, qqq or $(\bar{q}\bar{q}\bar{q})$
 235 while mesons consist of two quarks ($q\bar{q}$).

236 The models that describe these interactions are listed as follows:

237

Force	Strength	Gauge Boson(s)	Applies on
Strong force	1	8 Gluons(g)	Quarks, gluons
Electromagnetic force	$\simeq 10^{-2}$	Photon (γ)	All charged particles
Weak force	$\simeq 10^{-7}$	W^\pm, Z^0	Quarks, leptons
Gravitation	$\simeq 10^{-39}$	Gravitons	All particles

Table 2: Fundamental forces

238 **Quantum Electro-Dynamics (QED)** is a quantum field theory of the electromagnetic
 239 force and describes how light and matter interact. This is the first theory where
 240 full agreement between quantum mechanics and special relativity is achieved. It explains
 241 mathematically not only all interactions of light with matter but also those of charged
 242 particles with one another.

243
 244 **Electroweak Theory (EW)** is the unified description of two of the four known fundamental
 245 interactions of nature: electromagnetism and the weak interaction. The first
 246 measurement of the existence of the weak bosons W^+ , W^- and Z^0 was performed in 1983,
 247 when they were produced and directly observed in $Spp\bar{S}$ collisions at CERN.

248
 249 **Quantum Chromo-dynamics (QCD)** is the theory of the strong interaction (color
 250 force), describing the interactions between quarks and gluons which make up the hadrons.
 251 Starting from the classification of the large amount of particles discovered during the fifties,
 252 the original idea of the quark model by Gell-Mann (Nobel Prize in 1969) has been developed
 253 during the sixties until 1973, when David J. Gross, H. David Politzer and Frank Wilczek
 254 discovered the asymptotic freedom property of the strong nuclear interaction.

255 1.2 QCD and Quark-Gluon plasma

256 As the number of known particle species became large, the idea that these could be the
 257 elementary constituents of matter was replaced by the notion that these species could in
 258 fact be composite objects made up of fewer, more elementary particles, in a similar way to
 259 what had already happened to the elements of Mendeleev's Periodic Table. The original
 260 idea by Gell-Mann (1964) was that the hadrons could be obtained as combination of the
 261 fundamental representation of an $SU_f(3)$ group, where three different flavors of quark (q
 262 = u, d, s) combine to build mesons ($q\bar{q}$) and hadrons (qqq). However, when cataloging
 263 hadrons using the $SU_f(3)$ group, there are anomalous states, such as the $\Omega^-(sss)$ and the
 264 $\Delta^{++}(uuu)$, that are combinations of three quarks of the same flavor, in clear contrast
 265 with the Pauli exclusion principle for fermions. A solution was proposed in 1965 by Moo-
 266 Young Han with Yoichiro Nambu and Oscar W. Greenberg, who independently solved the
 267 problem by proposing that quarks possess an additional $SU(3)$ gauge quantum number,

268 later called color charge. This new quantum number may assume three states, represented
 269 by the three primary colors: red, green and blue (denoted symbolically by R, G and B,
 270 respectively). The introduction of this new quantum number also provides an explanation
 271 to other empirical evidence, such as the fact that no qq , $\bar{q}q$ or the single quark have never
 272 been observed directly. On the other hand, the existence of color charge gives rise to the
 273 possible existence of differently colored states for each particle. Thus, we could have many
 274 states for the proton, such as $u_R u_G d_B$, $u_R u_G d_G$, $u_B u_R d_R$, and so on. The fundamental
 275 rule that solves such contradictions is that all the particle states observed in nature are
 276 "colorless" or "white" (or, to be more precise, unchanged under $SU_c(3)$ rotations). The
 277 dynamics of the quarks and gluons are controlled by the gauge invariant QCD Lagrangian:

$$\mathcal{L}_{QCD} = \underbrace{i\delta_{ij}\bar{\Psi}_q^i\gamma^\mu\partial_\mu\Psi_q^j}_{\mathcal{L}_1} + \underbrace{g_s\bar{\Psi}_q^i\gamma^\mu t_{ij}^a A_\mu^a\Psi_q^j}_{\mathcal{L}_2} + \underbrace{m_q\bar{\Psi}_q^i\Psi_q^j}_{\mathcal{L}_3} + \underbrace{\frac{1}{4}F_{\mu\nu}^a F^{a\mu\nu}}_{\mathcal{L}_4} \quad (1)$$

278 where the coloured gluon field tensor, $F_{\mu\nu}^a$ (with color index a) and the squared gauge
 279 coupling parameter, g_s^2 (associated to the strong coupling constant α_s) are defined as:

$$F_{\mu\nu}^a = \partial_\mu A_\nu^a - \partial_\nu A_\mu^a + g_s f^{abc} A_\mu^b A_\nu^c \quad (2)$$

280 and

$$g_s^2 = 4\pi\alpha_s \quad (3)$$

281 where:

- 282 • Ψ_q^i : the quark field with flavor q and color index $i \in [1;3]$, such as $\Psi_q = (\Psi_{qR}, \Psi_{qG},$
 283 $\Psi_{qB})^T$ and A_μ^a is the gluon field with color index a (adjoint representation)
- 284 • γ^μ : Dirac matrices that express the vector nature of the strong interaction, with μ
 285 being the Lorentz vector associated index
- 286 • m_q : quark mass, a priori not equal to zero (resulting from the Higgs mechanism or
 287 equivalent)
- 288 • t_{ij}^a : generator matrices of the group $SU_c(3)$, proportional to the Gell-Mann matrices,
 289 that perform revolutions in color space, representing interaction of quarks and gluons
- 290 • f^{abc} : structure constant of QCD

291 Each of the four terms of the QCD Lagrangian expresses and aspect of the interaction,
 292 specifically:

- 293 • \mathcal{L}_1 : gives the kinetic energy of the quark field Ψ_q^i

- 294 • \mathcal{L}_2 : gives the interaction between quarks (fermions) and gluons (the bosons of the
295 interaction)

- 296 • \mathcal{L}_3 : gives the mass of the quarks

- 297 • \mathcal{L}_4 : gives the kinetic energy of the gluons

298 The terms of this equation, together with the fundamental parameters α_s and m_q ,
299 summarize in just one expression all the features of the strong interaction. The first three
300 terms describe the free propagation of quarks and gluons and the quark-gluon interaction.
301 The remaining two terms show the presence of three and four gluon vertices in QCD and
302 reflect the fact that gluons themselves carry color charge. This is a consequence of the non-
303 abelian⁴ character of the gauge group. This peculiarity of the QCD interaction imposes the
304 evolution of the strong coupling constant, α_s . The corresponding trend has been measured
305 experimentally, and compared in Figure 1 with predictions. A practical consequence of
306 this behavior is that the corresponding potential has a completely different shape than the
307 other fundamental interactions and can be expressed by the following equation:

$$V(r) = -4 \frac{\alpha_s}{3r} + kr \quad (4)$$

308 where r is the separation distance between the two quarks and k is a constant that is
309 approximately 1 GeV/fm.

310 Three are main properties of the QCD interaction:

312 **Confinement** At large distances between quarks and gluons (i.e. small values of trans-
313 ferred momentum Q in Figure 1) the coupling constant is large and the associated force
314 is strong enough to keep these elementary con- stituents (usually called partons) confined
315 in bounded states. As expressed in the Equation 4, the attractive potential increases with
316 the increasing of the relative distance between the two partons preventing the separation
317 of an individual quark or gluon. This explains the meaning of the term "confinement"
318 adopted to describe this energy regime. From the theoretical point of view, the large value
319 of α_s make impossible any perturbative approach in the solution of the Hamilton equation
320 of the system. A successful solution is to perform the study of the system on a discrete
321 space. Such techniques are known as lattice QCD and are based on numerical Monte Carlo
322 simulations. The challenge for the calculations is to reduce the lattice spacing in order to
323 approach the continuum.

324 **Asymptotic freedom** Reducing the distance between quarks and gluons (i.e. increas-
325 ing Q in Figure 1) the coupling constant α_s becomes smaller. As anticipated, this is a
326 unique feature among the forces and comes from the non-abelian nature of the QCD gauge
327 symmetry. Such a phenomenon is also depicted by the weakening of the anti-screening
328 effect of the surround- ing virtual gluons with decreasing distance. In this way two quarks

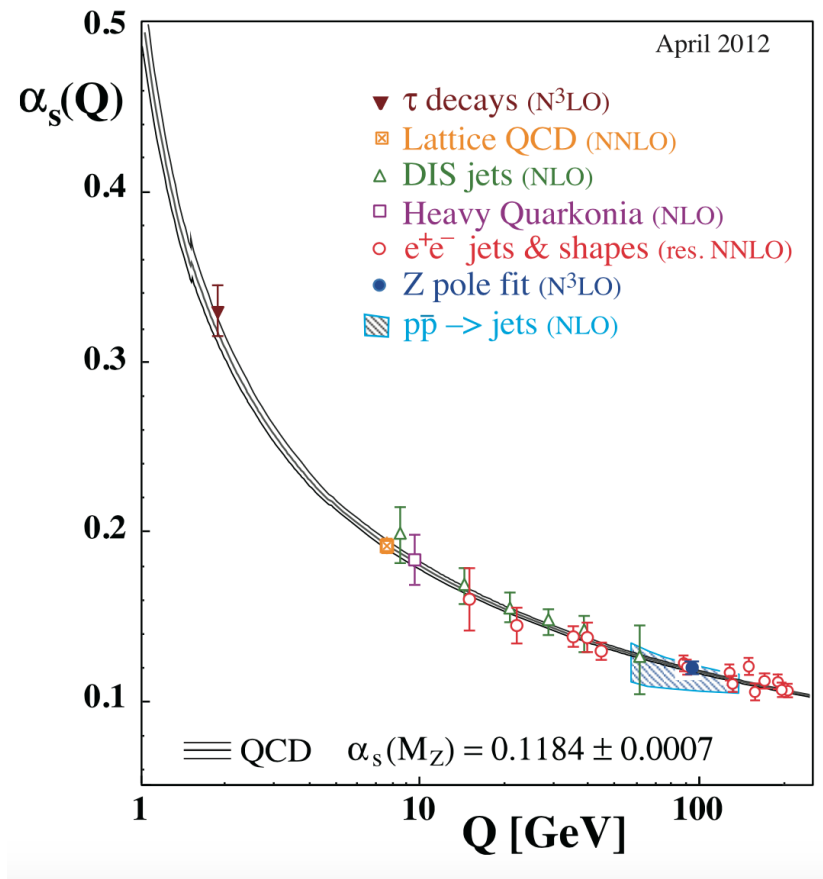


Figure 1: QCD coupling constant as a function of momentum transfer. Experimental data and also theoretical prediction are presented. [1]

330 closer and closer in space show each other a smaller and smaller color charge.

331

332 **Chiral symmetry** One further property of interest is connected to the chirality of
333 the quark. It can be verified that the QCD lagrangian for massless quarks is invariant
334 under a chiral rotation ($SU_L(N_f) \times SU_R(N_f)$), while the operator $\bar{q}q = \bar{q}_L q_R + \bar{q}_R q_L$ is
335 not invariant (in the axial part), meaning that the mesons (state $\bar{q}q$) should have the same
336 mass. Experimentally this is clearly not true, and it could be shown that the axial current
337 is conserved (PCAC and the Goldberger-Treiman relation). The solution to this puzzle
338 is that the chiral (axial-vector) symmetry is spontaneously broken; this means that the
339 symmetry of the Hamiltonian is not a symmetry of the corresponding ground state. It
340 has also been shown, by G. t'Hooft, that the confinement implies a dynamical breaking
341 of the chiral symmetry. This means that the breaking comes from the interaction between
342 the objects in the system. From this follows that the masses of the quarks are strongly
343 increased because of the interaction with the constituents of the system. This mechanism,
344 known as dynamical chiral symmetry breaking justifies the mass of the hadrons, reducing
345 the role of the Higgs mechanism in the mass explanation at least for the light hadrons.

346 The asymptotic freedom property suggests the existence of a state of matter, called
347 Quark-Gluon Plasma (QGP), in which the constituents of the hadrons are de-confined.

348 1.3 Heavy Ion Collisions

349 In the case a QGP is formed, it will eventually expand because of its internal pressure.
 350 As the system expands it also cools. The space-time evolution of the expansion can be
 351 seen in Figure 2 (right side). A and B represent the two incoming ion beams. After a pre-
 352 equilibrium phase a QGP is formed. As it expands, the system will eventually reach what
 353 is known as the critical temperature (T_c). At this point partons begin to hadronize and this
 354 will continue until the chemical freeze-out (T_{ch}) takes place, when inelastic collisions cease.
 355 At this stage the distribution of hadrons is frozen. As cooling and expansion continue the
 356 hadrons reach what is called thermal freeze out (T_{fo}). Here the elastic collisions stop and
 357 the hadrons carry fixed momenta. The QGP state can not be directly observed, because of
 358 its short lifetime. Instead, through experiment we measure the final state hadrons, which
 359 have a fixed momentum after T_{fo} . The observables of interest should tell us about the
 360 de-confinement and the thermodynamic properties of the matter. Moreover, experimental
 361 measurements include yields and p_T spectra of various particle species, azimuthal studies
 362 of high p_T particles, phase space distributions, and particle correlations.

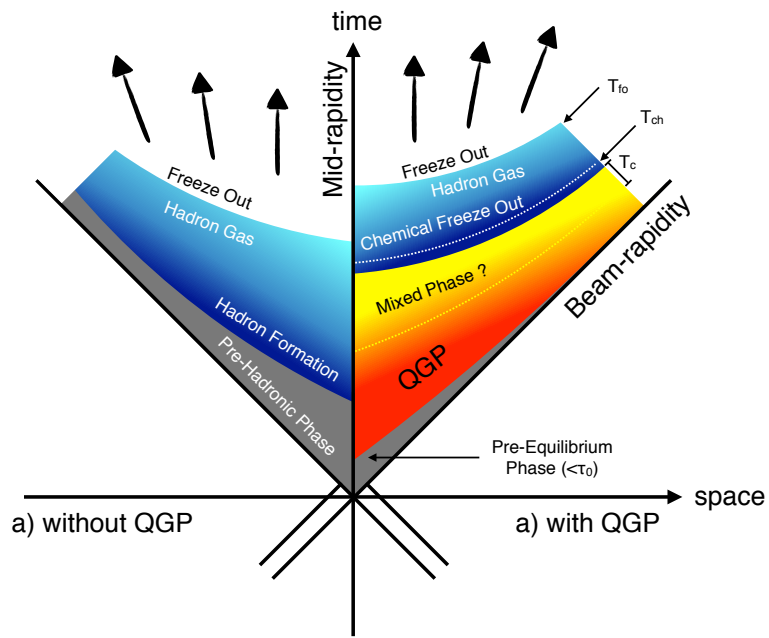


Figure 2: Hydrodynamic evolution of a heavy ion collision with and without the formation of a QGP.

363 A practical way to reach a critical condition in which a nuclear system should undergo

³⁶⁴ a phase transition to the QGP, at high temperature and/or matter density, is to collide
³⁶⁵ two nuclei at sufficiently high energy. Therefore, relativistic and ultra-relativistic heavy-ion
³⁶⁶ collisions are a unique tool to study nuclear matter under extreme conditions.

367 2 Theoretical models

368 2.1 Statistical-Thermal model

369 The statistical-thermal model deal with the fireball created from high energy collisions as
 370 an ideal gas of hadrons including resonances. These hadrons are described by local thermal
 371 distributions at freeze-out with the parameters common to all particle species. The
 372 model has proved successful in applications to relativistic collisions of both heavy ions and
 373 elementary particles. The comparison between prediction and data obtained from Pb–Pb
 374 collisions are shown in Figure 3. In light of this success, THERMUS, a thermal model
 375 analysis package, has been developed for incorporation into the object-oriented ROOT
 376 framework [13].

377

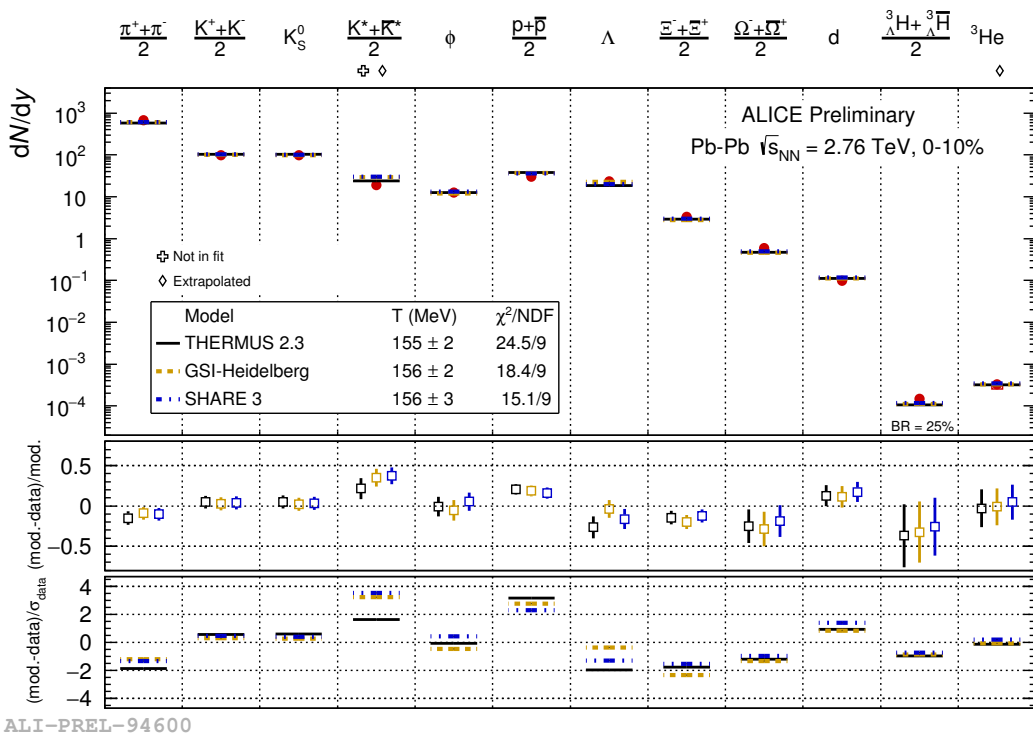


Figure 3: Grand canonical thermal fit of 0-10% central Pb-Pb collisions, with 3 models (THERMUS, GSI, SHARE).

378 There are three types of statistical-thermal models in explaining data in high energy
 379 nuclear physics and THERMUS treats the system quantum numbers B (baryon number),

380 S (strangeness) and Q (charge) within three distinct formalisms:

- 381 1. **Grand-Canonical Ensemble:** Because the hot dense matter produced in nucleus-
382 nucleus collisions is large enough, this ensemble is the most widely used in applica-
383 tions to heavy-ion collisions, in which the quantum numbers or particle numbers are
384 conserved on average through the temperature and chemical potential.
- 385 2. **Fully-Canonical Ensemble:** In which B, S and Q are exactly conserved and this
386 ensemble used in high-energy elementary collisions such as pp, p \bar{p} and e $^-$ e $^+$ collisions.
- 387 3. **Strangeness-Canonical Ensemble:** In heavy-ion collisions, the large numbers of
388 baryons and charged particles generally allows baryon number and charge to be
389 treated grand-canonically. However, in small systems or at low temperatures, a
390 canonical treatment leads to a suppression of hadrons carrying non-zero quantum
391 numbers, since these particles have to be created in pairs and the resulting low pro-
392 duction of strange particles needs a canonical treatment of strangeness. Within this
393 ensemble the strangeness in the system is fixed exactly by its initial value of S, while
394 the baryon and charge content are treated grand-canonically.

395 In order to calculate the thermal properties of a system, the partition function requires to
396 be evaluated. The form of it clearly depends on the choice of ensemble. In the present
397 analysis the strangeness-canonical ensemble used and statistical-thermal model requires six
398 parameters as input: the chemical freeze-out temperature T , baryon and charge chemical
399 potentials μ_B and μ_Q respectively, canonical or correlation radius, R_C ; the radius inside
400 which strangeness is exactly conserved and the fireball radius R . An additional strangeness
401 saturation factor γ_S has been used as indicator of a possible departure from equilibrium
402 and $\gamma_S = 1.0$ corresponds to complete strangeness equilibration.

403 The volume dependence cancels out when studying the particle ratios as well as strangeness
404 canonical equivalent to grand canonical formalism if $\Delta S = 0$ in the ratios and γ_S also can-
405 celes out. Parameters used in the analysis reported in Table 3.

Table 3: Parameters used in the thermal-model calculations.

Parameter	Value
T (MeV)	varied
μ_B (MeV)	0.1
μ_Q (MeV)	0.0
γ_S	1.0

406

407 **2.1.1 Calculations**

408 *Concept:*

409 In order to calculate the particle ratios within strangeness canonical formalism of THER-
410 MUS, temperature varied between 60 MeV to 180 MeV and particle yields extracted for
411 each temperature value and then primary particle ratios calculated for each case.

412

413 *Feed-Down Correction:*

414 Since the particle yields measured by the detectors in collision experiments include feed-
415 down from heavier hadrons and hadronic resonances, the primitive hadrons are allowed to
416 decay to particles considered stable by the experiment before model predictions are com-
417 pared with experimental data. In the analysis only Λ particles counted as stable (do not
418 allowed to decay) so there is no feed-down contribution from these particles to the other
419 ratios.

420

421 Properties of studied particles and their particle ratios listed in Table 4 and Table 5,
422 respectively.

423

424

Table 4: Properties of particles used in the ratio calculations.

Particle	Δ^{++}	Δ^{++}	p	K^{*0}	K^+	Λ^*	Λ	Σ^{*+}	Σ^+	Σ^0	Ξ^{*0}	Ξ^-
Mass (MeV/ c^2)	1232	938.27	895.92	493.67	1519.5	1115.68	1382.8	1189.37	1192.64	1531.80	1321.31	-
Width (MeV/ c^2)	120	-	50.7	-	15.6	-	37.6	-	-	9.1	-	-
$c\tau$ (fm)	1.6	-	3.9	-12.6	-	5.51	-	-	21.6	-	-	-
Ang. Momentum (J)	$3/2$	$1/2$	1	0	$3/2$	$1/2$	$3/2$	$1/2$	$1/2$	$3/2$	$1/2$	$1/2$
Isospin (I)	$3/2$	$1/2$	$1/2$	$1/2$	0	0	1	1	1	$1/2$	$1/2$	$1/2$
Parity (P)	+1	+1	-1	0	-1	+1	+1	+1	+1	+1	+1	+1
Strangeness (S)	0	0	1	1	-1	-1	-1	-1	-1	-2	-2	-2
Baryon Number (B)	1	1	0	0	1	1	1	1	1	1	1	1
Decay Channel	$p\pi^+$	-	π^-	$\mu^+\nu_\mu$	pK^-	$p\pi^-$	$\Lambda\pi^+$	$p\pi^0$	$\Lambda\gamma$	$\Xi^-\pi^+$	$\Lambda\pi^-$	-
Branching Ratio (%)	~ 100	-	~ 66.7	~ 63.54	~ 45	~ 63.9	~ 87	~ 51.6	~ 100	~ 64	~ 99.9	-
Q-Value(MeV/ c^2)	154.16	-	262.68	-	87.55	37.84	127.55	111.53	76.96	70.92	70.66	-

Table 5: Difference of mass (ΔM), baryon number (ΔB), strangeness (ΔS) and charge (ΔQ) of the ratios.

Particle	Δ^{++}/p	K^*/K^+	Λ^*/Λ	Σ^{*+}/Λ	Σ^0/Λ	Σ^{*+}/Σ^+	Ξ^{*0}/Ξ^-
ΔM (MeV/ c^2)	293.8	402.25	403.82	267.12	76.96	193.43	210.49
ΔB	0	0	0	0	0	0	0
ΔS	0	0	0	0	0	0	0
ΔQ	+1	-1	0	+1	0	0	-1
Slope (%) per MeV	0.19	0.76	0.98	0.25	-0.08	0.37	0.42

425 **2.1.2 Results and comparison with data**

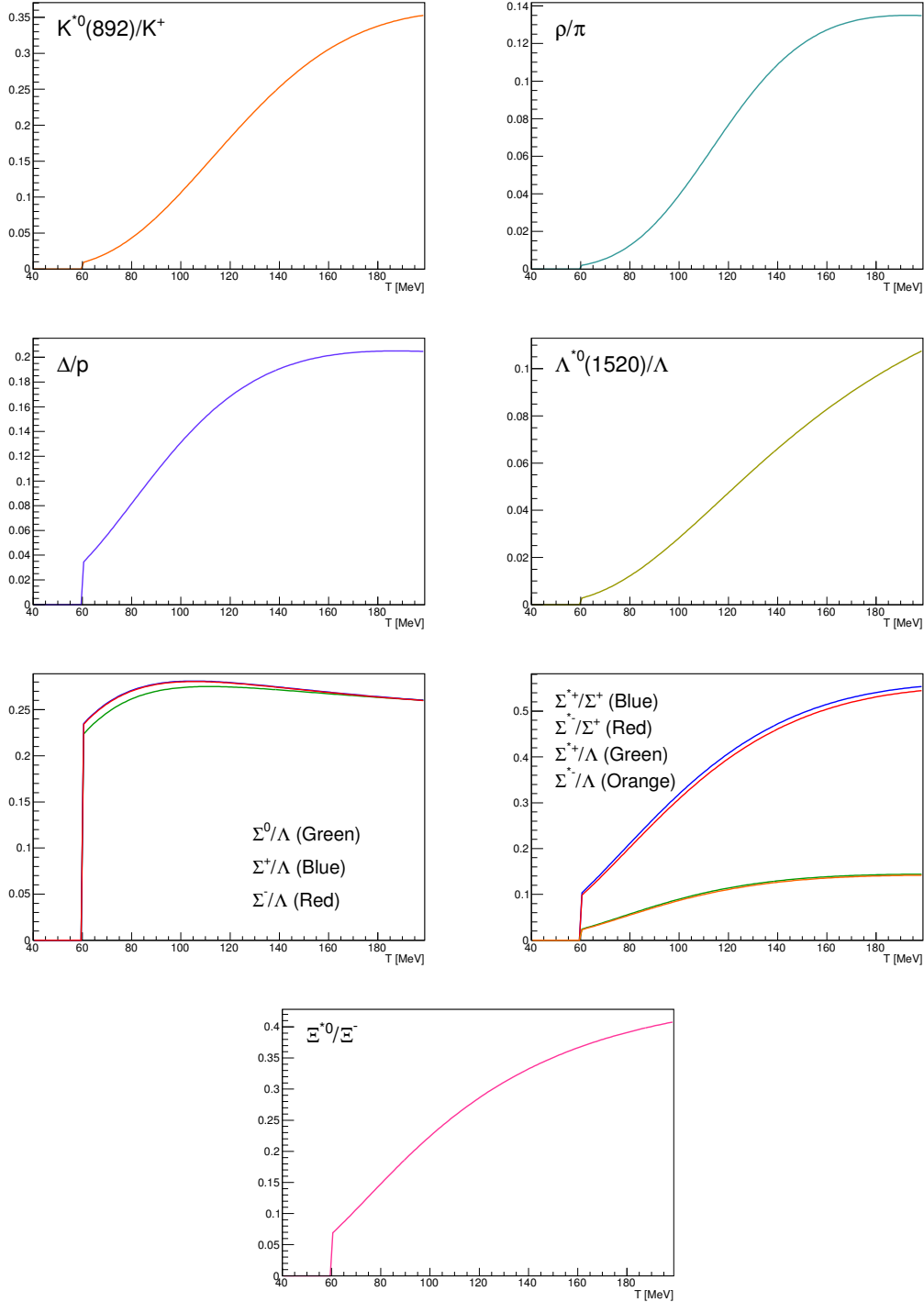


Figure 4: Ratio of baryonic and mesonic resonances over their stable partner as a function of temperature.

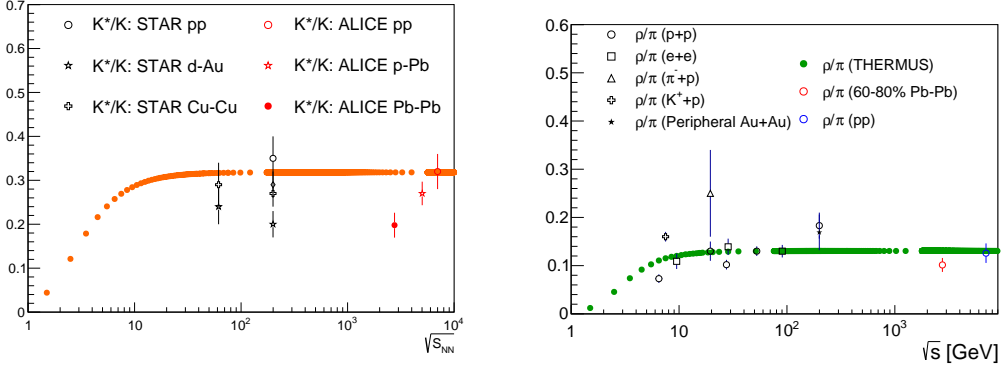


Figure 5: Ratio of resonances over their stable partner as a function of $\sqrt{(s)}$.

426 2.2 EPOS, UrQMD

427 The EPOS3 model [15, 16, 17] describes the full evolution of a heavy-ion collision. The
 428 initial stage is treated via a multiple-scattering approach based on Pomerons and strings.
 429 The reaction volume is divided into a core and a corona part [18]. The core is taken as
 430 the initial condition for the QGP evolution, for which one employ viscous hydrodynamics.
 431 The corona part is simply composed of hadrons from string decays. After hadronisation of
 432 the fluid (core part), these hadrons and as well the corona hadrons are fed into UrQMD
 433 [19, 20], which describes hadronic interactions in a microscopic approach. The chemical
 434 and kinetic freeze-outs occur within this phase. The chemical freeze-out is expected to
 435 occur shortly after the phase transition from partonic to hadronic matter and is followed
 436 by the kinetic freeze-out.

437 As explained in [15, 16, 17, 18], EPOS3 is an event generator based on 3+1D viscous
 438 hydrodynamical evolution starting from flux tube initial conditions, which are generated
 439 in the Gribov-Regge multiple scattering framework. An individual scattering is referred
 440 to as a Pomeron, identified with a parton ladder, eventually showing up as flux tubes (or
 441 strings). Each parton ladder is composed of a pQCD hard process, plus initial and final
 442 state linear parton emission. Nonlinear effects are considered by using saturation scales
 443 Q_s , depending on the energy and the number of participants connected to the Pomeron in
 444 question.

445 The final state partonic system (corresponding to a Pomeron) amounts to (usually two)
 446 color flux tubes, being mainly longitudinal, with transversely moving pieces carrying the
 447 p_T of the partons from hard scatterings. One has two flux tubes based on the cylindrical
 448 topology of the Pomerons. Each quark- antiquark pair in the parton ladder will cut a string
 449 into two; in this sense one may have more than two flux tubes. In any case, these flux

tubes eventually constitute both bulk matter, also referred to as ?core? (which thermalizes, flows, and finally hadronizes) and jets (also referred to as ?corona?), according to some criteria based on the energy of the string segments and the local string density. For the core, we use a 3+1D viscous hydrodynamic approach, employing a realistic equation of state, compatible with lQCD results. We employ for all calculations in this paper a value of $\eta/s = 0.08$. Whenever a hadronisation temperature of T_H is reached, we apply the usual Cooper-Frye freeze-out procedure, to convert the fluid into particles. We use $T_H = 166\text{MeV}$. From this point on, we apply the hadronic cascade UrQMD [19, 20], about which more details are given later. All hadrons participate in the cascade, including those from the core (after freeze- out) and the corona. The corona particles, from string decay, are only ?visible? after a certain formation time (some constant of order one fm/c), multiplied by the corresponding gamma factor), so very high p_T particles have a good chance to escape.

The UrQMD model is a non-equilibrium transport approach. The interactions of hadrons in the current version include binary elastic and $2 \rightarrow n$ inelastic scatterings, resonance creations and decays, string excitations, particle + antiparticle annihilations as well as strangeness exchange reactions. The cross sections and branching ratios for the corresponding interactions are taken from experimental measurements (where available), detailed balance relations and the additive quark model. The model describes the full phase-space evolution of all hadrons, including resonances, in a heavy- ion collision based on their hadronic interactions and their decay products. Due to the short lifetime of resonances, their decay products may interact in the hadronic phase. This is not the case for weak decays, where the system has already decoupled at the time of the decay. As discussed previously, the experimental reconstruction of resonances will be influenced by the final state interactions of the decay products. Resonance signals have been previously studied using the UrQMD model.

475 3 Production of resonance with strangeness

476 The Quark Model, proposed independently by Murray Gell-Mann and Yuval Ne?eman in
 477 1964 [21], enables the classification of hadrons in terms of their constituent quarks. In
 478 this model, the lighter mesons and baryons are representations of an $SU_f(3)$ group, whose
 479 fundamental representation is the three dimensional vector (u, d, s). These are the three
 480 lighter quarks whose characteristics are reported in Table reftable:quark.

Light flavor	d	u	s
Baryon number (B)	+1/3	+1/3	+1/3
Electric charge (Q)	-1/3	+2/3	-1/3
Isospin (I)	-1/2	+1/2	0
Strangeness (S)	0	0	-1
mass (MeV/c^2)	$2.3^{+0.7}_{-0.5}$	$4.8^{+0.5}_{-0.3}$	95 ± 5

Table 6: Quantum numbers and masses associated to the three lighter quarks: u, d and s

481 The hadronic state are obtained from the decomposition of the following scalar prod-
 482 ucts of the fundamental representations of the group:

483

$$484 \text{ Meson } (q\bar{q}) \ 3 \otimes \bar{3} = 1 \oplus 8$$

485

$$486 \text{ Baryon } (qqq) \ 3 \otimes 3 \otimes 3 = 10_S \oplus 8_M \oplus 8_M \oplus 1_A$$

487

488 For the baryons without c or b quark, flavor and spin may be combined in an approxi-
 489 mate flavor-spin $SU(6)$, in which the six basic states are $d \uparrow, d \downarrow, \dots, s \downarrow$ (\uparrow, \downarrow = spin up,
 490 down). Then the baryons belong to the multiplets on the right side of

491

$$492 \ 6 \otimes 6 \otimes 6 = 56_S \oplus 70_M \oplus 70_M \oplus 20_A$$

493

494 Here, the 56 representation can be decompose in an octet ($J^P = 1/2^+$) and a decuplet
 495 ($J^P = 3/2^+$), as can be seen in Figure 6 and Figure 7.

496 Among the hadrons, the special family of particles that contain at least one strange
 497 quark but not heavier quarks (like charm or bottom), are called hyperons. These are:
 498 the Λ (uds), the triplet $\Sigma^+(uus)$, $\Sigma^0(uds)$, $\Sigma^-(dds)$, the doublet $\Xi^-(dss)$, $\Xi^0(uss)$ and the
 499 $\Omega(sss)$ and the corresponding antiparticles. Ξ and Ω are the only hyperons containing more
 500 than one strange quark, hence they are called multi-strange baryons. Resonances shown in
 501 Figure reffig:decuplet having * with its name (e.g. $X^{*\pm}$) are particles with higher mass than
 502 the corresponding ground state particle with the same quark content. Different resonances
 503 with different lifetimes can probe different stages of the fireball expansion. The lifetime
 504 of some short-lived resonances is reported in Table 7. The ratios between resonances and

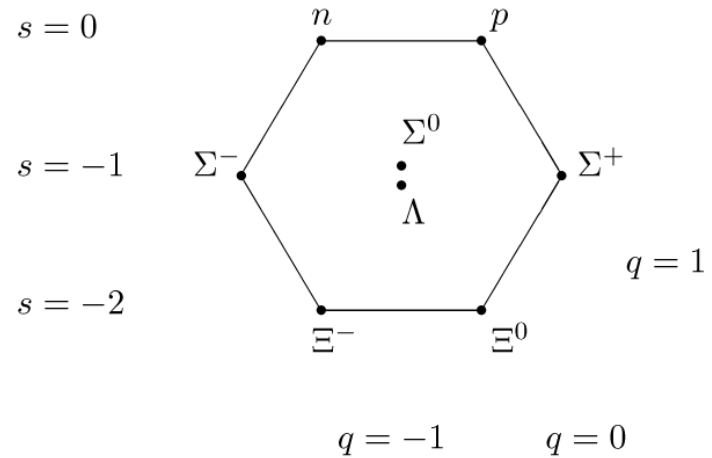


Figure 6: The $J^P = 1/2^+$ ground state baryon octet

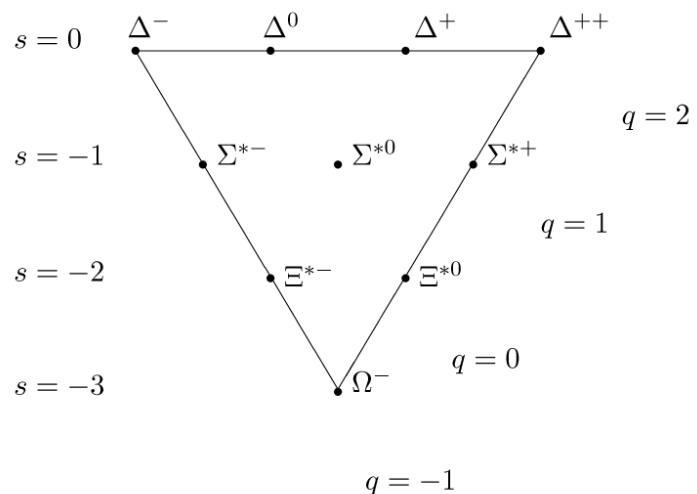


Figure 7: The $J^P = 3/2^+$ baryon decuplet

505 stable hadrons can be compared for resonances with different lifetimes and provide insights
 506 on the role of the re-scattering effect between the two freeze-out phases.

Particle	$\rho(770)$	$\Delta(1232)$	$K^*(892)$	$\Sigma(1385)$	$\Lambda(1520)$	$\Xi(1530)$	$\Phi(1020)$
Lifetime[c τ]	1.3 fm	1.7 fm	4.0 fm	5.5 fm	10.3 fm	22 fm	46 fm

Table 7: Lifetime of hadronic resonances

507 In the following, a general overview of the role of the strange quark within the QGP
 508 studies with heavy-ion collisions is given. And importance of the measurement of resonance
 509 is explained as probe of properties in hadronic phase between the chemical(T_{ch}) and the
 510 kinetic freeze-out(T_{kin}).

511 3.1 Strange quark and hyperons

512 The original interest in the strangeness in the context of the QGP comes from an idea by
 513 Johann Rafelski and Berndt Müller. In 1982, they suggested a possible signature for the
 514 formation of a QGP in a heavy-ion collision [22]. The key argument, at a fixed collision
 515 energy, rests on the different production mechanism of the s quark within two different
 516 systems:

- 517 **1. Hadron Gas (HG)** , where the degrees of freedom are the hadronic ones, as quark
 518 and gluons are confined
- 519 **2. QGP** , where the degrees of freedom are partonic ones, with quarks and gluons free
 520 with respect to each other

521 The mass of the hadrons is only partly due to the mass of the constituent valence
 522 quarks.

523 Naively speaking, the quarks ?dress up? due to the strong interaction that keeps them
 524 confined. Once they are free, as in a QGP, the quarks recover their bare masses. It was
 525 predicted that, if the QGP is formed, an enhancement of the strange quarks should occur,
 526 because the production of $s\bar{s}$ pairs becomes easier due to the lower energy needed. When
 527 the QGP cools down, these strange quarks eventually recombine into hadrons favoring also
 528 an enhancement of the number of strange hadrons. This effect is larger for hadrons with
 529 higher strangeness, with the following scaling for the number type:

530 $N_\Omega > N_\Xi > N_\Lambda$
 531 where N_Ω , N_Ξ , N_Λ are the number of produced Ω , Ξ and Λ . A certain enhancement of
 532 strange hadrons can occur also in a hadron gas system, but the processes of hadronisation
 533 in this case are relatively easy for K and Λ . and progressively harder for hadrons with
 534 higher strangeness, hence the relation would be:
 535

537 $N_\Omega < N_\Xi < N_\Lambda$.

538 The production of multi-strange hadrons with respect to pp - like collisions is considered
 539 to be a signature of the formation of the QGP and it was observed at SPS, RHIC and LHC.
 540 [23]

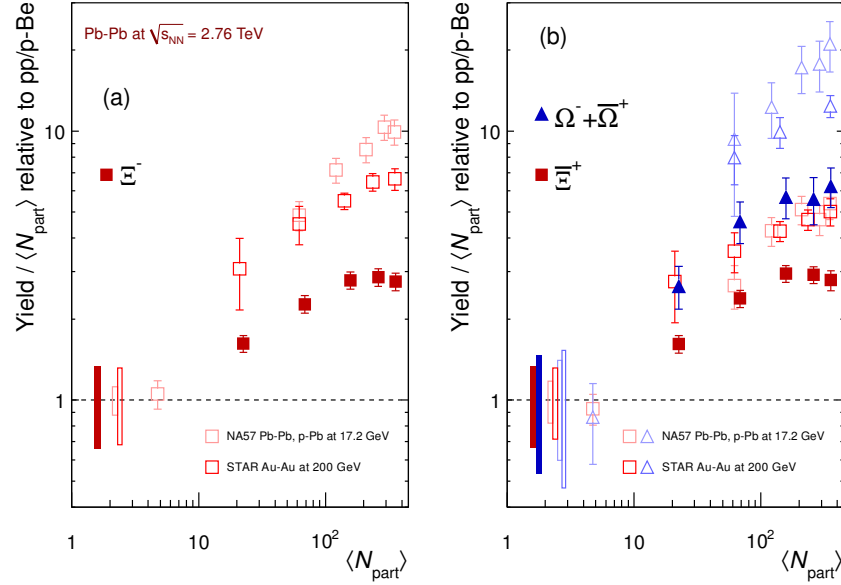


Figure 8: Enhancements in the rapidity range $|y| < 0.5$ as a function of the mean number of participants $\langle N_{part} \rangle$, showing LHC (ALICE, full symbols), RHIC and SPS (open symbols) data. Boxes on the dashed line at unity indicate statistical and systematic uncertainties on the pp or p-Be reference. Error bars on the data points represent the corresponding uncertainties for all the heavy-ion measurements and those for p-Pb at the SPS.

541 The measured enhancement factors of baryons with increasing strangeness content are
 542 reported in Figure 8 as a function of the number of participant nucleons, $\langle N_{part} \rangle$, in com-
 543 parison with similar measurements at SPS and RHIC. For p-Pb collisions there is no
 544 evidence of enhancement. For Pb-Pb collisions the enhancement increases with centrality
 545 and the effect is larger for particles with higher strangeness content, up to a factor ?20 for
 546 ?s. No hadronic model has reproduced these observations and they can be interpreted as
 547 clear signal of QGP state formation. The comparison with results from the previous ex-
 548 periments shows that the relative enhancements decrease with increasing collision energy.
 549 An explanation of this behavior is given in terms of a statistical model, with canonical
 550 strangeness conservation. In a small system, with small particles multiplicities, quantum
 551 numbers conservation laws (such as strangeness) must be applied locally, event-by-event,

552 whereas in a large system, with many degrees of freedom, they can be applied in average,
 553 by means of the corresponding chemical potential. The conservation of quantum numbers
 554 is known to reduce the phase space available for particle production. This canonical sup-
 555 pression factor decreases with lower energy in the centre of mass of the collisions and could
 556 explain the larger enhancement for lower energy systems.

557 **3.2 Resonance production**

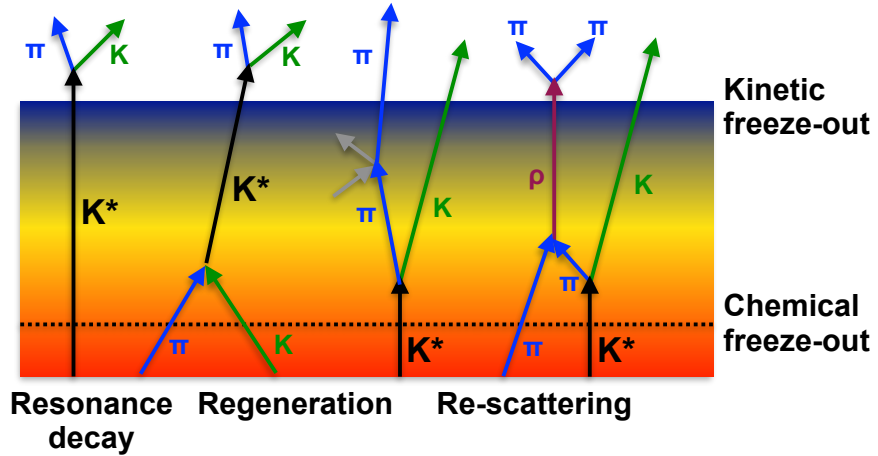


Figure 9: Hadronic phase

558 Resonances are particles with higher mass than the corresponding ground state particle
 559 with the same quark content. Hadronic resonances decay strongly, thus with a short
 560 lifetime, $\tau \sim$ few tenths of fm/c. The resonance natural width is given by $\Gamma = \bar{h}/\tau$, that
 561 is inversely proportional to the lifetime. Broad states with finite Γ decay very shortly
 562 after being produced and can be measured only by reconstruction of their decay products
 563 (or "daughters") in a detector. In heavy-ion collisions, hadronic resonances are produced
 564 within the bulk of the expanding medium, where they can decay while still traversing its
 565 volume. Decay products may interact with the other particles of the medium (mostly pions
 566 at the LHC), resulting in the impossibility of reconstructing the resonance, because the
 567 invariant mass of the daughters does not match that of the parent particle. Conversely,
 568 resonances may be regenerated as a consequence of pseudo-elastic collisions in the time
 569 lapse between the chemical (T_{ch}) and the kinetic freeze-out (T_{kin}). Re-scattering and
 570 regeneration depend on the individual cross section, hence lifetime, of the resonances and
 571 affect the measurement of their yield and momentum spectrum. The yield is decreased if the
 572 re-scattering dominates, vice versa the regeneration feeds the system with more particles.

⁵⁷³ The two effects may even compensate. Different resonances with different lifetimes can
⁵⁷⁴ probe different stages of the fireball expansion. The ratios between resonances and stable
⁵⁷⁵ hadrons can be compared for resonances with different lifetimes and provide insights on
⁵⁷⁶ the role of the re-scattering effect between the two freeze-out phases.

577 **4 A Large Ion Collider Experiment at the LHC**

578 ALICE (A Large Ion Collider Experiment) has been collecting data during the whole first
579 phase of the Large Hadron Collider operations, from its startup on the 23 November 2009
580 to the beginning of the first long technical shutdown in February 2013. During the first
581 three years of operations LHC provided pp collisions at 0.9, 2.76, 7 and 8 TeV, Pb–Pb colli-
582 sions at 2.76A TeV and finally p–Pb collisions at 5.02 TeV. The first section of this chapter
583 focuses on the LHC performance during this phase and includes details on the accelerator
584 parameters that allow the LHC to perform as a lead ion collider. A detailed description
585 of the ALICE detector follows in the section 4.2.1. ALICE has been designed and op-
586 timized to study the high particle-multiplicity environment of ultra-relativistic heavy-ion
587 collisions and its tracking and particle identification performance in Pb–Pb collisions are
588 discussed. The attention is drawn in particular on the central barrel detectors. Section
589 4.2.2 describes the ALICE Data Acquisition (DAQ) system, that also embeds tools for the
590 online Data Quality Monitoring (DQM). The final part of the chapter is dedicated to the
591 offline computing and reconstruction system based on the GRID framework.

592 **4.1 The Large Hadron Collider**

593 The Large Hadron Collider (LHC) [24] at CERN is the biggest particle accelerator world-
594 wide. The LHC project was approved in 1994 and construction works in the existing
595 underground tunnel started in 2001 after the dismantling of the LEP collider, which had
596 previously been built in the tunnel which is located under the Swiss-French border area
597 close to Geneva at a depth of 50 to 175 m. The LHC has a circumference of 26.7 km. By
598 design, its maximum achievable energies are 7 TeV for beam of protons and 2.76 TeV per
599 nucleon for beam of lead ions, thus providing collisions at $\sqrt{s} = 14$ TeV and $\sqrt{s_{NN}} = 5.5$
600 TeV, respectively. These would be the largest energies ever achieved in particle collision
601 experiments. The LHC is a synchrotron that accelerates two counter-rotating beams in
602 separate parallel beam pipes. In each of them bunches of particles travel many times
603 around the accelerator ring before the collision energy is reached. The accelerator has to
604 bend the beams around the ring, keep the bunches focused and accelerate them to their
605 collision energy. Finally, the spatial dimension of the bunches has to be minimized in order
606 to attain high luminosity, which ensure a high number of collisions per time interval at
607 the collision points, i.e. a high luminosity. A combination of magnetic and electric field
608 components performs the mentioned tasks. Despite the high luminosity reached, only a
609 very small fraction of the particles of two bunches collides in a single bunch crossing. The
610 others leave the interaction region essentially uninfluenced, are defocused, and continue to
611 circulate in the accelerator.

612 Injection of bunches into the LHC (Figure 10) is preceded by acceleration in the
613 LINAC2, PS booster, PS, and SPS accelerators. The acceleration sequence is slightly
614 different for heavy-ions, in which case bunches pass the LINAC3, LEIR, PS, and SPS

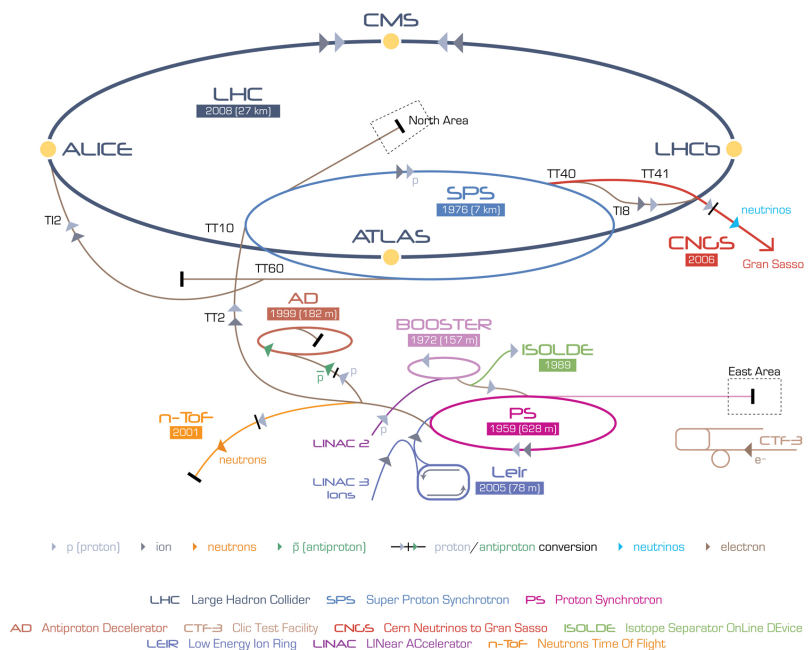


Figure 10: The CERN accelerator complex [2]

accelerators (more information can be found in [90]). Several injections to the LHC are needed until all bunches of both beams are filled. The first pp collisions at 900 GeV centre-of-mass energy were delivered by the LHC on September 10th 2008. Nine days later, the operations were interrupted due to a failure in an electrical connection between two magnets. The machine operators spent over a year repairing and consolidating the accelerator. On November 20th 2009 low energy proton beams circulated again, and a few days later, by achieving the energy of 1.18 TeV per proton beam, LHC became the most powerful accelerator in the world. The first pp collisions at centre-of-mass energy of 7 TeV were delivered in March 2010, and the first Pb?Pb collisions at centre-of-mass energy of 2.76 TeV per nucleon pair in November 2010. In 2010 the integrated luminosity delivered by the LHC was $\sim 48 \text{ pb}^{-1}$ for pp collisions at $\sqrt{s}= 7 \text{ TeV}$ ($\sim 0.5 \text{ pb}^{-1}$ in ALICE) and $\sim 10 \mu\text{b}^{-1}$ for Pb?Pb at $\sqrt{s_{\text{NN}}}= 2.76 \text{ TeV}$ ($\sim 10 \mu\text{b}^{-1}$ in ALICE). In 2011 the beam energy was the same as in 2010 both for pp and Pb-Pb. The performance of the LHC improved in terms of luminosity with $\sim 5.61 \text{ fb}^{-1}$ for pp ($\sim 2 \text{ pb}^{-1}$ in ALICE) and $\sim 166 \mu\text{b}^{-1}$ for Pb-Pb collisions ($\sim 143.62 \mu\text{b}^{-1}$ in ALICE). In 2012, the centre-of-mass energy for pp collisions was brought to 8 TeV and the integrated luminosity (up to December 2012, end of the pp program) was $\sim 23.3 \text{ fb}^{-1}$ ($\sim 10 \text{ pb}^{-1}$ in ALICE). A pilot p-Pb run operated at $\sqrt{s_{\text{NN}}}= 5.02 \text{ TeV}$ on September 2012, followed by a long p-Pb run on February 2013 with a delivered luminosity of 31.2 nb^{-1} . A very short pp run at $\sqrt{s}= 2.76 \text{ TeV}$ ended the Run1 of the LHC program, marking the start of the first long shutdown (LS1) until the end of 2014. Despite its excellent performance, the LHC has not yet achieved the nominal parameters (\sqrt{s}, L), that is the main goal for the next ignition of the machine in 2015. The LHC produces collisions in four so called Interaction Points (IPs) in correspondence of which are located six detectors of different dimensions and with different goals, all able to study the products of the interactions. These are:

ALICE (A Large Ion Collider Experiment-IP₂) [25] is a dedicated heavy-ion experiment designed to study strongly-interacting matter at very high energy density. It explores the phase transition to the QGP, its phase diagram, and its properties. Furthermore, ALICE will also study collisions of protons, on one hand as a baseline for heavy-ion measurements and on the other hand it contributes to measurements of identified particles by making use of its excellent particle identification capability and its acceptance at very low transverse momenta.

ATLAS (A Toroidal LHC ApparatuS-IP₁) and CMS (Compact Muon Solenoid - IP₅) [26][27] are general-purpose detectors for pp collisions that are built to cover the widest possible range of physics at the LHC. Specific topics are the search for the Higgs boson and physics beyond the Standard Model, e.g. new heavy particles postulated by supersymmetric extensions (SUSY) of the Standard Model and evidence of extra dimensions.

LHCb (The Large Hadron Collider beauty experiment-IP₈) [28] is a dedicated

656 experiment for the study of heavy flavor physics at the LHC. In particular, the experiment
657 focuses on the study of CP violation and rare decays of beauty and charm particles, to
658 test the Standard Model and to search for evidence of New Physics. The LHCb physics
659 program is complementary to the flavor physics studies conducted at the B-factories and
660 to the direct searches for new particles performed at ATLAS and CMS.

661

662 **LHCf (Large Hadron Collider forward experiment-IP₁)** [29] measures forward
663 particles created during LHC collisions to provide further understanding of high energy
664 cosmic rays. The detector is placed close to the ATLAS experiment.

665

666 **TOTEM (TOTal Elastic and diffractive cross-section Measurement-IP₅)** [30]
667 measures the total cross-section, elastic scattering, and diffractive processes. The detector
668 is located close to the CMS experiment.

669

670 4.2 The ALICE project

671 The ALICE experiment at the LHC [31] has as main goal the study of nuclear matter
672 under extreme conditions of temperature and energy density such as those reached in ultra-
673 relativistic heavy-ion collisions. The aim is to verify the QCD prediction of the existence of
674 a phase transition from the common hadronic matter to the Quark-Gluon Plasma. Since
675 ALICE is the only LHC experiment specifically designed for Pb–Pb collisions, it has to
676 be able to cope with the large multiplicities associated with these collision systems and at
677 the same time has to cover as many QGP-related observables as possible. ALICE is also
678 interested in the study of pp interactions, as these are crucial for a comparison with Pb–Pb
679 collisions, to tune Monte Carlo models and per se, like the other LHC experiments. With
680 respect to these experiments, ALICE is endowed with an excellent Particle IDentification
681 (PID) performance, obtained combining different PID techniques from different detectors
682 that are optimized in different momentum (p) regions.

683 4.2.1 ALICE detector

684 ALICE is a complex of 14 detector subsystems (Figure 11) that can be classified in three
685 groups:

686

687 **Central detectors** are housed in a solenoid magnet which provides the experiment
688 with a 0.5 T magnetic field and covers the pseudo-rapidity interval $-0.9 < \eta < 0.9$ (corre-
689 sponding to a polar acceptance $\pi/4 < \theta < 3\pi/4$). The azimuthal acceptance is 2π . They
690 are mainly dedicated to vertex reconstruction, tracking, particle identification and momen-
691 tum measurement. Starting from the interaction region and going outward, we find the
692 following detectors:

- Inner Tracking System (ITS)
- Time Projection Chamber (TPC)
- Transition Radiation Detector (TRD)
- Time Of Flight (TOF)

697 In the mid-rapidity region there are also three detectors with limited azimuthal accep-
 698 tance:

- High Momentum Particle Identification Detector (HMPID)
- PHOton Spectrometer (POHS)
- ElectroMagnetic CALorimeter (EMCAL)

702 **Muon spectrometer** is placed in the forward pseudo-rapidity region ($-4.0 < \eta < -2.5$) and consists of a dipole magnet and tracking and trigger chambers. It is optimized to
 703 reconstruct heavy quark resonances (such as J/Ψ through their $\mu^+\mu^-$ decay channel) and
 704 single muons.

706 **Forward detectors** are placed in the high pseudo-rapidity region (small angles with
 707 respect to the beam pipe). They are small and specialized detector systems used for
 708 triggering or to measure global event characteristics. They are:

- Time Zero (T0) to measure the event time with precision of the order of tens of picoseconds, as needed by TOF
- VZERO (V0) to reject the beam-gas background and to trigger minimum bias events
- Forward Multiplicity Detector (FMD) to provide multiplicity information over a large fraction of the solid angle ($-3.4 < \eta < -1.7$ and $1.7 < \eta < 5$)
- Photon Multiplicity Detector (PMD) to measure the multiplicity and the spatial distribution of photons on an event-by-event basis in the $2.3 < \eta < 3.7$ region
- Zero Degree Calorimeter (ZDC) to measure and trigger on the impact parameter. The ZDC consists of two calorimeters, one for neutrons (ZDC:ZN) and one for protons (ZDC:ZP), and includes also an electromagnetic calorimeter (ZEM)

720 The ALICE global coordinate system [32] is a right-handed orthogonal Cartesian system
 721 with the origin X, Y, Z = 0 at the centre of the detector. The three Cartesian axes are
 722 defined as follows: the X axis pointing towards the centre of the LHC, the Y axis pointing
 723 upward and the Z axis parallel to the local mean beam line pointing in the direction opposite

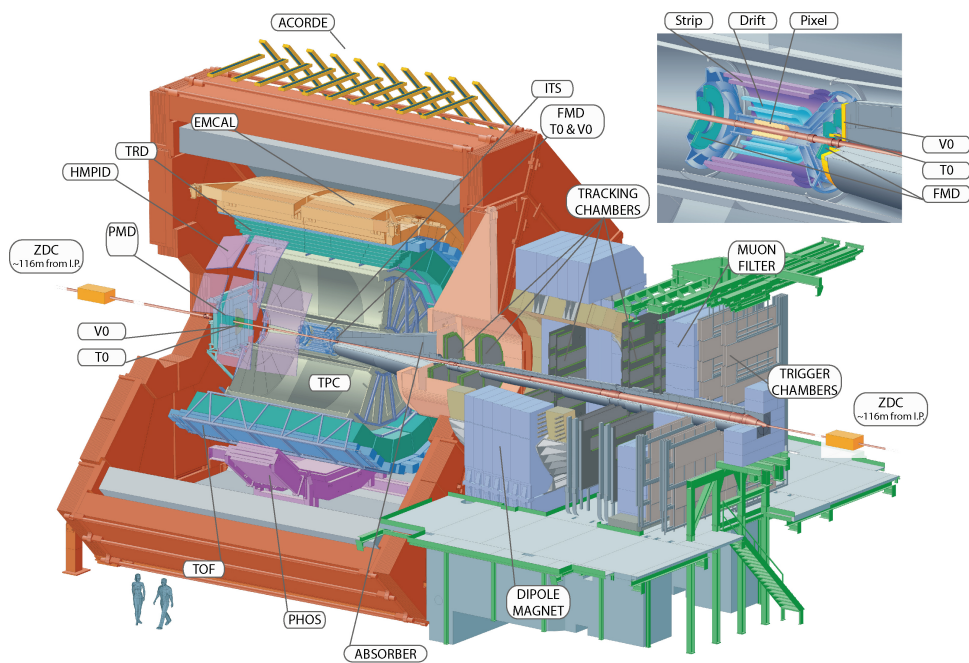


Figure 11: The ALICE detector

724 to the muon spectrometer. The azimuthal angle increases counter-clockwise from the
725 positive X axis ($\Phi = 0$) to the positive Y axis ($\Phi = \pi/2$) with the observer standing at
726 positive Z and looking at negative Z; the polar angle increases from the positive Z axis (θ
727 = 0) to the X-Y plane ($\theta = \pi/2$) and to the negative Z axis ($\theta = \pi$).

728 In the following Sections more specific descriptions of the detectors used in the identifi-
729 cation of the $\Xi(1530)^0$ baryons and in the determination of the characteristics of typical
730 collisions will be given.

731

ITS

732 The ITS [31] (Figure 12) is the barrel detector closest to the beam pipe. Its main goals
733 are:

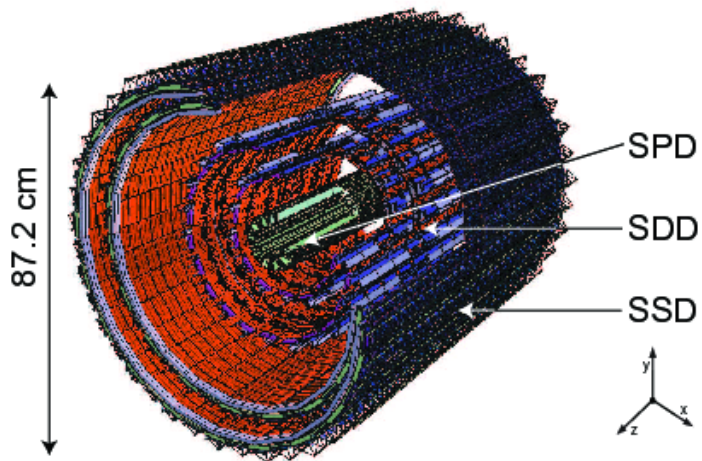


Figure 12: Schematic view of the ITS [3]

734

- 735 • to contribute with the TPC to the global tracking of ALICE by improving the angle
736 and momentum resolution
- 737 • to reconstruct the position of the primary interaction vertex
- 738 • to reconstruct secondary vertices from decays of heavy-flavor and strange particle
739 decays;
- 740 • to track and identify particles with momentum below $100 \text{ MeV}/c^2$
- 741 • to improve the momentum, impact parameter and angle resolution for the measure-
742 ment of high p_T particles performed with the TPC

- 743 • to reconstruct particles traversing dead regions of the TPC

744 The ITS surrounds the beam pipe (which is a 800 μm thick cylinder with an outer
 745 diameter of 2.9 cm) and consists of six cylindrical layers of silicon detectors located at radii
 746 between 4 cm and 43 cm. Due to the high track density, the two innermost layers are
 747 Silicon Pixel Detectors (SPD) which guarantee a high granularity. They are followed by
 748 two layers of Silicon Drift Detectors (SDD), while the two outmost layers are double-sided
 749 Silicon micro-Strip Detectors (SSD).

750 Since the momentum and impact parameter resolutions for low momentum particles
 751 are dominated by multiple scattering effects, the amount of material in the active volume
 752 has been minimized as much as possible. The granularity of the detector was optimized to
 753 keep the occupancy low in all the layers. With the technology chosen, the ITS detectors
 754 reach a spatial resolution of the order of a few tens of m resulting in a resolution on the
 755 impact-parameter⁵ better than 70 m in the r plane for $p_T > 1 \text{ GeV}/c$ and thus well suited
 756 for the reconstruction of heavy-flavor decays (see Figure 13).

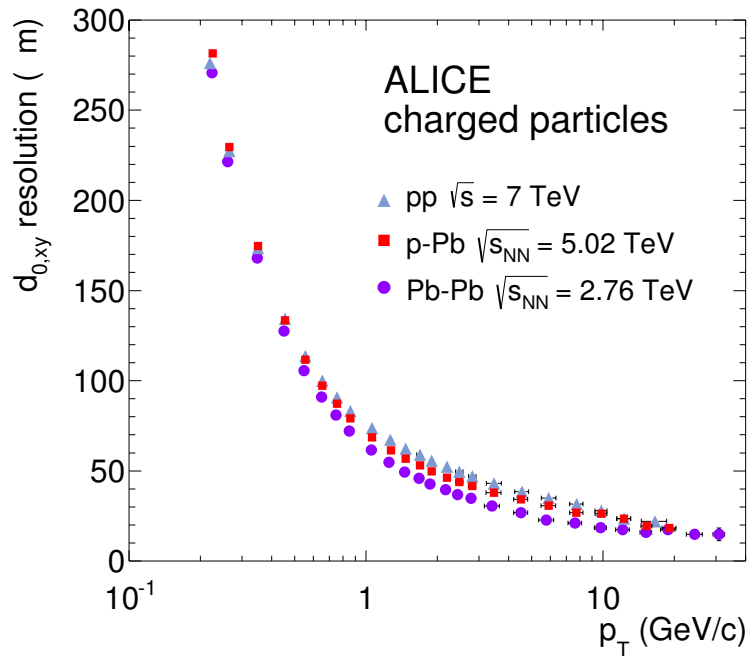


Figure 13: Track impact parameter resolution in the transverse plane ($r\phi$) vs p_T for charged particle

757 TPC

758 The TPC [33] (Figure 14) is the main tracking detector of the central barrel, optimized

759 to provide, together with the other central barrel detectors, charged-particle momentum
 760 measurements with good two-track separation, particle identification and vertex determina-
 761 tion. The TPC was designed for an excellent tracking performance in the high multiplicity
 762 environment of Pb–Pb collisions. For this reason, it was chosen to be a drift chamber,
 763 cylindrical in shape, 5 m long, with the inner radius ($r_{in} \sim 85$ cm) determined by the
 764 maximum acceptable track density, and the external one ($r_{ext} \sim 250$ cm) by the minimum
 765 track length for which dE/dx resolution is $< 10\%$. The TPC volume is filled with 90 m^3 of
 766 Ne/CO₂/N₂ (90/10/5). The readout planes are divided in 18 sectors in which multi-wire
 767 proportional chambers (with cathode pad readout) are housed. Because of its good dE/dx
 768 resolution, the TPC can identify particles with $p_T < 1\text{ GeV}/c$ on a track-by-track basis.

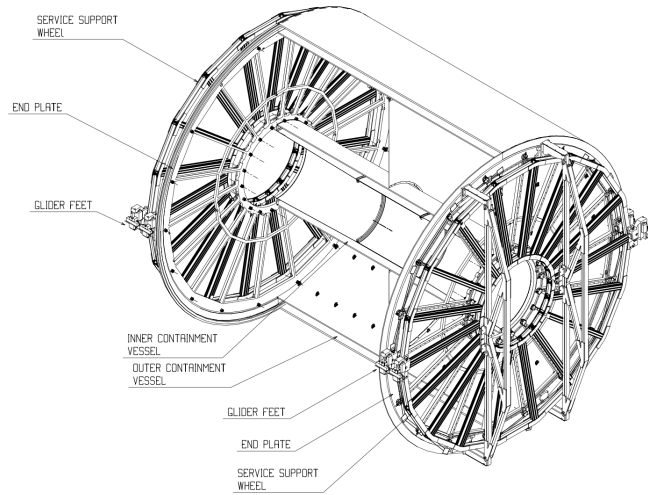


Figure 14: Schematic view of the TPC

769 Charged particles traveling through the TPC ionize the detector's gas; the measure-
 770 ment of this loss of energy is what we need to identify a particle. The physics observable
 771 in this case is the energy loss per unit length, within the matter crossed by the charged
 772 particle, which we call specific energy loss, also denoted by dE/dx . This is described by
 773 the Bethe–Bloch equation, 5, that highlights the key of the identification technique: this
 774 observable depends only on the charge and on velocity (β) of the particle, which, in turn,
 775 depends only on the momentum and the mass of the ionizing particle. Since momentum is
 776 already known due to track curvature and charge is unitary for most measured tracks, mea-
 777 suring the dE/dx allows us to indirectly determine mass and thus determine the particle
 778 species. The Bethe-Bloch equation gives the mean specific energy loss:

$$-\langle \frac{dE}{dx} \rangle = k_1 \cdot z^2 \frac{Z}{A} \cdot \frac{1}{\beta^2} \left[\frac{1}{2} \ln(k_2 \cdot m_e c^2 \cdot \beta^2 \gamma^2) - \beta^2 + k_3 \right] \quad (5)$$

779 where $\beta\gamma = p/Mc$ and: Z: atomic number of the ionized gas (in this case Ne/CO₂/N₂)
 780 A: mass number of the ionized gas (g/mol)
 781 m_e: electron mass
 782 z: electric charge of the ionizing particle in unit of electron charge e
 783 M: ionizing particle mass
 784 p: ionizing particle momentum
 785 β: ionizing particle velocity normalized to the light velocity c
 786 γ = 1/√(1 - β²), Lorentz factor
 787 k₁, k₂, k₃: constants depending on the ionized medium

788
 789 For a given ionizing particle mass hypothesis, a given momentum and a given length
 790 of the trajectory in the ionizing medium, the total charge deposited along the trajectory
 791 is subject to statistical fluctuations. This random variable follows a Landau distribution,
 792 that give us the opportunity to measure the mean value hdE/dx . The long tail of the
 793 Landau distribution is usually truncated at 50%-70% of the collected signal.

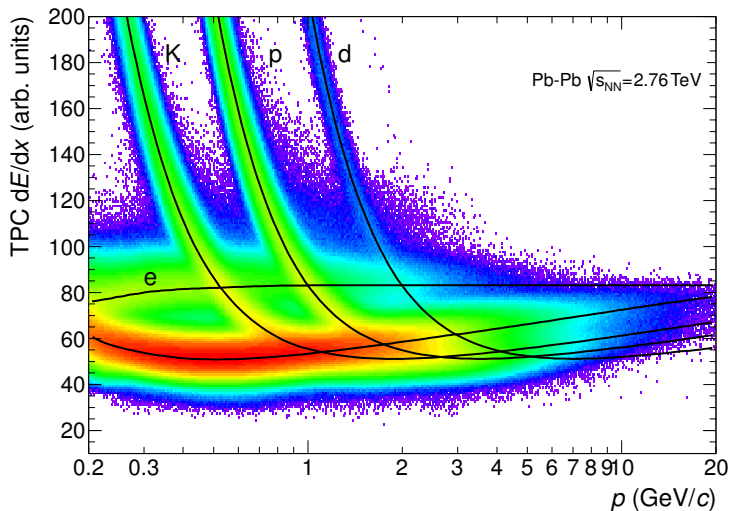


Figure 15: Specific energy loss (dE/dx) in the TPC vs. particle momentum in Pb–Pb collisions at $\sqrt{s_{NN}} = 2.76$ TeV. The lines show the parametrisations of the expected mean energy loss.

794 The specific energy loss in the TPC as a function of momentum is shown in Figure
 795 15. The different bands characteristic for e[±], π[±], K[±], p[±] are clearly visible. These
 796 are the evidence of the statistical distribution of the measured energy loss around the
 797 expected mean value. The expected value correspond to the prediction by a Bethe–Bloch
 798 experimental parametrization (superimposed as black lines in the Figure). For a track

799 within the TPC the relevant quantity to be considered for PID is the difference between
 800 the measured specific energy loss and the corresponding predicted value, by the Bethe-
 801 Bloch parametrization for a given measured momentum. If normalized to the resolution
 802 of the dE/dx measurement in the TPC, this difference could be expressed in number of
 803 σ (see Equation 6). In this way it is possible to estimate more quantitatively the goodness
 804 of a mass hypothesis. This also gives us the possibility to choose the strictness we want to
 805 adopt in the identification of a particle (n_σ , $n = 2, 3, 4$):

$$n_\sigma = \frac{(dE/dx)_{measured} - (dE/dx)_{Bethe-Bloch}}{\sigma_{TPC}} \quad (6)$$

V0

806 The VZERO detector [34] consists of two segmented arrays of plastic scintillator counters,
 807 called VZERO-A and VZERO-C, placed around the beam-pipe on either side of the IP:
 808 one at $Z = 340$ cm, covering the pseudo-rapidity range [2.8; 5.1], and the other at $Z = -90$
 809 cm (in front of the absorber), covering the pseudo-rapidity range [-3.7; -1.7]. They consist
 810 of 32 counters distributed in four rings, each divided in eight 45 sectors. Each counter
 811 is made of scintillator material embedded with WaveLength Shifting fibers. Clear fibers
 812 collect and transport the signal to photomultipliers 3 - 5 m far from the detector, inside
 813 the L3 magnet. The counters have a time resolution better than 1 ns. Their response is
 814 recorded in a time window of 25 ns around the nominal beam crossing time. The VZERO
 815 has an important role in rejecting background from beam-gas collisions (see, Figure 16)
 816 exploiting the relative time-of-flight measurement between the two arrays: when the beam-
 817 gas collision takes place outside the region between the two arrays, particles arrive 6 ns
 818 before or after the time of a beam-beam collision.

819 The VZERO is a trigger detector that will provide a minimum-bias trigger for all
 820 colliding systems to the central barrel detectors and three centrality triggers in p-Pb and
 821 Pb-Pb collisions (multiplicity, central and semi-central).

822 The first parameter to be determined in A-A(p-A) collisions is the centrality(multipliciy).
 823 This is defined according to the value of the impact parameter, b , and provides a geomet-
 824 rical scale of the overlapping region between the colliding nuclei: a collision will be defined
 825 from central to peripheral, as the impact parameter increases. The centrality of a collision
 826 is not directly available and must be deduced from a combination of experimentally mea-
 827 sured quantities and Monte Carlo simulations. There are a number of observables that can
 828 be measured and used as centrality estimators. The charged-particle multiplicity N_{ch} and
 829 the transverse energy E_T measured around mid-rapidity are measurable quantities related
 830 to the energy deposited in the interaction region (these are therefore related to N_{part}).
 831 These variables increase significantly increasing the centrality of the collisions. Another
 832 measurable quantity to estimate the centrality is the zero-degree energy EZDC, namely
 833 the energy carried by spectator nucleons $N_{spec} = 2A - N_{part} = E_{ZDC}/E_A$, where E_A is
 834 the beam energy per nucleon. Typically a measured distribution of one of the previous
 835 observables is mapped to the corresponding distribution obtained from phenomenological
 836

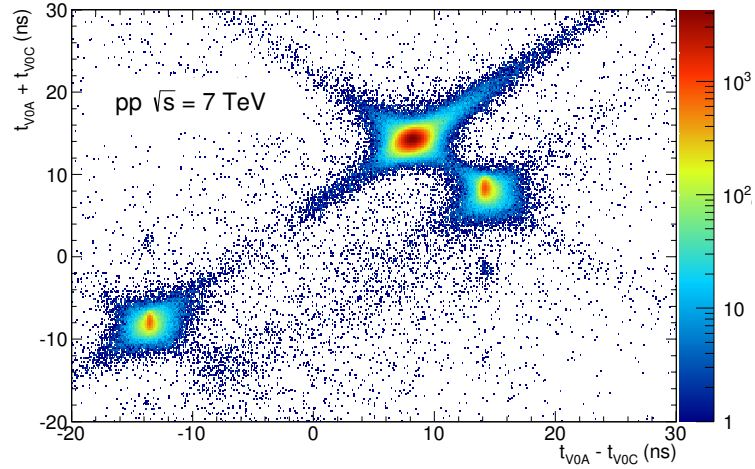


Figure 16: Correlation between the sum and difference of signal times in V0A and V0C. Three classes of events collisions at (8.3 ns, 14.3 ns), background from Beam 1 at (-14.3 ns, -8.3 ns), and background from Beam 2 at (14.3 ns, 8.3 ns) can be clearly distinguished.

837 Glauber calculations. The Glauber model [35, 36] uses a semi-classical approach: the A?A
 838 collision is assumed to be an incoherent superposition of N elementary nucleon- nucleon
 839 collisions. The main parameters of the model are the inelastic nucleon- nucleon collision
 840 cross-section σ_n and the nuclear density distribution $\rho(r)$. In practice, the simulated dis-
 841 tribution well reproduce the measured distribution or the latter is fitted with an analytical
 842 function. The experimental distribution can then be divided in classes with sharp cuts on
 843 the measured observable (E_{ZDC} , E_T or N_{ch}). These "centrality" classes will correspond to
 844 well defined percentage of the integral of the distribution. A given centrality class in the
 845 measured distribution, corresponds to the same class in the simulated distribution, where
 846 the main geometrical variables (N_{part} , N_{coll} and T_{AA}) can be determined. The number of
 847 classes that can be defined depends on the resolution achievable on the selection variable.
 848 In the analysis described in this thesis the centrality(multiplicity) estimation is based on
 849 the measurement of the multiplicities from the VZERO scintillators [37][38]. This is the
 850 method that achieve the best centrality resolution: it ranges from 0.5% in central to 2%
 851 in peripheral collisions. Other methods, as the ones based on the E_{ZDC} measurement or
 852 based on the estimate of the number of tracks in the SPD or TPC, are used to asses a
 853 systematic uncertainty on the centrality determination. The distribution of the VZERO
 854 amplitudes is shown in Figure 17 where the centrality(multiplicity) percentiles are also
 855 indicated.

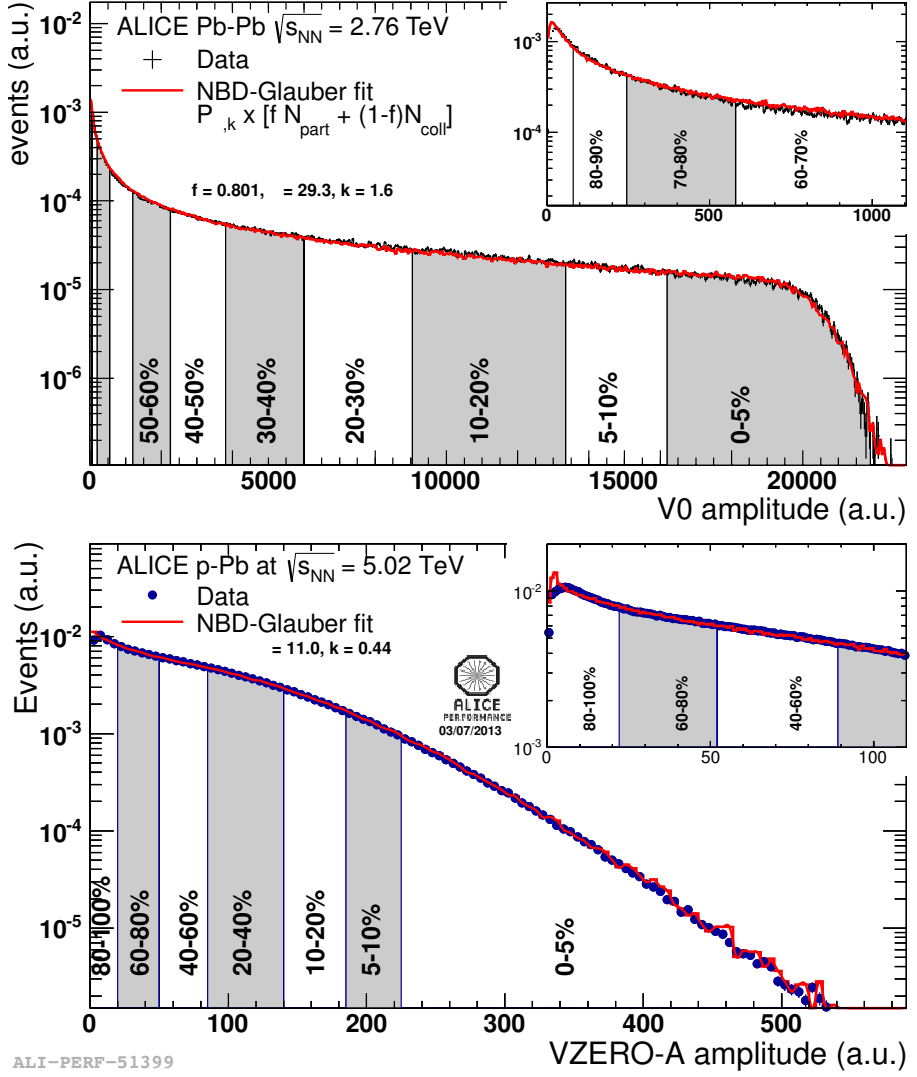


Figure 17: Distribution of the V0 amplitude (sum of V0A and V0C in top, V0A in bottom). The inset shows a magnified version of the most peripheral region.

856 **4.2.2 Data Acquisition (DAQ) and trigger system**

857 The architecture of data acquisition is shown in Figure 18. The tasks of the ALICE DAQ
 858 system are the assembly of event informations from individual detectors into complete
 859 events (event building) as well as buffering and export of assembled events to permanent
 860 storage. The DAQ is designed to process a data rate up to 1.25 GB/s in heavy-ion runs.
 861 Event building is done in two steps. Data from the detectors is received by Detector Data
 862 Links (DDLs) on Local Data Concentrators (LDCs). The LDCs assemble the data into
 863 sub-events that are then shipped to Global Data Collectors (GDCs). A GDC re- ceives all
 864 sub-events from a given event and assembles them into a complete event. These events are
 865 subsequently stored on a system called Transient Data Storage (TDS).

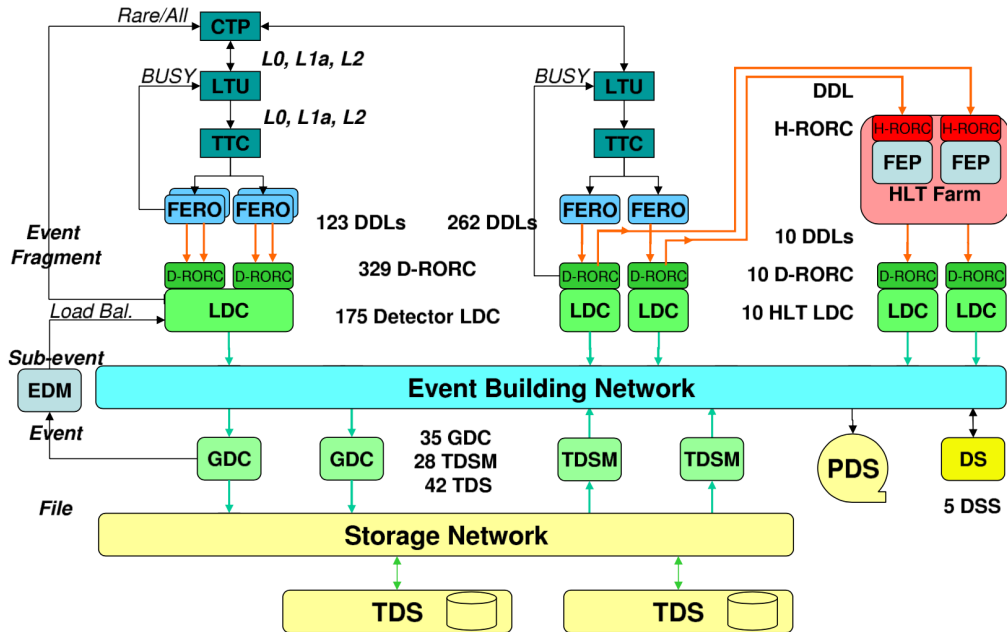


Figure 18: The overall architecture of the ALICE DAQ and the interface to the HLT system.

866 ALICE can simultaneously take data in several partitions, where a set of detec-
 867 tors can store their outputs. Since a partition is a group of commonly controlled detectors, a
 868 given detector can only be active in one partition at a time. The ac-
 869 tive detectors in a given partition may be assigned to data taking groups called clusters, for which triggers

can be defined. Therefore, upon a trigger only a sub-set of the whole partition may be read out. Furthermore, a triggering detector does not have to be necessarily part of the partition. ALICE has a two-layer trigger architecture [39]. The low-level trigger is a hardware trigger called Central Trigger Processor (CTP). The High-Level Trigger (HLT) is implemented as a pure software trigger. The CTP combines inputs from different trigger sources, namely the various detectors. These inputs are single signals, like a hit in the detector, or, can be the result of fast calculation performed directly in the detectors. The HLT allows the implementation of sophisticated logic for the triggering. In contrast to the CTP which governs the readout of the detectors, the HLT receives a copy of the data read out from the detectors and processes them. The hardware trigger combines the trigger signals of the various detectors to decide if an event is accepted, that means it is read out and written to disk. Several trigger levels reduce the event rate depending on the input signals. The first level, called L0, is delivered after 1.2 ?s, while the second, called L1, after 6.5 ?s. The final trigger, L2, is delivered after 100 ?s, upon completion of the drift time in the TPC. Only after an L2 trigger the event is finally stored. The rates of different trigger classes are very different. By definition minimum-bias triggers have the highest rate; other triggers that look for rare signals are characterized by much lower rates. In order to cope with different scenarios, downscaling factors can be applied to the trigger classes individually, i.e. only every nth event fulfilling the trigger condition is read out. The total recording rate is limited by the maximum bandwidth of data that can be recorded to disk and tape. The ALICE software trigger, called HLT, is a farm of multiprocessor computers. The aim is to have about 1000 PCs processing the data in parallel allowing an online analysis of the events. A trigger decision comes from the analysis of a more comprehensive set of information than what happens for the hardware trigger, giving the possibility to apply more sophisticated triggers. Examples include triggers on high energy jets or on muon pairs. Furthermore, the HLT can significantly reduce the event size by selecting regions of interest (partial readout of detectors) and by further compression of the data. The HLT receives a copy of the raw data and performs per detector reconstruction, partly aided by hardware coprocessors. Subsequently, the trigger decision is based on the global reconstructed event. In the same step a region of interest can be selected. In the last optional step, if the trigger decision is positive, the data are compressed. The trigger decision, partial readout information, compressed data, and the re-construction output is sent to LDCs and subsequently processed by the DAQ. In terms of the overall DAQ architecture, data sent by HLT is treated like stemming from a detector.

904 **4.2.3 ALICE offline software frame work**

905 The required computing resources for the reconstruction and analysis of the raw data as
906 well as the production of simulated events needed for the understanding of the data exceed
907 the computing power of single institutes and even centers like CERN. Therefore, institutes
908 that are part of the Collaboration also provide storage and computing resources. Distribu-
909 tion of the data for reconstruction and analysis cannot be performed manually and this
910 led to the need for an automated system. The concept of a decentralized computing model
911 called Grid [40] was identified as a solution.

912

913 *The AliEn Framework*

914 The Grid paradigm implies the unification of resources of distributed computing center,
915 in particular computing power and storage, to provide them to users all over the World.
916 It allows computing center to offer their resources to a wider community and the local re-
917 sources to be shared by an entire collaboration. Software that implements the Grid concept
918 is called Grid middleware. ALICE has developed a Grid middleware called AliEn [41] since
919 2001. An ALICE user employs AliEn to connect to the ALICE Grid which is composed
920 of a combination of general services that are provided by many Grid middleware solutions
921 and ALICE-specific services provided by AliEn. Parts of the ALICE Grid are: i) a global
922 file catalog that is a directory of files in storage elements distributed over the Globe, ii)
923 the automatic matching of jobs for execution to a suitable location in one of the connected
924 sites, iii) a shell-like user interface and iv) API9 services for the ROOT framework [42].

925

926 *AliRoot Framework*

927 AliRoot [31] is the offline framework for simulation, alignment, calibration, reconstruction,
928 visualization, quality assurance, and analysis of experimental and simulated data. It is
929 based on the ROOT framework. Most of the code is written in C++ with some parts in
930 Fortran that are wrapped inside C++ code. Re-usability and modularity are the basic
931 features of the AliRoot framework. Modularity allows parts of the code to be replaced,
932 with minimum or no impact on the rest (for example changing the event generator, the
933 transport Monte Carlo or the reconstruction algorithms). This is achieved implementing
934 abstract interfaces. In addition codes for each detector subsystem are independent modules
935 with their specific code for simulation and reconstruction and the code can be developed
936 concurrently with minimum interference. Re-usability is meant to maintain a maximum
937 amount of backward compatibility as the system evolves.

938 The central module of the AliRoot framework is STEER (Figure 19) which provides
939 several common functions such as: steering of program execution for simulation, reconstruc-
940 tion and analysis; general run management, creation and destruction of data structures,
941 initialization and termination of program phases; base classes for simulation, event genera-
942 tion, reconstruction, detectors elements. For event simulation the framework provides the
943 following functionality:

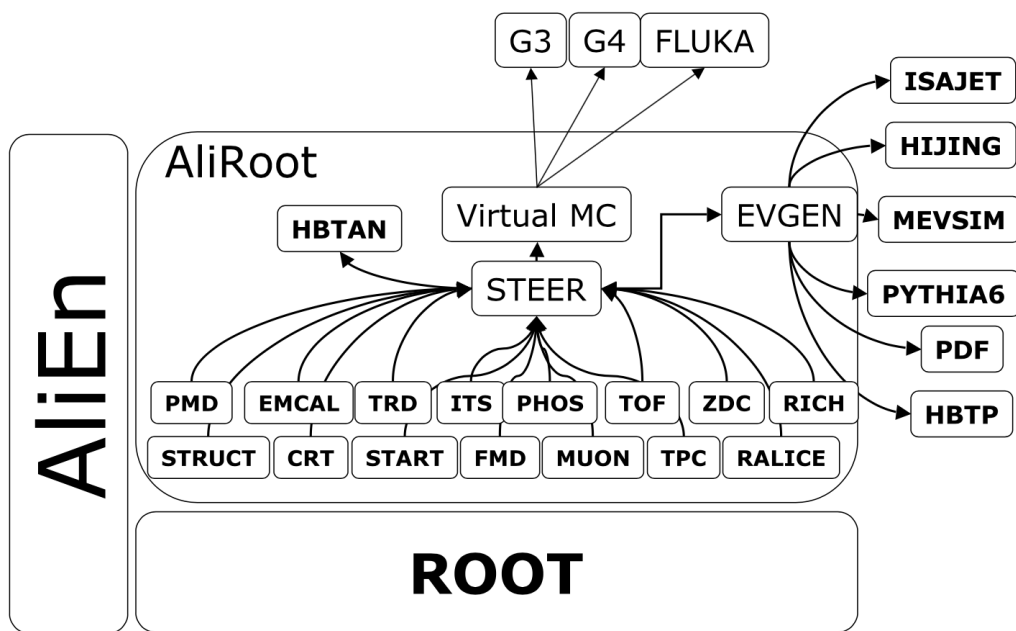


Figure 19: Schematic view of the AliRoot framework

944 **5 Measurement of $\Xi(1530)^0$ production in p–Pb and Pb–Pb**

945 The measurement of resonance production in p–Pb collisions helps to disentangle cold
946 nuclear matter effects from genuine hot medium effects and contribute to the study of
947 the system size dependence of re-scattering in the hadronic phase. And the measurement
948 in ultra-relativistic heavy-ion collisions such as Pb–Pb collisions, provide information on
949 the properties of hadronic medium and different stage of its evolution. In order to study
950 the particle production mechanism in the hadronic phase between the chemical and ki-
951 netic freeze-out, the $\Xi(1530)^0$ resonance production at mid-rapidity ($-0.5 < y_{\text{CMS}} < 0$) is
952 measured in p–Pb collisions $\sqrt{s_{\text{NN}}} = 5.02$ TeV and in Pb–Pb collisions with $|y| < 0.5$ at
953 $\sqrt{s_{\text{NN}}} = 2.76$ TeV with the ALICE experiment, via the reconstruction of its hadronic decay
954 into $\Xi\pi$.

955 **5.1 $\Xi(1530)^0$ -reconstruction**

956 The Ξ^{*0} production in p–Pb and Pb–Pb collisions at mid-rapidity has been studied in dif-
957 ferent multiplicity classes, from very central to peripheral collisions. The analysis strategy
958 is based on the invariant mass study of the reconstructed pairs (referred to as the candi-
959 dates) whose provenance could be the decay of a Ξ^{*0} baryon into charged particles. The
960 decay products (also called daughters in the text) are identified as oppositely charged Ξ and
961 π among the tracks reconstructed in the central barrel. The event selection, track selec-
962 tion and the particle identification strategy is described. The raw signal yield is extracted
963 by fitting the background-subtracted invariant mass distribution in several transverse mo-
964 mentum intervals. In order to extract the p_{T} -dependent cross section, these yields are
965 corrected for efficiency. The p_{T} -dependent correction due to the detector acceptance and
966 reconstruction efficiency, $(\text{Acc} \times \epsilon_{\text{rec}})(\text{pt})$, is computed from a Monte Carlo simulation.
967 The absolute normalisation is then performed, by dividing for the number of the events in
968 each multiplicity and centrality classes.

969 **5.1.1 Data sample and event selection**

970 A description of the ALICE detector and of its performance during the LHC Run 1 (2010–
971 2013) can be found in [31, 43]. The data sample in the analysis from Pb–Pb collisions with
972 energy of $\sqrt{s_{\text{NN}}} = 2.76$ obtained during 2011 and the sample of p–Pb run at $\sqrt{s_{\text{NN}}} = 5.02$
973 TeV was recorded in 2013.

974 Due to the asymmetric energies of the proton (4 TeV) and lead ion (1.57 A TeV) beams,
975 the centre-of-mass system in the nucleon-nucleon frame is shifted in rapidity by $\Delta y_{\text{NN}} =$
976 0.465 towards the direction of the proton beam with respect to the laboratory frame of
977 the ALICE detector [5]. For the analysed p–Pb data set, the direction of the proton beam
978 was towards the ALICE muon spectrometer, the so-called “C” side, standing for negative
979 rapidities; conversely, the Pb beam circulated towards positive rapidities, labelled as “A”

980 side in the following. The analysis in this paper was carried out at midrapidity, in the
981 rapidity window $-0.5 < y_{\text{CMS}} < 0$.

982 The minimum-bias trigger during the p–Pb run was configured to select events by
983 requiring a logical OR of signals in V0A and V0C [43], two arrays of 32 scintillator detectors
984 covering the full azimuthal angle in the pseudo-rapidity regions $2.8 < \eta_{\text{lab}} < 5.1$ and
985 $-3.7 < \eta_{\text{lab}} < -1.7$, respectively [44]. In the data analysis it was required to have a
986 coincidence of signals in both V0A and V0C in order to reduce the contamination from
987 single-diffractive and electromagnetic interactions. Out of this sample in p–Pb collision
988 events about 109.3 million events, 93.9 million events satisfy the following selection criteria
989 and have been actually used for the analysis.

990 The Pb–Pb collisions data sample was selected by online centrality trigger requiring a
991 signal in the forward V0 detectors[38] to record enhanced data in central collision. The
992 data consists of 24.8 million events in most central collisions (0-10%), 21.8 million events in
993 semi-central collisions (10-50%) and 3.5 million events with minimum-bas trigger (0-90%).
994 Among 49.6 million events in total, 43.0 million events have been analyzed as passed the
995 criteria below.

- 996 • Events with z-coordinate of primary vertex (V_z) falling within ± 10 cm from the
997 interaction point
- 998 • Rejection of pile-up event
- 999 • Requiring primary tracks to have at least one hit in one of the two innermost layers
1000 of the ITS (silicon pixel detector, SPD)
- 1001 • p–Pb: multiplicity ranges in percentile (V0A): 0-20%, 20-40%, 40-60%, 60-100% and
1002 MB(0-100%)
- 1003 • Pb–Pb: centrallity classes (V0A and V0C): 0-10%, 10-40%, 40-80% and MB (0-80%)

1004 The distribution of the vertex z position of the accepted events in p–Pb collision is
1005 reported on left panel in Figure 20 and corresponding figure but obtained from Pb–Pb
1006 collisions is shown on right panel in Figure. 20. Events with $|V_z| < 10$ cm have been used
1007 to ensure a uniform acceptance in the central pseudo-rapidity region, $|\eta| < 0.8$, where the
1008 analysis is performed. This cut reduces the total number of events to 97.5 million events,
1009 that is the $\sim 89.2\%$ of the initial sample in p–Pb collisions and 43.04 million events which
1010 is $\sim 86.8\%$ of the initial sample in Pb–Pb collisions are survived.

1011 Fig. 21 shows the multiplicity distribution of the accepted events in p–Pb collision
1012 divided in bins of percentile. The each color on the histogram indicate the multiplicity
1013 ranges used in this analysis. Corresponding events for each multiplicity range are in Table
1014 8.

1015 The distribution of centrality in each trigger used to select the events in Pb–Pb collision
1016 is shown in Fig. 22 and the reason why the centrality has step structure is that there are

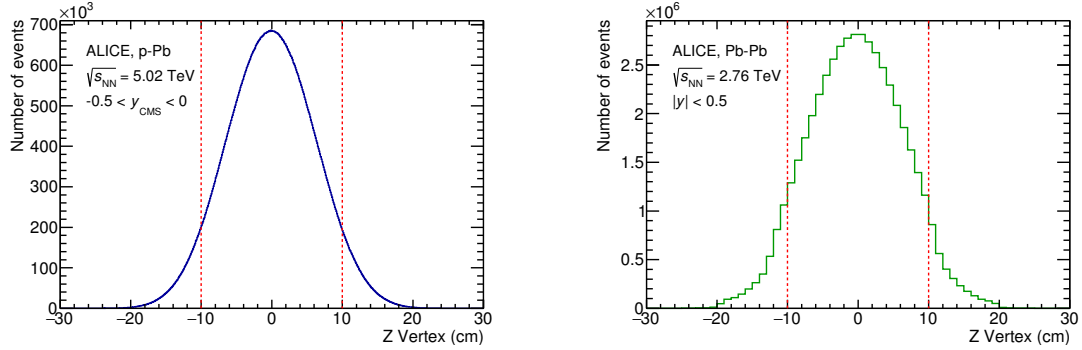


Figure 20: Vertex-z coordinate distribution of the accepted events in p–Pb collision(Left) and in Pb–Pb collisions(Right). The red dashed line indicates vertex cut

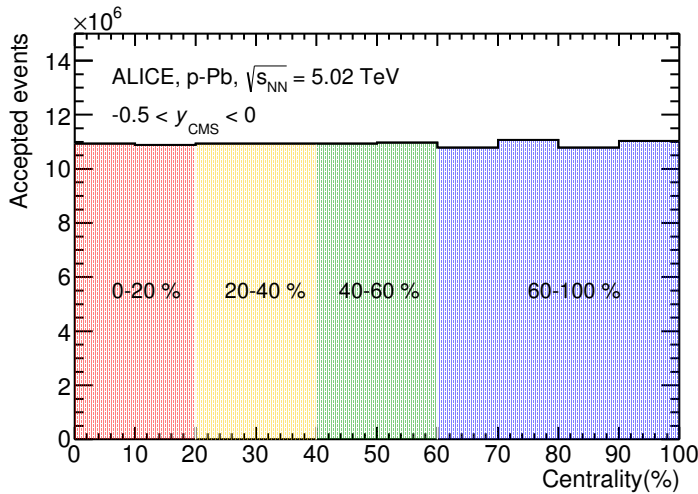


Figure 21: Multiplicity distribution of accepted events in p–Pb collision in percentile. The each color and labels define the four intervals in which the analysis is performed.

1017 three different trigger classes classified by the amplitude threshold on VZERO detector.
 1018 Because the distribution of events as function of centrality is not a flat, this may lead to
 1019 additional bias, in particular when one needs to combine the results from different triggers.
 1020 For example, events from 40-80% centrality bin have bias with high statistics in 40-60%. In
 1021 order to avoid this effect, we have applied a flattening procedure to have flat distribution
 1022 of events as function of centrality. A brief explanation of the method is below :

- 1023 1. Histograms are obtained for the effective mass distribution in 1% centrality bins and
 1024 for the centrality distribution

 1025 2. The effective mass distributions are scaled in each 1% centrality bin by a factor:
 1026 Factor = N_{event} in 20-40% / 20 / N_{event} in current 1% bin

 1027 3. Each bin in the centrality distribution is scaled using the factor described above

 1028 4. Histograms are added for centrality bins of interest: 0-10%, 10-40%, 40-80%, 0-80%

1029 The resulting number of events in each centrality classes is summarized in Table 8.

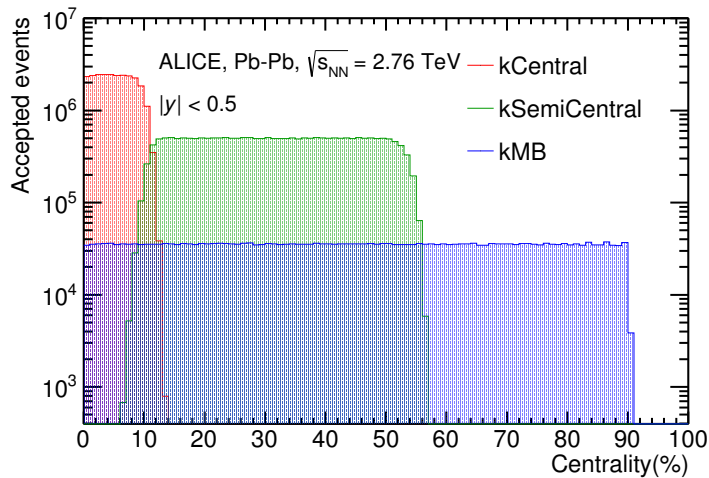


Figure 22: Centrality distribution of three different trigger classes.

p-Pb	0-20%	21.82×10^6
	20-40%	21.86×10^6
	40-60%	21.91×10^6
	60-100%	43.68×10^6
Pb-Pb	0-10%	5.58×10^6
	10-40%	16.73×10^6
	40-80%	22.31×10^6

Table 8: Number of accepted and analyzed events per multiplicity/centrality interval

1030 5.1.2 Track and topological selection

1031 In comparison with the Ξ^{*0} analysis carried out in pp collisions at $\sqrt{s} = 7$ TeV [7], track
 1032 and topological selections were revised and adapted to the p-Pb dataset. Pions from strong
 1033 decays of Ξ^{*0} were selected according to the criteria for primary tracks. As summarized
 1034 in Table 9, all charged tracks were selected with $p_T > 0.15$ GeV/c and $|\eta_{\text{lab}}| < 0.8$,
 1035 as described in Ref. [43]. The primary tracks were chosen with the Distance of Closest
 1036 Approach (DCA) to PV of less than 2 cm along the longitudinal direction (DCA_z) and
 1037 lower than $7\sigma_r$ in the transverse plane (DCA_r), where σ_r is the resolution of DCA_r . The σ_r
 1038 is strongly p_T -dependent and lower than 100 μm for $p_T > 0.5$ GeV/c [43]. To ensure a good
 1039 track reconstruction quality, candidate tracks were required to have at least one hit in one
 1040 of the two innermost layers (SPD) of the ITS and to have at least 70 reconstructed points in
 1041 the Time Projection Chamber (TPC), out of a maximum of 159. The Particle IDentification
 1042 (PID) criteria for all decay daughters are based on the requirement that the specific energy
 1043 loss (dE/dx) is measured in the TPC within three standard deviations (σ_{TPC}) from the
 expected value (dE/dx_{exp}), computed using a Bethe-Bloch parametrization [43].

Common track selections	$ \eta_{\text{lab}} $	< 0.8
	p_T	> 0.15 GeV/c
	PID $ (\text{d}E/\text{d}x) - (\text{d}E/\text{d}x)_{\text{exp}} $	$< 3 \sigma_{\text{TPC}}$
Primary track selections	DCA_z to PV	< 2 cm
	DCA_r to PV	$< 7\sigma_r$ - $10\sigma_r$ (p_T)
	number of SPD points	≥ 1
	number of TPC points	> 70
	χ^2 per cluster	< 4

Table 9: Track selections common to all decay daughters and primary track selections applied to the charged pions from decays of Ξ^{*0} .

1044 Since pions and protons from weak decay of Λ ($c\tau = 7.89$ cm [1]) and pions from weak
 1045 decay of Ξ^- ($c\tau = 4.91$ cm [1]) are produced away from the PV, specific topological and
 1046

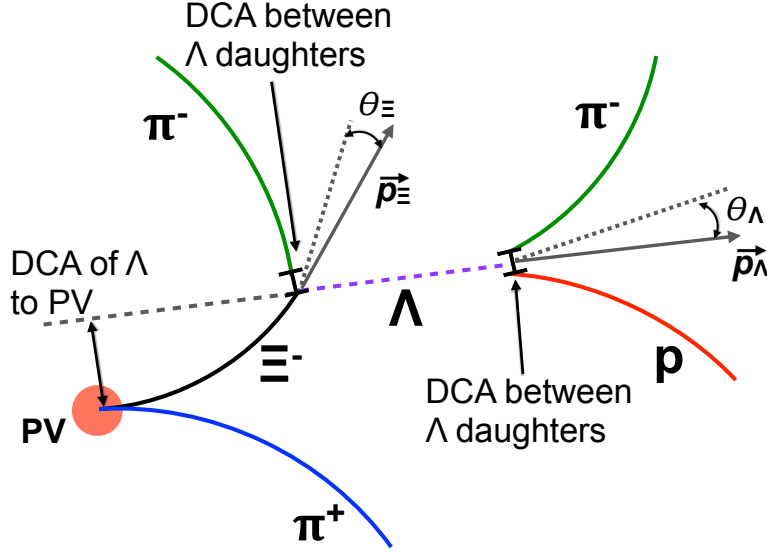


Figure 23: Sketch of the decay modes for Ξ^{*0} and depiction of the track and topological selection criteria.

¹⁰⁴⁷ track selection criteria, as summarized in Table 10, were applied [6, 7, 45].

Topological cuts	p-Pb	Pb-Pb
DCA _r of Λ decay products to PV	> 0.06 cm	> 0.11 cm
DCA between Λ decay products	< 1.4 cm	< 0.95 cm
DCA of Λ to PV	> 0.015 cm	> 0.06
$\cos\theta_\Lambda$	> 0.875	> 0.998
$r(\Lambda)$	$0.2 < r(\Lambda) < 100$ cm	$0.2 < r(\Lambda) < 100$ cm
$ M_{p\pi} - m_\Lambda $	< 7 MeV/ c^2	< 7 MeV/ c^2
DCA _r of pion (from Ξ^-) to PV	> 0.015 cm	> 0.035 cm
DCA between Ξ^- decay products	< 1.9 cm	< 0.275
$\cos\theta_\Xi$	> 0.981	> 0.9992
$r(\Xi^-)$	$0.2 < r(\Xi^-) < 100$ cm	$0.2 < r(\Xi^-) < 100$ cm
$ M_{\Lambda\pi} - m_\Xi $	< 7 MeV/ c^2	< 7 MeV/ c^2

Table 10: Topological and track selection criteria.

¹⁰⁴⁸ In the analysis of Ξ^{*0} , Λ and π from Ξ^- were selected with a DCA of less than 1.9 cm
¹⁰⁴⁹ and with a DCA_r to the PV greater than 0.015 cm. The Λ daughter particles (π and p)

1050 were required to have a DCA_r to the PV greater than 0.06 cm, while the DCA between the
1051 two particles was required to be less than 1.4 cm. Cuts on the invariant mass, the cosine of
1052 the pointing angle ($\theta_\Lambda, \theta_\Xi$) and the radius of the fiducial volume ($r(\Lambda), r(\Xi)$) in Table 10
1053 were applied to optimize the balance of purity and efficiency of each particle sample.

1054 **5.1.3 Particle identification**

1055 PID selection criteria are applied for

- 1056 1. π^\pm (last emitted π) and proton from Λ
1057 2. π^\pm (second emitted π) from Ξ^\pm
1058 3. π^\pm (first emitted π) from $\Xi(1530)^0$

1059 by using TPC. On TPC dE/dx versus momentum distribution, 3σ cuts are applied to TPC
1060 for selecting each of the particles. The TPC dE/dx selection allows to have better signal
1061 with $\sim 20\%$ increase of significance.

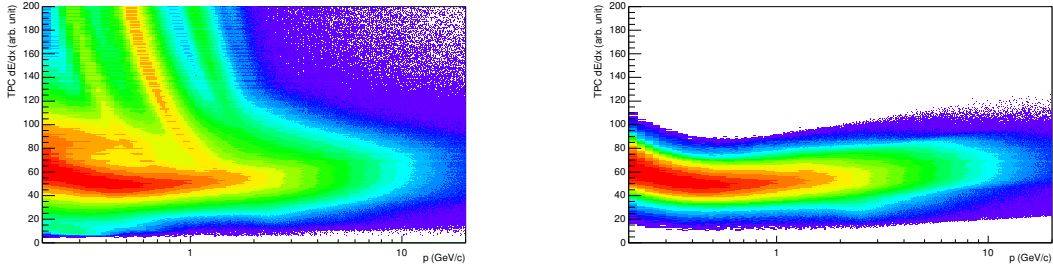


Figure 24: TPC dE/dx as function of transverse momentum for total (top) and selected first emitted π in 3σ (bottom)

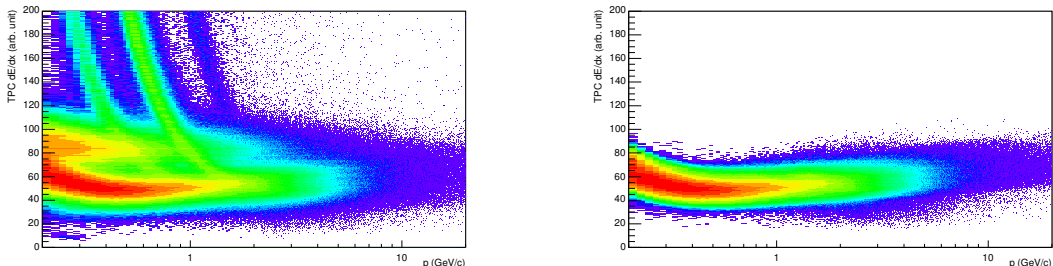


Figure 25: TPC dE/dx as function of transverse momentum for total (top) and selected second emitted π in 3σ (bottom)

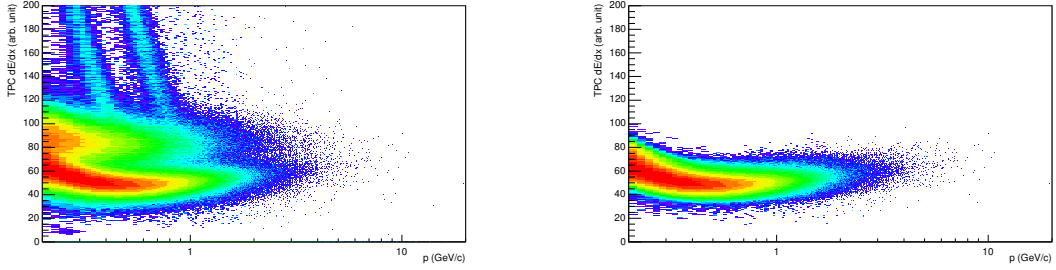


Figure 26: TPC dE/dx as function of transverse momentum for total (top) and selected last emitted π in 3σ (bottom)

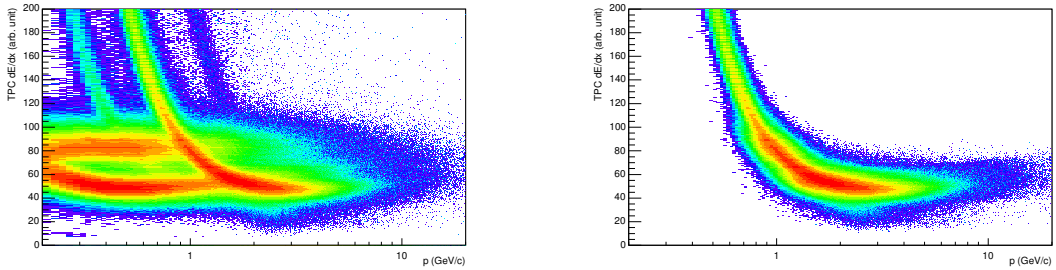


Figure 27: TPC dE/dx as function of transverse momentum for total (top) and selected proton in 3σ (bottom)

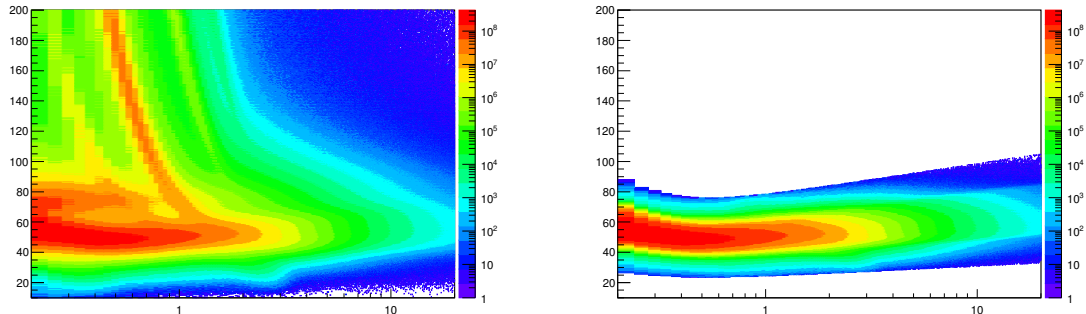


Figure 28: TPC dE/dx as function of transverse momentum for total (top) and selected first emitted π in 3σ (bottom)

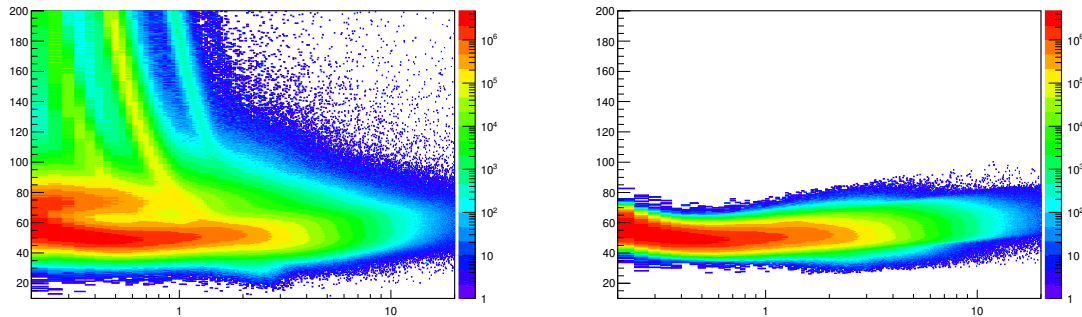


Figure 29: TPC dE/dx as function of transverse momentum for total (top) and selected second emitted π in 3σ (bottom)

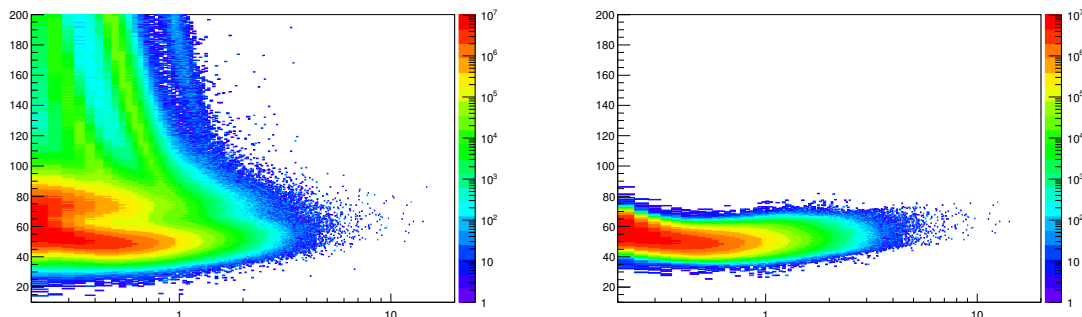


Figure 30: TPC dE/dx as function of transverse momentum for total (top) and selected last emitted π in 3σ (bottom)

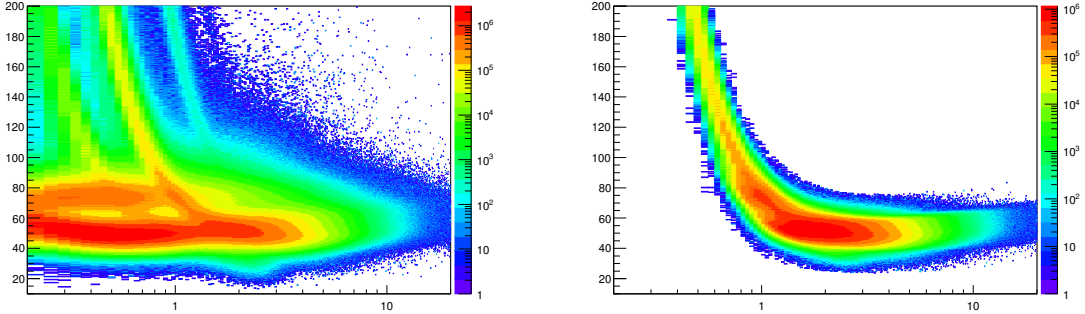


Figure 31: TPC dE/dx as function of transverse momentum for total (top) and selected proton in 3σ (bottom)

1062 5.1.4 Signal extraction

1063 The Ξ^{*0} signals were reconstructed by invariant-mass analysis of candidates for the decay
 1064 products in each transverse momentum interval of the resonance particle, and for each
 1065 multiplicity class. The $\Xi^-\pi^+(\Xi^+\pi^-)$ invariant mass distribution is reported in Figure 5.1.4
 1066 for semi-central events (20-40%) in p–Pb collisions and Figure 5.1.4 for central events(0-
 1067 10%) in Pb–Pb collisions.

1068 Since the resonance decay products originate from a position which is indistinguishable
 1069 from the PV, a significant combinatorial background is present. In order to extract
 1070 $\Xi(1530)^0$ signal it is necessary to remove or, at least reduce, the combinatorial background.
 1071 For this analysis, this has been done with the event mixing (EM) technique, by combining
 1072 uncorrelated decay products 20 different events in p–Pb (5 different events in Pb–Pb). The
 1073 events for the mixing have been selected by applying the similarity criteria to minimise
 1074 distortions due to different acceptances and to ensure a similar event structure, only tracks
 1075 from events with similar vertex positions z ($|\Delta z| < 1$ cm) and track multiplicities n ($|\Delta n| <$
 1076 10) were taken.

1077 The mixed-event background distributions were normalised to two fixed regions,
 1078 $1.49 < M_{\Xi\pi} < 1.51 \text{ GeV}/c^2$ and $1.56 < M_{\Xi\pi} < 1.58 \text{ GeV}/c^2$, around the Ξ^{*0} mass
 1079 peak (Figure 5.1.4 and 5.1.4). These regions were used for all p_T intervals and multiplicity
 1080 classes, because the background shape is reasonably well reproduced in these regions and
 1081 the invariant-mass resolution of the reconstructed peaks appears stable, independently of
 1082 p_T . The uncertainty on the normalisation was estimated by varying the normalisation
 1083 regions and is included in the quoted systematic uncertainty for the signal extraction (Section 5.4).

1085 After the background subtraction, the resulting distribution is shown in Figure 5.1.4
 1086 and 5.1.4. In order to obtain raw yields, a combined fit of a first-order polynomial for

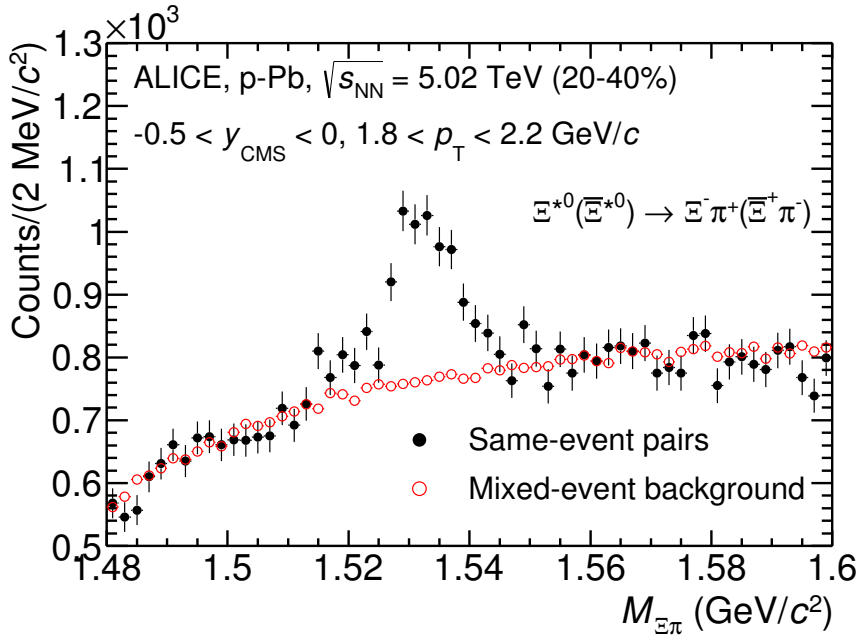


Figure 32: The $\Xi^\pm\pi^\pm$ invariant mass distribution (Same-event pairs) in $1.8 < p_T < 2.2 \text{ GeV}/c$ and for the multiplicity class 20-40%. The background shape, using pairs from different events (Mixed-event background), is normalised to the counts in $1.49 < M_{\Xi\pi} < 1.51 \text{ GeV}/c^2$ and $1.56 < M_{\Xi\pi} < 1.58 \text{ GeV}/c^2$.

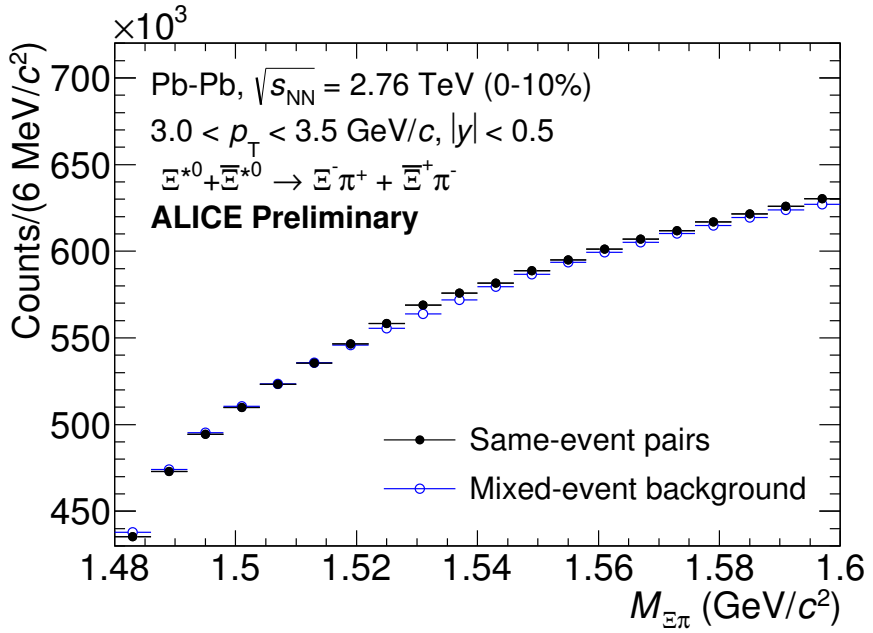


Figure 33: The $\Xi^\pm\pi^\pm$ invariant mass distribution (Same-event pairs) in $3.0 < p_T < 3.5$ GeV/c and for the centrality class 0-10%. The background shape, using pairs from different events (Mixed-event background), is normalised to the counts in $1.49 < M_{\Xi\pi} < 1.51$ GeV/c² and $1.56 < M_{\Xi\pi} < 1.58$ GeV/c².

1087 the residual background and a Voigtian function (a convolution of a Breit-Wigner and a
 1088 Gaussian function accounting for the detector resolution) for the signal was used. The
 1089 mathematical form of fit function used in analysis is:

$$f(M_{\Xi\pi}) = \frac{Y}{2\pi} \frac{\Gamma_0}{(M_{\Xi\pi} - M_0)^2 + \frac{\Gamma_0^2}{4}} \frac{e^{-(M_{\Xi\pi} - M_0)/2\sigma^2}}{\sigma\sqrt{2\pi}} + bg(M_{\Xi\pi}) \quad (7)$$

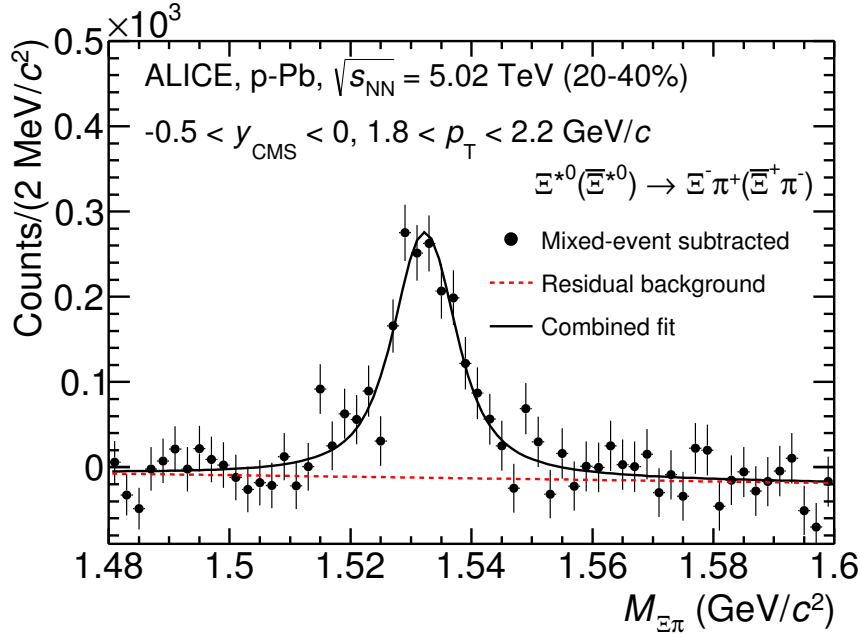


Figure 34: The invariant mass distribution after subtraction of the mixed-event background in p–Pb collisions. The solid curve represents the combined fit, while the dashed line describes the residual background.

1090 The mass parameter of the Voigtian fit (M_0) is left free within the fit range ($1.48 \text{ GeV}/c^2$
 1091 and $1.59 \text{ GeV}/c^2$). The overall invariant mass width of the Voigtian function is governed
 1092 by 2 parameters: σ and Γ_0 . The σ describes the broadening of the peak due to finite
 1093 detector resolution while Γ describes the intrinsic width of the resonance itself. The Γ_0 is
 1094 fixed to the PDG value of $9.1 \text{ MeV}/c$ for the $\Xi(1530)^0$. Because of lack of statistics, the
 1095 σ can be over estimated. Therefore the σ parameter is fixed to value derived from σ in
 1096 MB events which has largest statistics. The σ as function of p_T distribution in MB events
 1097 is shown in Figure. 36 and we also report invariant mass of $\Xi(1530)^0$ as function of p_T in
 1098 Figure. 37. The $\Xi(1530)^0$ raw yields have been extracted from the fit for the 4 multiplicity

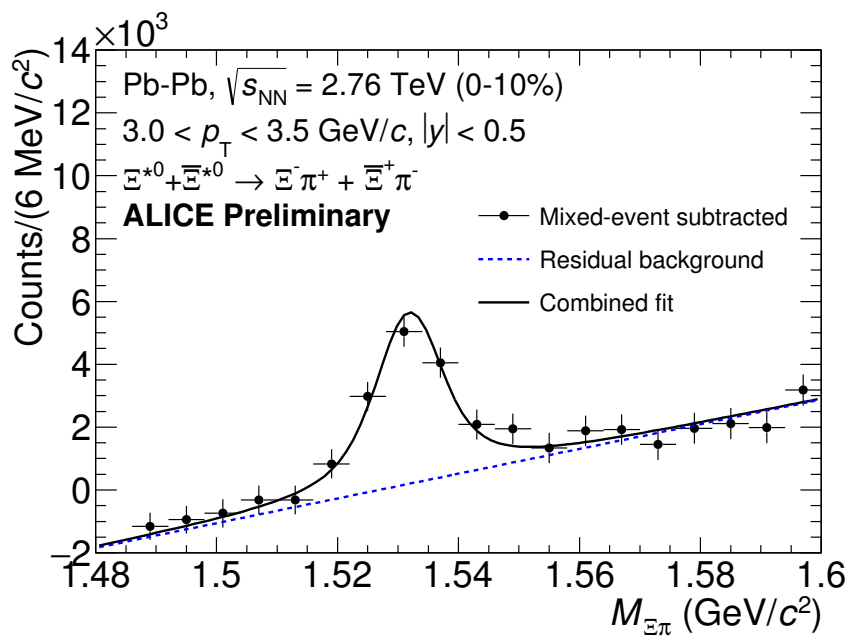


Figure 35: The invariant mass distribution after subtraction of the mixed-event background in Pb–Pb collisions. The solid curve represents the combined fit, while the dashed line describes the residual background.

¹⁰⁹⁹ bins (+ NSD events) in p–Pb and 4 centrality bins in Pb–Pb collisions and the yields as
¹¹⁰⁰ function of p_T are shown in Figure 38.

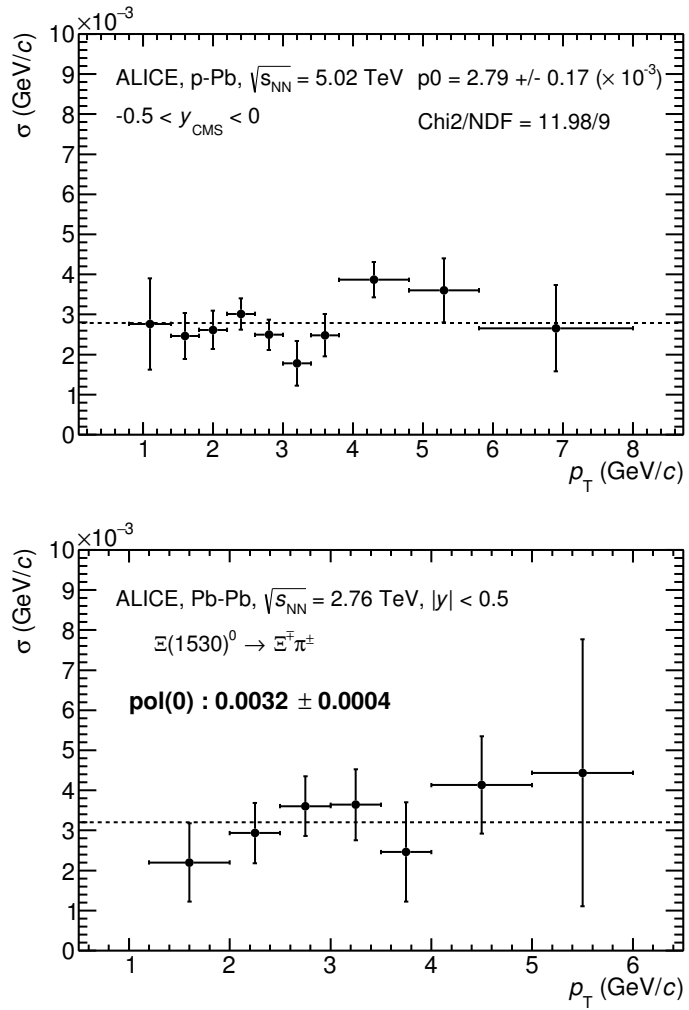


Figure 36: σ fit parameters as a function of p_T in MB in p–Pb collisions (top) and in Pb–Pb collisions (bottom).

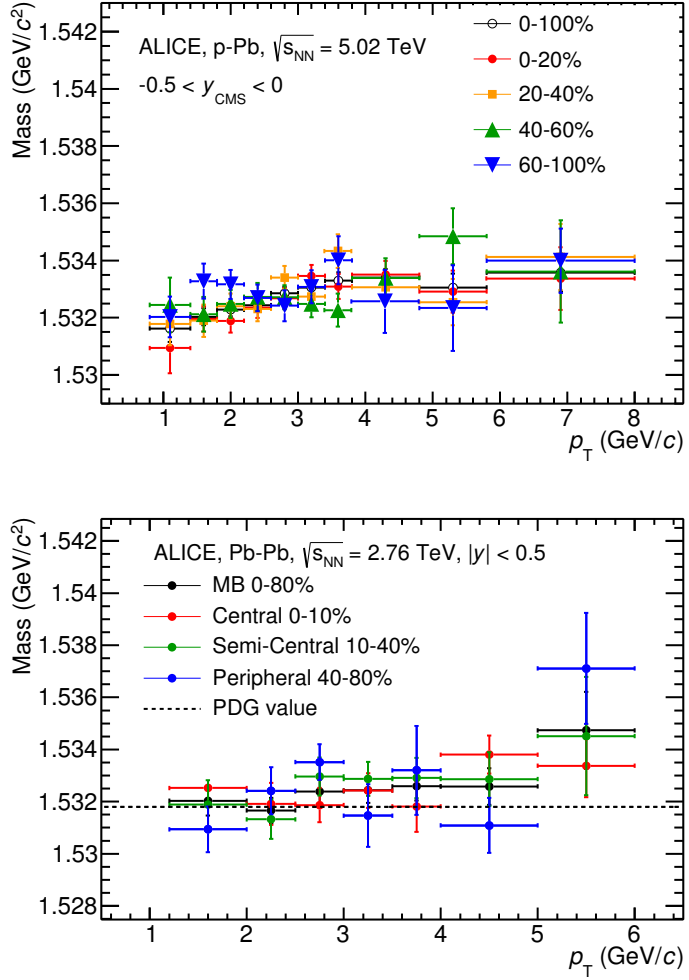


Figure 37: $\Xi(1530)^0$ -mass obtained from fit of the Voigtian peak as a function of p_T in each multiplicity classes in p-Pb collisions (top) and the different centrality classes in Pb-Pb (bottom).

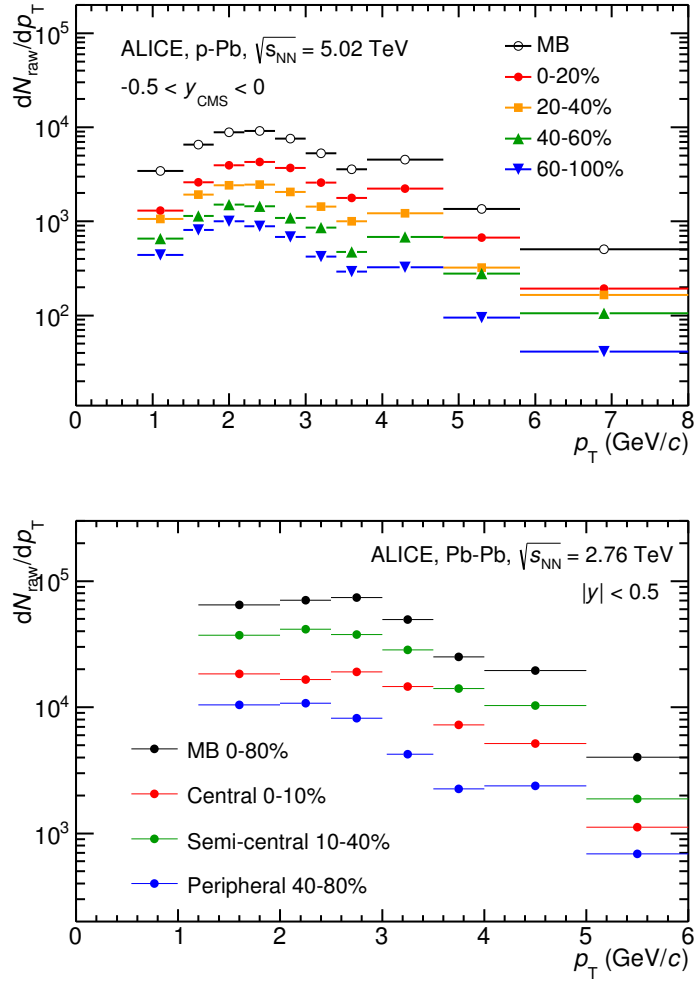


Figure 38: $\Xi(1530)^0$ -raw spectra obtained from fit of the Voigtian peak and a polynomial residual background for different multiplicities in p-Pb collisions (top) and Pb-Pb collisions (bottom). Only the statistical error is reported.

1101 **5.2 Efficiency correction**

1102 The raw yields were corrected for the geometrical acceptance and the reconstruction effi-
 1103 ciency ($A \times \epsilon$) of the detector (Figure. 39). By using the DPMJET 3.05 event generator [46]
 1104 and the GEANT 3.21 package [47], a sample of about 100 million p–Pb events was sim-
 1105 ulated and reconstructed in order to compute the corrections. The distributions of $A \times \epsilon$
 1106 were obtained from the ratio between the number of reconstructed Ξ^{*0} and the number of
 1107 generated particle in the same p_T and rapidity interval. Since the correction factors for
 1108 different multiplicity classes are in agreement with those from MB events within statistical
 1109 uncertainty, the latter were used for all multiplicity classes.

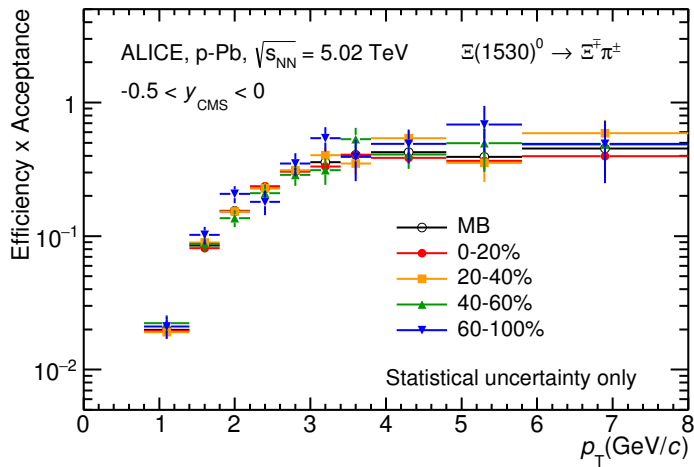


Figure 39: $\Xi(1530)^0$ -raw spectra obtained from fit of the Voigtian peak and a polynomial residual background for different multiplicities. Only the statistical error is reported.

1110 Because the generated $\Xi(1530)^0$ spectra have different shapes than the measured $\Xi(1530)^0$
 1111 spectra, it is necessary to weight the generated and reconstructed $\Xi(1530)^0$ spectra in these
 1112 simulations. Fig. 40 shows the generated and reconstructed $\Xi(1530)^0$ spectra plotted with
 1113 the (corrected) measured $\Xi(1530)^0$ spectrum for MB events and the Levy fit of that mea-
 1114 sured spectrum. The generated and measured $\Xi(1530)^0$ spectra have different behaviours
 1115 for the range $0.5 < p_T < 1$ GeV/ c . The generated $\Xi(1530)^0$ spectrum decreases with
 1116 increasing p_T over this range, while the fit of the measured $\Xi(1530)^0$ spectrum reaches a
 1117 local maximum in this range. The correction ϵ is observed to change rapidly over this
 1118 p_T range. It is therefore necessary to weight the generated spectrum so that it has the
 1119 shape of the measured $\Xi(1530)^0$ spectrum (and to apply corresponding weights to the re-
 1120 constructed $\Xi(1530)^0$ spectrum). An iterative procedure is performed to determine the
 1121 correct weighting (and therefore the correct ϵ).

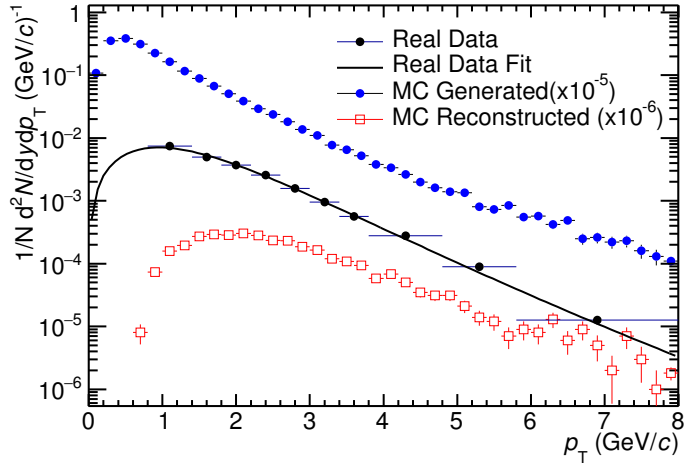


Figure 40: Real corrected $\Xi(1530)^0$ spectrum (black) for the minimum bias with Levy fit (black curve). Also shown are the unweighted generated (blue) and reconstructed (red) $\Xi(1530)^0$ spectra.

- 1122 1. The unweighted ϵ is calculated.
- 1123 2. This ϵ is used to correct the measured xis spectrum.
- 1124 3. The corrected $\Xi(1530)^0$ spectrum is fit.
- 1125 4. This fit is used to weight the simulated xis spectra. A p_T dependent weight is applied
1126 to the generated xis spectrum so that it follows the fit. The same weight is applied
1127 to the reconstructed xis spectrum.
- 1128 5. The (weighted) ϵ is calculated.
- 1129 6. Steps 2-5 are repeated (with the weighted ϵ from step 5 used as the input for step 2)
1130 until the ϵ values are observed to change by < 0.1% (relative) between iterations. It
1131 is observed that four iterations are sufficient for this procedure to converge.

1132 Finally, the re-weighted efficiency is obtained and the distribution as function of p_T is
1133 shown in Figure 41.

1134 In order to obtain the correction factor dedicated in Pb-Pb collisions, MC events are
1135 generated using Heavy Ion Jet Interaction Generator (HIJING). The generated events are
1136 passed through a GEANT3 model of the ALICE experiment with a realistic description of
1137 the detector response. Because we have observed centrality dependent efficiency, the cen-
1138 trality dependent efficiencies have been applied to get corrected raw yield. The reweighting

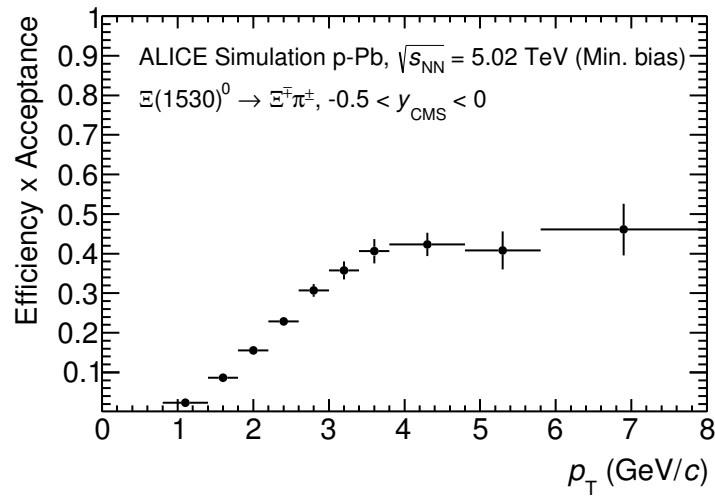


Figure 41: Efficiency as a function of p_T in minimum bias events in p–Pb collisions.

1139 approach which was used to correct the efficiency in p–Pb is also applied to the efficiency
 1140 obtained in Pb–Pb.

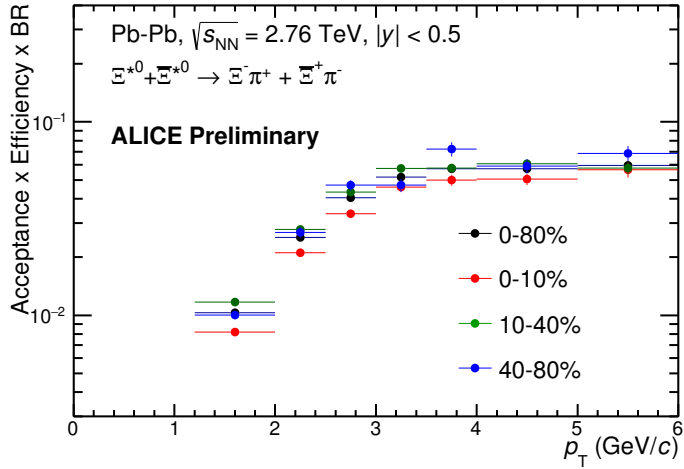


Figure 42: Efficiency as a function of p_T in different centrality classes in Pb–Pb collisions

1141 5.3 Corrected p_T -spectra

1142 The p_T spectrum is by the number of produced particles of a given type in the desired
 1143 interval of phase-space divided by the number of inelastic collisions. The spectrum is
 1144 calculated as:

$$\frac{1}{N} \times \frac{d^2N}{dydp_T} = \frac{1}{N_{E,PhysSel}} \times \frac{N_{raw}}{dp_T dy} \epsilon \frac{N_{total}^{MC}}{N_{post-PVcut}^{MC}}, \quad (8)$$

1145 where N_E represent the number inelastic collisions, the $\frac{dN}{dydp_T}$ is the yield per range of
 1146 rapidity y , per range in p_T . On the right hand side $N_{E,PhysSel}$ is the number of events
 1147 counted by the physics selection trigger. N_{raw} is the raw extracted number of particle in the
 1148 rapidity and p_T bin of width $\Delta y = 0.5$ in p–Pb ($\Delta y = 1.0$ in Pb–Pb) and Δp_T , respectively.
 1149 ϵ is the reconstruction efficiency estimated from Monte Carlo simulations. $\frac{N_{total}^{MC}}{N_{post-PVcut}^{MC}}$ is the
 1150 ratio of the total number of particle from MC divided by the number of particle from MC
 1151 after the Primary-Vertex cut is imposed. It takes into account the fraction of particle lost
 1152 after imposing the PV cut. We notice that for minimum-bias results in p–Pb, we adopted
 1153 a normalisation such that to provide result from non-single diffractive(NSD) cross-section.
 1154 The normalisation factor is 0.964 [5]. The obtained spectrum at MB and the spectrums
 1155 from different multiplicity classes in p–Pb are shown in Figure 43 and different centrality
 1156 classes in Pb–Pb are shown in Figure 44.

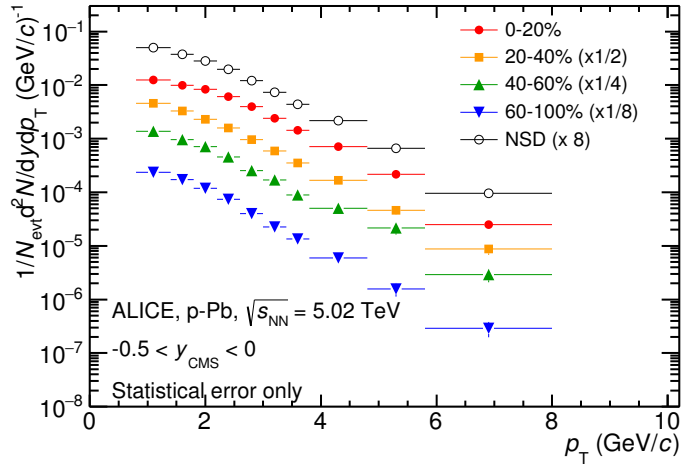


Figure 43: Corrected p_T -spectra of $\Xi(1530)^0$ in NSD and different multiplicity classes in p-Pb collisions.

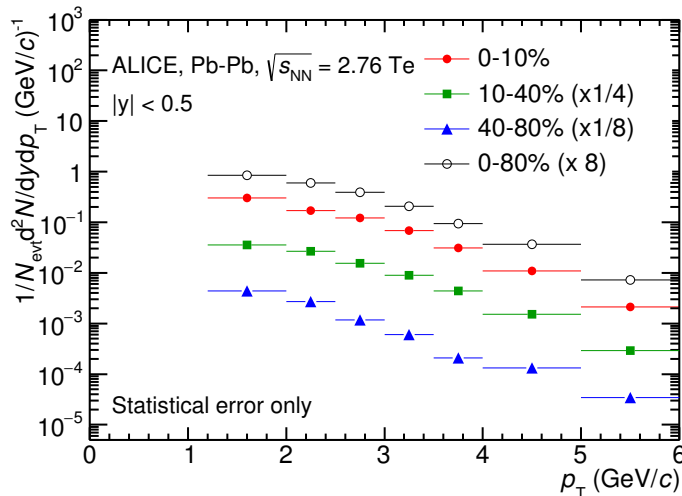


Figure 44: Corrected p_T -spectra of $\Xi(1530)^0$ in different centrality classes in Pb-Pb collisions.

1157 **5.4 Systematic uncertainties**

1158 The systematic uncertainties are calculated in seven principle groups. The procedure to ob-
1159 tain the systematic uncertainties is performed many times by varying the possible permuta-
1160 tion of the analysis parameter. The general strategy for evaluating systematic uncertainties
1161 is described as following:

- 1162 1. Choose one set of parameters for the analysis as default
- 1163 2. Observe the deviation of yield when one parameter is changed
- 1164 3. The systematic uncertainty is calculated for a given source as the RMS deviation of
1165 the available sources.
- 1166 4. The total systematic uncertainty, taking into account all the different sources, is the
1167 sum in quadrature of each source.

1168 To study the systematic effect we repeat the measurement by varying one parameter at
1169 a time. A Barlow [48] check has been performed for each measurement to verify whether it
1170 is due to a systematic effect or a statistical fluctuation. Let each measurement be indicated
1171 by $(y_i \pm \sigma_i)$ and the central value (default measurement) by $(y_c \pm \sigma_c)$, one can define $\Delta\sigma_i$
1172 (Eq. 9).

$$\Delta\sigma_i = \sqrt{(|\sigma_i^2 - \sigma_c^2|)} \quad (9)$$

1173 Then we calculate $n_i = \Delta y_i / \Delta\sigma_i$, where $\Delta y_i = |y_c - y_i|$. If $n_i \leq 1.0$ then the effects
1174 are due to the statistical fluctuation and if $n_i > 1.0$ we apply consistency check. Since
1175 the alternate and default measurements are not statistically independent, an alternate
1176 measurement which is statistically consistent with the default measurement should not be
1177 used in calculating a systematic uncertainty. The difference between the two measurements
1178 is $\Delta = y_c - y_i$. The difference in quadrature of the uncertainties is calculated by Eq. 9. It
1179 could be possible to check if $\Delta < \sigma$ and exclude such cases from the systematic uncertainties.
1180 However, there can be statistical fluctuations for which $\Delta > \sigma$. If the variations between the
1181 default and alternate measurements are purely statistical, the distribution of Δ/σ should
1182 be a Gaussian with a mean value that is consistent with zero and a deviation σ consistent
1183 with unity. In this analysis, if the mean value is less than 0.1 and σ is less than 1, the
1184 variation passes the consistency check.

1185 Only the measurements which passed the Barlow check ($n_i > 1$) are used to determine
1186 the systematic uncertainty. For measurements $N > 2$, the systematic uncertainty has been
1187 determined as the RMS (eqn. 10) of the available measurements. If $N=2$, the absolute
1188 difference is assigned as systematic uncertainty.

$$\delta y_{syst.} = \sqrt{\frac{1}{N} \sum_i (y_i - \bar{y})^2} \quad (10)$$

1189 Here N is the total number of available measurements including y_c and \bar{y} is the average
1190 of value of the measurements. The measurement did not pass Barlow check, zero systematic
1191 uncertainty has been assigned to the value.

1192 By suing the way as explained above, all the main contributions to the systematic un-
1193 certainty of particle spectra have been studied. In particular those that comes from signal
1194 extraction, topological and kinematical selection cuts, track quality selection and $n\sigma$ TPC
1195 PID variation. the meaning of each source of systematic uncertainty studied is described
1196 in the following:

1197

1198 **Signal extraction**

1199 We have extracted the signal with varying the yield calculating method which contains
1200 the method of signal extraction by integrating the Voigtian fit function and bin counting.
1201 We also have varied the normalisation range which is related to the invariant mass region
1202 where the mixed events distribution is scaled to subtract the combinatorial background
1203 and different background estimator such as Like-Sign distribution and polynomial fit was
1204 taken account into the systematic source of signal extraction. The systematic uncertainty
1205 from signal extraction is sum in quadrature of three sources.

1206

1207 **Topological selection**

1208 To evaluate the stability of the chosen set of values for the topological cuts, loose and tight
1209 cuts have beed defined in order to vary by $\pm 10\%$ respectively. The parameters are changed
1210 once at a time. Total systematic uncertainty from topological selection is calculated by
1211 summation in quadrature of nine sources.

1212

1213 **TPC $N_{cluster}$ selection**

1214 The selection performed for the daughter tracks of the cascade is that $N_{cluster}$ is larger
1215 than 70 and the value has been varied to 60 and 80 in order to estimate the systematic
1216 uncertainty due to this selection.

1217

1218 **TPC dE/dx selection**

1219 In order to evaluate any potential effect due to the TPC dE/dx selection (U_{PID}), the N_σ
1220 selection was varied with $N = 2.5$ and 3.5 .

1221

1222 **p_T shape correction**

1223 As described in Section 5.2, due to the different shape of the measured and generated
1224 $\Xi(1530)^0$ spectra, we have applied reweighing procedure to the generated spectra to have
1225 same shape and this correction is added into contributor of systematic uncertainty as
1226 p_T shape correction.

1227

1228 **Mass window range selection**

1229 In order to select Ξ^\pm which is daughter particle of $\Xi(1530)^0$, we apply the mass window

1230 ± 7 MeV/ c^2 around $\Xi(1530)^0$ mass on $\Lambda\pi$ invariant mass distribution. The boundaries has
1231 been varied to ± 6 MeV/ c^2 and ± 8 MeV/ c^2 to estimate systematic uncertainty.

1232

1233 Vertex range selection

1234 The distribution of vertex-z is shown in Fig.20. The cut on $|Vz|$ was varied from the nominal
1235 ± 10 cm to ± 9 cm, ± 11 cm.

1236

1237 Material Budget and hadronic cross section

1238 A possible source of uncertainty comes from the description of the material, active (detecting area)
1239 or dead (structure and cable), that the particles cross during their travel in
1240 the MC with respect to the real material present in the detector. Such description could
1241 affect the reconstruction efficiency in different aspects (e.g. multiple scattering, energy
1242 loss). The value estimated by Ξ analysis [23] has been used in this study which gives 4%
1243 systematic uncertainty. In case of systematic uncertainty from hadronic cross section, we
1244 have inherited the value studied in previous measurement[49] which amount is 1%.

1245

1246 Tracking efficiency

1247 Systematic uncertainties from tracking efficiency from ITS + TPC combined track were
1248 assigned as 3% in p–Pb and 4% in Pb–Pb collision system.[49]
1249 (<https://twiki.cern.ch/twiki/bin/view/ALICE/TrackingEfficiencyCharged>)

1250

1251 Finally, total systematic uncertainty is sum in quadrature of sources listed above. Figure
1252 45 and Figure 46 show the total systematic uncertainty in minimum bias event and
1253 different multiplicity classes in p–Pb collisions, respectively. Again, Figure 47 and Figure
1254 48 present the total systematic uncertainty in minimum bias event and different centrality
1255 classes in Pb–Pb collisions.

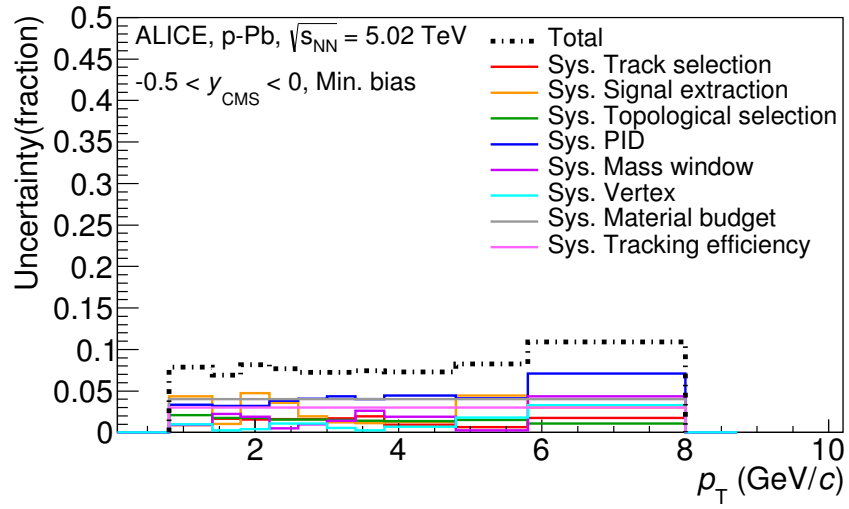


Figure 45: Summary of the contributions to the systematic uncertainty in minimum bias events in p–Pb collisions. The dashed black line is the sum in quadrature of all the contributions.

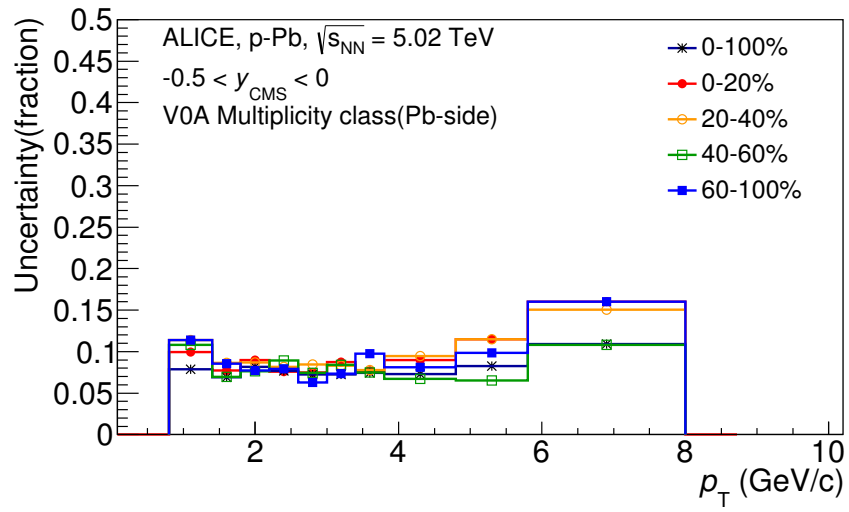


Figure 46: Systematic uncertainties for each multiplicity classes in p–Pb collisions.

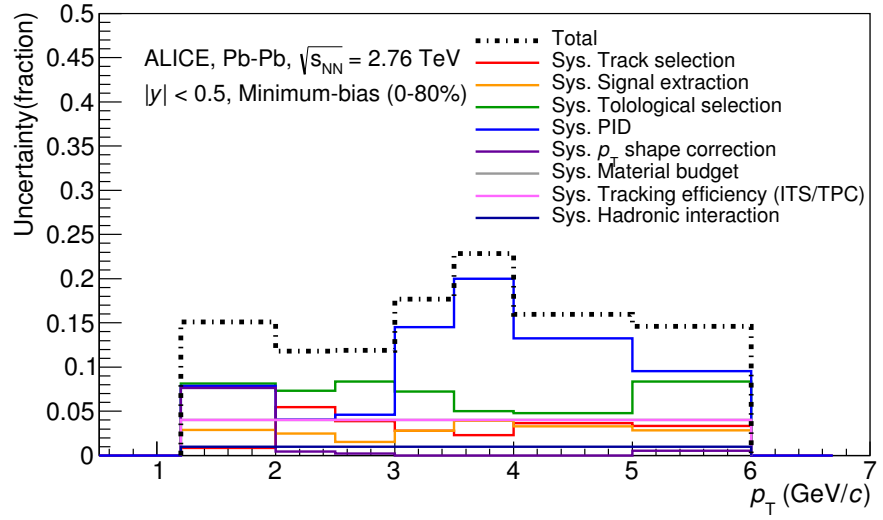


Figure 47: Summary of the contributions to the systematic uncertainty in minimum bias events in Pb–Pb collisions. The dashed black line is the sum in quadrature of all the contributions.

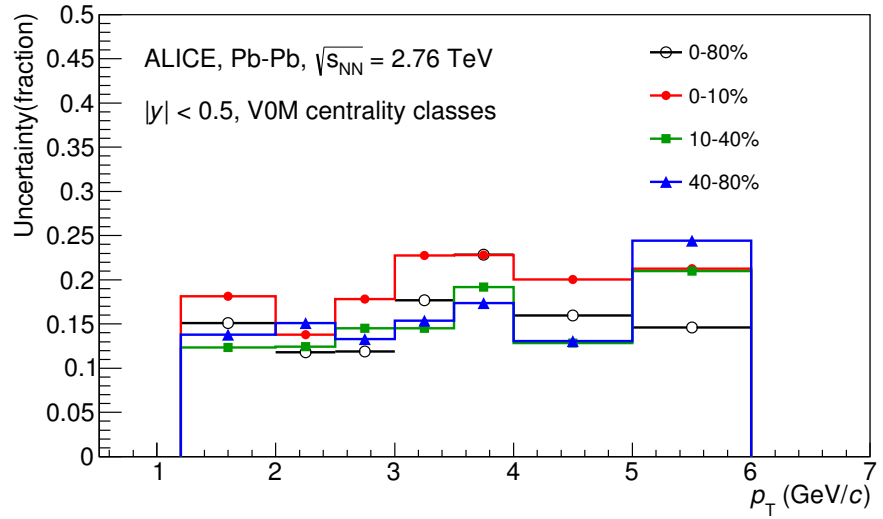


Figure 48: Systematic uncertainties for each multiplicity classes.

Source of uncertainty	p-Pb	Pb-Pb
<i>p</i> _T -dependent		
Tracking efficiency	3%	4%
Tracks selection	1-2%	1-5%
Topological selection	1-2%	5-8%
PID	3-7%	4-20%
Signal extraction	1-5%	1-4%
<i>p</i> _T shape correction	-	0-8%
Mass window (Ξ^\pm)	4%	-
Vertex selection	3%	-
<i>p</i> _T -independent		
Hadronic interaction	-	1%
Material budget	4%	4%
Branching ratio	0.3%	0.3%
Total	8-12%	9-25 %

Table 11: Summary of the systematic uncertainties on the differential yield, $d^2N/(dp_T dy)$. Minimum and maximum values in all p_T intervals and multiplicity classes in p–Pb, centrality classes in Pb–Pb are shown for each source.

1256 **5.5 $\Xi(1530)^0$ transverse momentum spectra**

1257 The raw yield shown in Figure 43 and 44 have been corrected for efficiency as described
 1258 in section 5.2. The measured spectra for $(\Xi(1530)^0 + \bar{\Xi}(1530)^0)/2$ are reported in Figure
 1259 49 for p–Pb collisions and Figure 50 for Pb–Pb collisions. The statistical and systematic
 1260 uncertainties are reported respectively as the error bars and the boxes on the plot. The
 1261 corrected yields for p–Pb collisions are measured with $0.8 < p_T < 8.0$ GeV/c while the
 1262 yields for Pb–Pb collisions are obtained with $1.2 < p_T < 6.0$ GeV/c due to difficulty of
 1263 signal extraction in low and high p_T region.

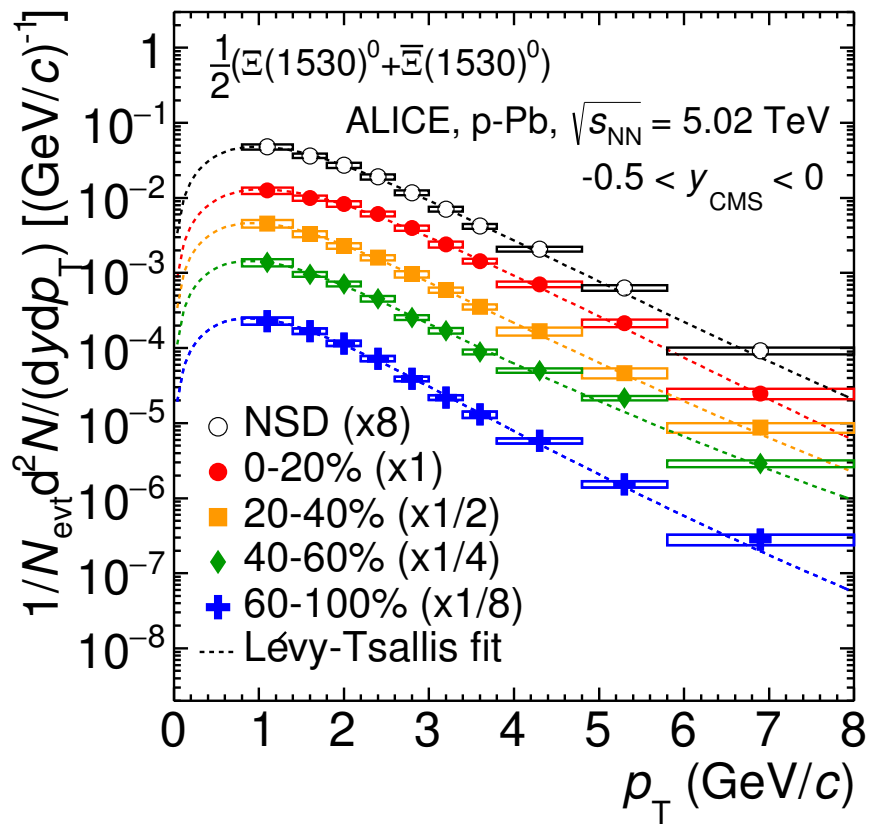


Figure 49: Corrected yields as function of p_T in NSD events and multiplicity dependent event classes in p-Pb collision system. Statistical uncertainties are presented as bar and systematical uncertainties are plotted as boxes.

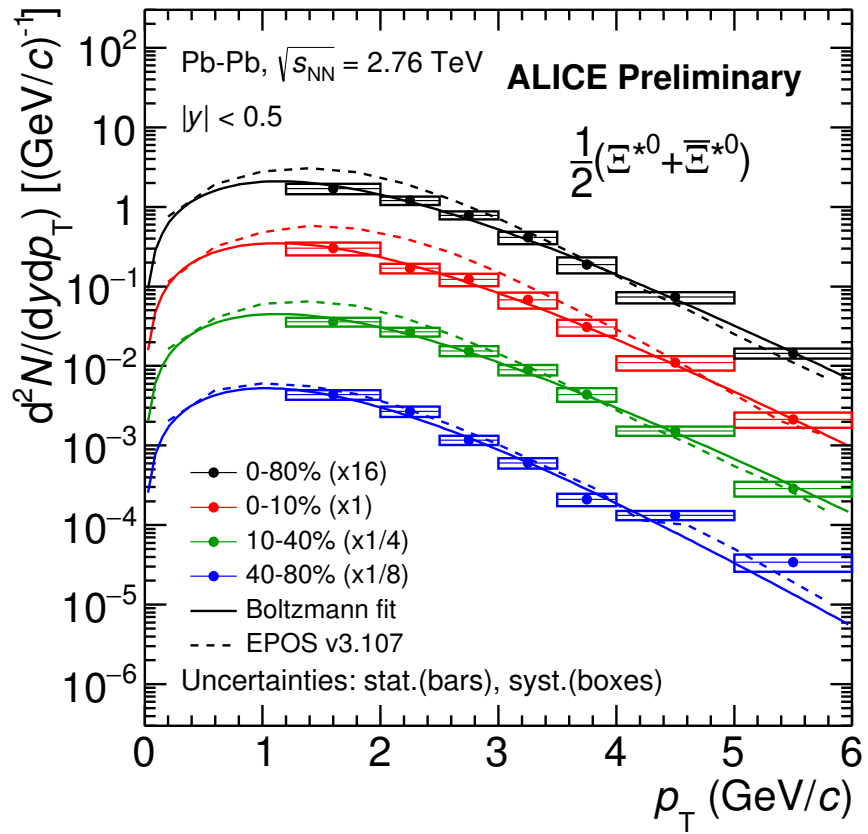


Figure 50: Corrected yields as function of p_T in different centrality classes in Pb–Pb collision system. Statistical uncertainties are presented as bar and systematical uncertainties are plotted as boxes.

1264 6 Further results and discussion

1265 The transverse momentum distributions of double-strange hyperon resonances, $\Xi(1530)^0$
1266 , produced in p–Pb collisions at $\sqrt{s_{\text{NN}}}= 5.02$ TeV and Pb–Pb collisions at $\sqrt{s_{\text{NN}}}= 2.76$
1267 TeV were measured in the mid-rapidity range and they have been already presented in
1268 Chapter 5. From the measurement, the $\langle p_{\text{T}} \rangle$ and integrated particle yield ratios with
1269 system size have been obtained. In the present Chapter these results are compared with
1270 model predictions and discussed in connection with the following topics:

- 1271 • Mean transverse momentum studies
- 1272 • Study of particle production mechanism in hadronic phase
- 1273 • Study of strangeness enhancement

1274 Most of the theoretical aspects related to these topics and, in particular, the description
1275 of the models already have been addressed in Chapter 2.

1276 6.1 Mean transverse momentum

1277 Figure 51 shows the mean transverse momentum $\langle p_{\text{T}} \rangle$ as a function of mean charged-
1278 particle multiplicity density $\langle dN_{\text{ch}}/d\eta_{\text{lab}} \rangle$ at midrapidity. The results for $\Xi(1530)^0$ are
1279 compared with those for other hyperons observed in p–Pb collisions at $\sqrt{s_{\text{NN}}}= 5.02$ TeV [4,
1280 6].

1281 Increasing trends from low to high multiplicities are observed for all hyperons. The
1282 mean transverse momenta increase by 20% as the mean charged-particle multiplicity in-
1283 creases from 7.1 to 35.6. This result is similar to the one obtained for the other hyperons.
1284 Furthermore, a similar increase has been observed also for K^{\pm} , K_S^0 , $K^*(892)^0$ and ϕ [5],
1285 whereas protons are subject to a larger ($\sim 33\%$) increase in the given multiplicity range,
1286 as discussed also in Ref. [4].

1287 In all multiplicity classes, the $\langle p_{\text{T}} \rangle$ follows an approximate mass ordering:

- 1288 • $\langle p_{\text{T}} \rangle_{\Lambda} < \langle p_{\text{T}} \rangle_{\Xi^-} \simeq \langle p_{\text{T}} \rangle_{\Sigma^{*\pm}} < \langle p_{\text{T}} \rangle_{\Xi^{*0}} < \langle p_{\text{T}} \rangle_{\Omega^-}$

1289 The $\langle p_{\text{T}} \rangle$ of $\Sigma^{*\pm}$ looks systematically lower than the $\langle p_{\text{T}} \rangle$ of Ξ^- , despite the larger mass
1290 of $\Sigma^{*\pm}$. The uncertainties, however, are too large to draw any conclusion on possible hints
1291 of violation of the mass hierarchy. This hierarchy of mass-ordering, also including D^0 and
1292 J/ψ in the comparison, is displayed in Figure 52. Note, however, that the D^0 and J/ψ
1293 were measured in different rapidity ranges: $|y_{\text{CMS}}| < 0.5$ [8] ($|y_{\text{CMS}}| < 0.9$ [9]) for D^0 (J/ψ)
1294 in pp and $-0.96 < y_{\text{CMS}} < 0.04$ [8] ($-1.37 < y_{\text{CMS}} < 0.43$ [10]) for D^0 (J/ψ) in p–Pb, and
1295 the results for D^0 and J/ψ in p–Pb collisions are for the 0–100% multiplicity class. This
1296 mass dependence is observed in both p–Pb and pp collisions. It was observed also by the
1297 STAR collaboration [50] in MB pp, MB d–Au and central Au–Au collisions.

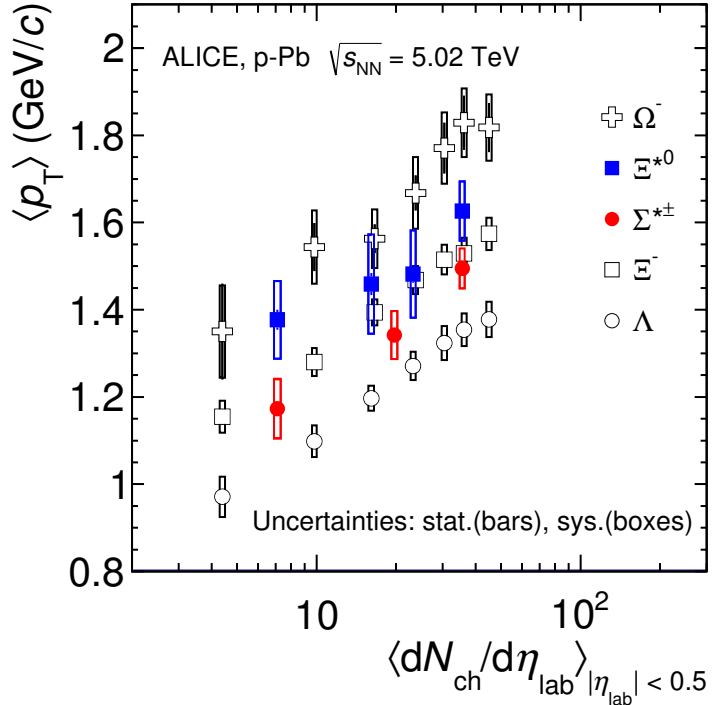


Figure 51: Mean transverse momenta $\langle p_T \rangle$ of Λ , Ξ^- , $\Sigma^{*\pm}$, Ξ^{*0} and Ω^- in p-Pb collisions at $\sqrt{s_{\text{NN}}} = 5.02$ TeV as a function of mean charged-particle multiplicity density $\langle dN_{\text{ch}}/d\eta_{\text{lab}} \rangle$, measured in the pseudorapidity range $|\eta_{\text{lab}}| < 0.5$. The results for Λ , Ξ^- and Ω^- are taken from [4, 5, 6]. Statistical and systematic uncertainties are represented as bars and boxes, respectively. The Ω^- and Ξ^- points in the 3rd and 4th lowest multiplicity bins are slightly displaced along the abscissa to avoid superposition with the $\Xi(1530)^0$ points.

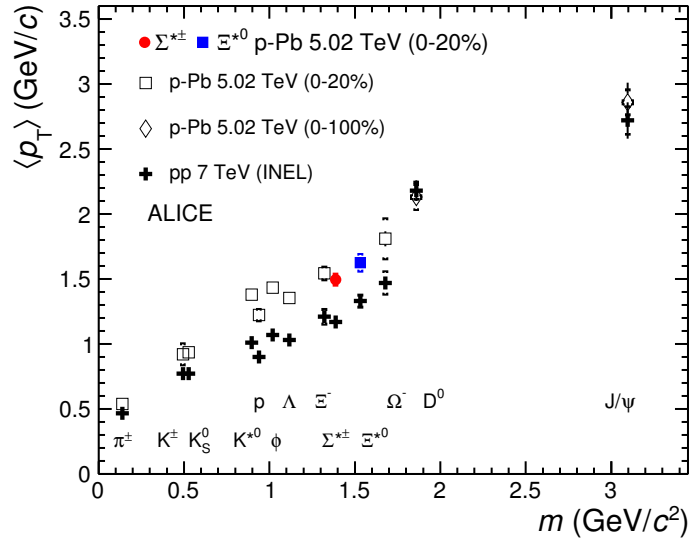


Figure 52: Mass dependence of the mean transverse momenta of identified particles for the 0 – 20% V0A multiplicity class and with $-0.5 < |y_{\text{CMS}}| < 0$ in p–Pb collisions at $\sqrt{s_{\text{NN}}} = 5.02$ TeV [4, 6], and in minimum-bias pp collisions at $\sqrt{s} = 7$ TeV [7] with $|y_{\text{CMS}}| < 0.5$. Additionally, D^0 and J/ψ results are plotted. The D^0 and J/ψ were measured in different rapidity ranges: $|y_{\text{CMS}}| < 0.5$ [8] ($|y_{\text{CMS}}| < 0.9$ [9]) for D^0 (J/ψ) in pp and $-0.96 < |y_{\text{CMS}}| < 0.04$ [8] ($-1.37 < |y_{\text{CMS}}| < 0.43$ [10]) for D^0 (J/ψ) in p–Pb. Note also that the results for D^0 and J/ψ in p–Pb collisions are for the 0–100% multiplicity class.

1298 Furthermore, for the light-flavour hadrons, the mean transverse momenta in p–Pb col-
1299 lisions are observed to be consistently higher than those in pp collisions at 7 TeV. The
1300 situation for the charm hadrons is different, where $\langle p_T \rangle$ appears compatible between both
1301 colliding systems. The discrepancy is likely due to different production mechanisms for
1302 heavy and light flavours and to a harder fragmentation of charm quarks. Specifically, the
1303 fact that $\langle p_T \rangle$ remains similar in pp and in p–Pb is consistent with an $R_{p\text{Pb}}$ ratio com-
1304 patible with unity at all p_T [8] for D^0 , and/or with the effects of shadowing in p–Pb which
1305 reduces the production at low p_T and thus increasing the overall $\langle p_T \rangle$ for J/ψ [10]; the
1306 small p_T hardening expected in pp when going from 5.02 to 7TeV is apparently not enough
1307 to counter-balance the situation.

1308 Because of small decrease of the $\langle p_T \rangle$ for proton and Λ relative to those for K^{*0} and
1309 ϕ , two different trends for mesons and baryons have been suggested [51]. Even including
1310 D^0 and J/ψ , as shown in Figure 52, a different trend for mesons and baryons cannot be
1311 convincingly established.

1312 **6.2 Particle yield ratios**

1313 **6.2.1 Integrated yield ratios of excited to ground-state hadrons**

1314 The integrated yield ratios of excited to ground-state hyperons [52, 4, 7, 6] with the same
1315 strangeness content, for different collision systems and energies, are shown in Figure 53
1316 as a function of system size. The ratio of $\Xi(1530)^0$ to Ξ is flat across the system and
1317 it complements the information derived from other resonance measurement for different
1318 lifetime which are shown in Figure 54.

1319 The short-lived resonances(ρ , K^* and Λ^*) which exhibit suppression from peripheral to
1320 central lead-lead collisions and with respect to thermal model in central lead-lead collisions.
1321 Currently favored explanation of is dominance of elastic re-scattering of decay daughters
1322 over regeneration in the hadronic phase.

1323 The constant behavior of the yield ratios of excited to ground-state hyperons with same
1324 strangeness content ($\Xi(1530)^0$ and Φ) indicates that neither regeneration nor re-scattering
1325 dominates with increasing collision system size because of its longer-lifetime.

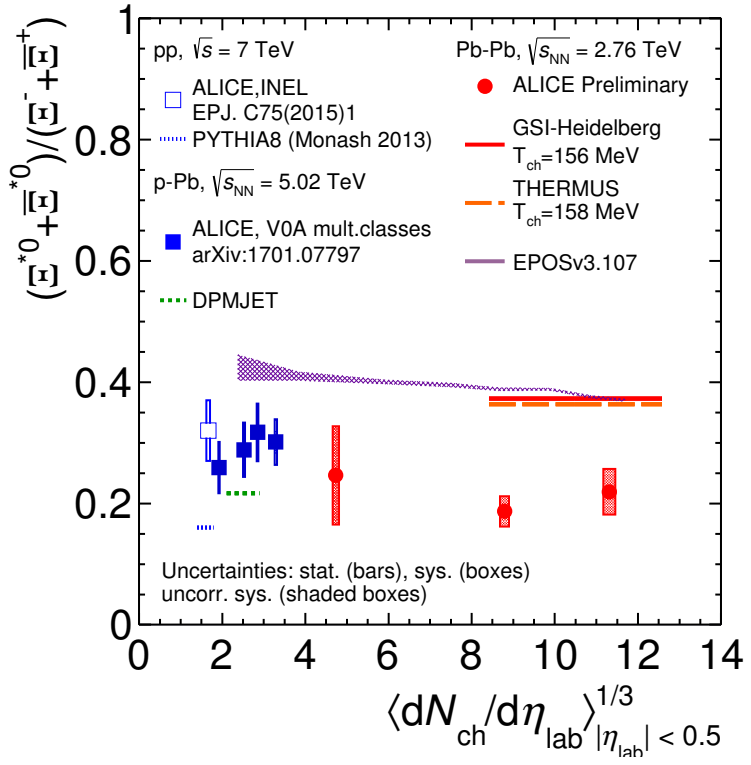


Figure 53: Ratio of $\Xi(1530)^0$ to Ξ^- measured in pp [7], p–Pb [4, 6] and Pb–Pb collisions as a function of $\langle dN_{ch}/d\eta_{lab} \rangle$ measured at midrapidity. Statistical uncertainties (bars) are shown as well as total systematic uncertainties (hollow boxes) and systematic uncertainties uncorrelated across multiplicity (shaded boxes). A few model predictions are also shown as lines at their appropriate abscissa.

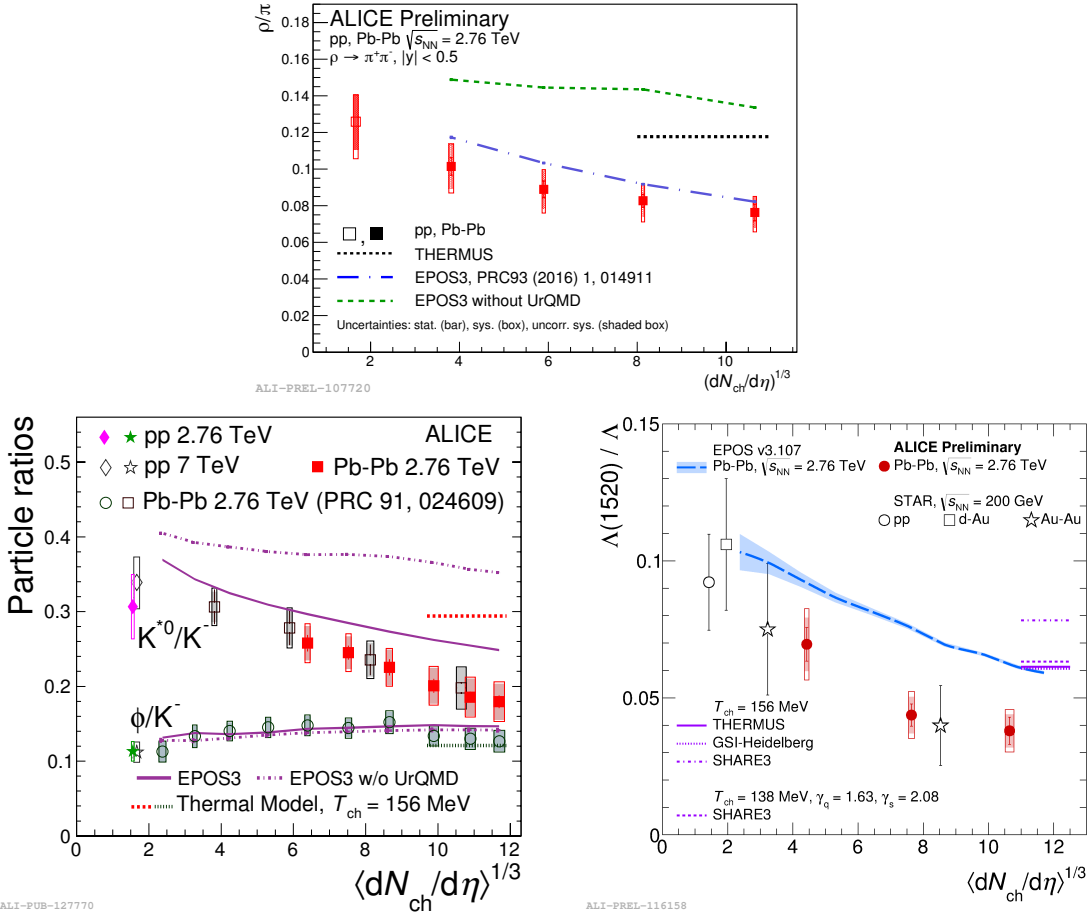


Figure 54: Ratio of ρ/π (Up), K^*/K , ϕ/K (Left bottom) and Λ^*/Λ with system size measured at mid-rapidity. Statistical uncertainties (bars) are shown as well as total systematic uncertainties (hollow boxes) and systematic uncertainties uncorrelated across multiplicity (shaded boxes). A few model predictions are also shown as lines at their appropriate abscissa.

1326 **6.3 Integrated yield ratios to pion**

1327 The integrated yield ratios of excited hyperons to pions are shown in Figure 55 to study
1328 the evolution of relative strangeness production yields with increasing collision system
1329 size. The ratio of $\Xi(1530)^0$ to Ξ is observed to be increase from pp to p–Pb collisions
1330 system and then, decrease from peripheral to central Pb–Pb collision. The QCD-inspired
1331 predictions like PYTHIA for pp [53] and DPMJET for p–Pb [46] clearly underestimate
1332 the observed yield ratios, while the statistical one seems to be comparable with results
1333 from high multiplicity in p–Pb but the ratio in Pb–Pb is below with respect to the model.
1334 The results in pp and p–Pb collisions are consistent with previous observation of ground-
1335 state hyperons to pion ratios. The Figure 56 presents particle yield ratios to pions of
1336 strange and multi-strange hadrons normalized to the values measured in pp collisions. As
1337 shown in the Figure 56, the $\Xi(1530)^0$ to pion ratios follow the trend of $\Xi \pi$ as function of
1338 $\langle dN_{ch}/d\eta_{lab} \rangle$ and indicate that the strangeness enhancement observed in p–Pb collisions
1339 depends predominantly on the strangeness content, rather than on the hyperon mass.

1340 The Figure 57 also shows the hyperon-to-pion ratios and compared with model predic-
1341 tions. The

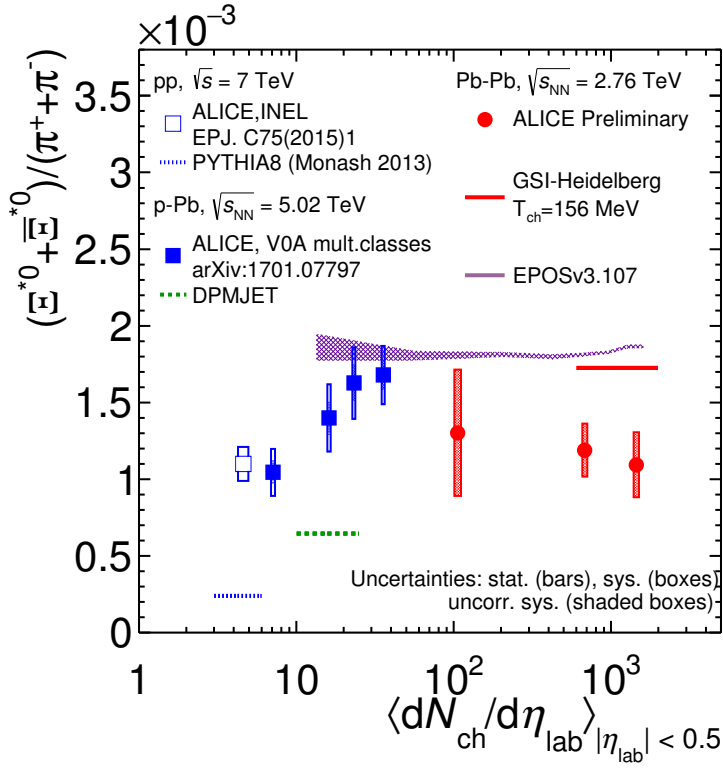


Figure 55: Ratio of $\Xi(1530)^0$ to π^\pm , measured in pp [11] and p–Pb [7] collisions, as a function of the average charged particle density ($\langle dN_{\text{ch}}/d\eta_{\text{lab}} \rangle$) measured at mid-rapidity. Statistical uncertainties (bars) are shown as well as total systematic uncertainties (hollow boxes) and systematic uncertainties uncorrelated across multiplicity (shaded boxes). A few model predictions are also shown as lines at their appropriate abscissa.

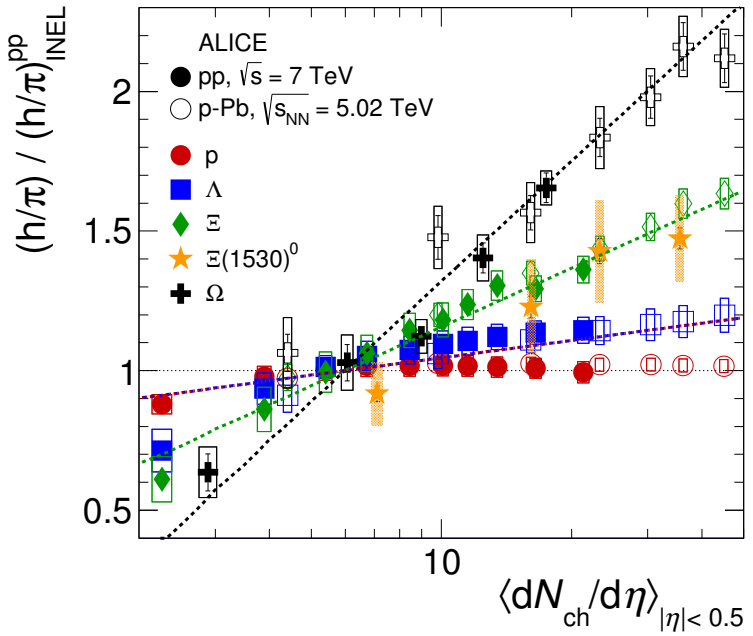


Figure 56: Particle yield ratios to pions of strange and multi-strange hadrons normalized to the values measured in pp collisions, both in pp and in p–Pb collisions. The common systematic uncertainties cancel in the double-ratio. The empty boxes represent the remaining uncorrelated uncertainties. The lines represent a simultaneous fit of the results with the empirical scaling formula in Equation ??.

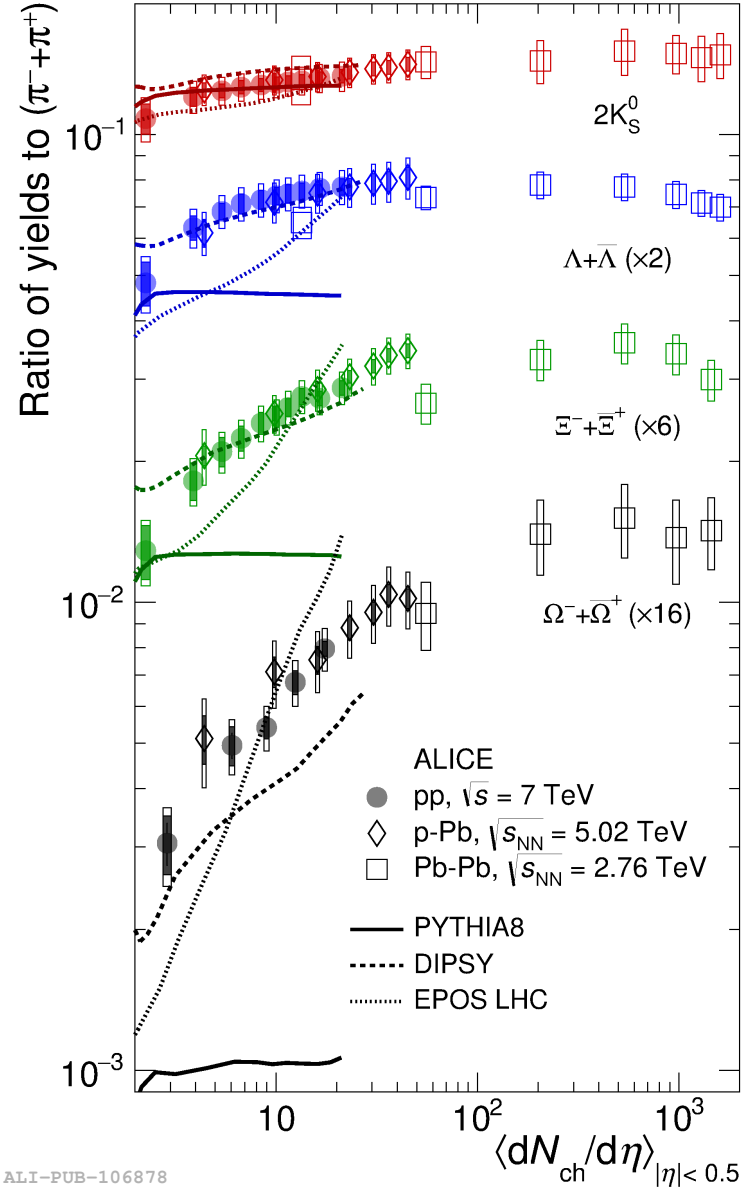


Figure 57: p_T -integrated yield ratios of strange and multi-strange hadrons to $(\pi^+ + \pi^-)$ as a function of $\langle dN_{ch}/d\eta_{lab} \rangle$ measured in the rapidity interval $|\eta| < 0.5$. The empty and dark-shaded boxes show the total systematic uncertainty and the contribution uncorrelated across multiplicity bins, respectively. The values are compared to calculations from MC models and to results obtained in Pb–Pb and p–Pb collisions at the LHC.

1342 **References**

- 1343 [1] **Particle Data Group** Collaboration, K. Olive *et al.*, “Review of Particle Physics,”
1344 *Chin. Phys. C***38** (2014) 090001.
- 1345 [2] “TE-EPC-LPC LHC units,”.
1346 <http://te-epc-lpc.web.cern.ch/te-epc-lpc/machines/lhc/general.stm>.
- 1347 [3] **ALICE** Collaboration, K. e. a. Aamodt, “Alignment of the ALICE Inner Tracking
1348 System with cosmic-ray tracks,” *JINST* **5** (2010) P03003.
- 1349 [4] **ALICE** Collaboration, J. Adam *et al.*, “Multiplicity dependence of pion, kaon,
1350 proton and lambda production in p–Pb collisions at $\sqrt{s_{NN}}= 5.02$ TeV,” *Phys. Lett.*
1351 **B728** (2014) 25–38, [arXiv:1307.6796](https://arxiv.org/abs/1307.6796) [nucl-ex].
- 1352 [5] **ALICE** Collaboration, J. Adam *et al.*, “Production of $K^*(892)^0$ and $\phi(1020)$ in
1353 p–Pb collisions at $\sqrt{s_{NN}}= 5.02$ TeV,” *Eur. Phys. J.* **C76** (2016) 245,
1354 [arXiv:1601.7868](https://arxiv.org/abs/1601.7868) [nucl-ex].
- 1355 [6] **ALICE** Collaboration, J. Adam *et al.*, “Multi-strange baryon production in p–Pb
1356 collisions at $\sqrt{s_{NN}}= 5.02$ TeV,” *Phys. Lett.* **B758** (2016) 389–401,
1357 [arXiv:1512.07227](https://arxiv.org/abs/1512.07227) [nucl-ex].
- 1358 [7] **ALICE** Collaboration, B. Abelev *et al.*, “Production of $\Sigma(1385)^{\pm}$ and $\Xi(1530)^0$ in
1359 proton-proton collisions at $\sqrt{s}= 7$ TeV,” *Eur. Phys. J.* **C75** (2015) 1,
1360 [arXiv:1406.3206](https://arxiv.org/abs/1406.3206) [nucl-ex].
- 1361 [8] **ALICE** Collaboration, J. Adam *et al.*, “ D -meson production in p–Pb collisions at
1362 $\sqrt{s_{NN}}= 5.02$ TeV and in pp collisions at $\sqrt{s}= 7$ TeV,” *Phys. Rev. C* **94** (2016)
1363 054908, [arXiv:1605.07569](https://arxiv.org/abs/1605.07569) [nucl-ex].
- 1364 [9] **ALICE** Collaboration, B. Abelev *et al.*, “Inclusive J/ψ production in pp collisions
1365 at $\sqrt{s}= 2.76$ TeV,” *Phys. Lett.* **B718** (2012) 295–306, [arXiv:1203.3641](https://arxiv.org/abs/1203.3641) [hep-ex].
- 1366 [10] **ALICE** Collaboration, J. Adam *et al.*, “Rapidity and transverse-momentum
1367 dependence of the inclusive J/ψ nuclear modification factor in p–Pb collisions at
1368 $\sqrt{s_{NN}}= 5.02$ TeV,” *JHEP* **06** (2015) 55, [arXiv:1503.07179](https://arxiv.org/abs/1503.07179) [nucl-ex].
- 1369 [11] **ALICE** Collaboration, J. Adam *et al.*, “Measurement of pion, kaon and proton
1370 production in proton-proton collisions at $\sqrt{s}= 7$ TeV,” *Eur. Phys. J.* **C75** (2015)
1371 226, [arXiv:1504.00024](https://arxiv.org/abs/1504.00024) [nucl-ex].
- 1372 [12] F. Halzen and A. Martin, “Quarks and Leptons: an introductory course in modern
1373 particle physics,” *By John Wiley and Sons* (1984) .

- 1374 [13] S. Wheaton, J. Cleymans, and M. Hauer, “THERMUS: A Thermal model package
 1375 for ROOT,” *Comput. Phys. Commun.* **180** (2009) 84–106, [arXiv:hep-ph/0407174](https://arxiv.org/abs/hep-ph/0407174)
 1376 [[hep-ph](#)].
- 1377 [14] J. Cleymans, S. Kabana, I. Kraus, H. Oeschler, K. Redlich, and N. Sharma,
 1378 “Antimatter production in proton-proton and heavy-ion collisions at ultrarelativistic
 1379 energies,” *Phys. Rev.* **C84** (2011) 054916, [arXiv:1105.3719](https://arxiv.org/abs/1105.3719) [[hep-ph](#)].
- 1380 [15] S. O. T. P. K. W. H.J. Drescher, M. Hladik, “Parton-Based Gribov-Regge Theory,”
 1381 *Phys. Rept.* **350** (2001) 93–289, [hep-ph/0007198](https://arxiv.org/abs/hep-ph/0007198).
- 1382 [16] T. P. M. B. K. M. K. Werner, Iu. Karpenko, “Event-by-event simulation of the
 1383 three-dimensional hydrodynamic evolution from flux tube initial conditions in
 1384 ultrarelativistic heavy ion collisions,” *Phys. Rev.* **C82** (2010) 044904.
- 1385 [17] I. K. T. P. K. Werner, B. Guiot, “Analyzing radial flow features in p-Pb and p-p
 1386 collisions at several TeV by studying identified-particle production with the event
 1387 generator EPOS3,” *Phys. Rev.* **C89** (2014) 064903.
- 1388 [18] K. Werner., “Analyzing radial flow features in p-Pb and p-p collisions at several TeV
 1389 by studying identified-particle production with the event generator EPOS3,” *Phys.
 1390 Rev. Lett.* **98** (2007) 152301.
- 1391 [19] S. B. et al., “Microscopic Models for Ultrarelativistic Heavy Ion Collisions,” *Prog.
 1392 Part. Nucl. Phys.* **41** (1998) 255.
- 1393 [20] M. B. et al., “Relativistic Hadron-Hadron Collisions in the Ultra-Relativistic
 1394 Quantum Molecular Dynamics Model,” *J. Phys.* **G25** (1999) 1859–1896.
- 1395 [21] M. Gell-Mann and Y. Ne’eman, “The Eightfold Way,” *By W.A. Benjamin* (1964) .
- 1396 [22] J. Rafelski and B. Mller, “Strangeness Production in the Quark-Gluon Plasma,”
 1397 *Phys. Rev. Lett* **48** (1982) 1066–1069.
- 1398 [23] **ALICE** Collaboration, B. Abelev *et al.*, “Multi-strange baryon production at
 1399 mid-rapidity in Pb–Pb collisions at $\sqrt{s_{\text{NN}}}= 2.76 \text{ TeV}$,” *Phys. Lett.* **B728** (2014)
 1400 216–227, [arXiv:1307.5543](https://arxiv.org/abs/1307.5543) [[nucl-ex](#)].
- 1401 [24] L. Evans and P. Bryant, “LHC Machine,” *JINST* **3** (2008) S08001.
- 1402 [25] “ALICE Technical Proposal,” *In CERN-LHCC-95-71* (1995) .
- 1403 [26] “ATLAS Technical Proposal,” *In CERN-LHCC-94-43* (1994) .
- 1404 [27] “CMS Technical Proposal,” *In CERN-LHCC-94-38* (1994) .

- 1405 [28] “LHCb Technical Proposal,” *In CERN-LHCC-98-004* (1998) .
- 1406 [29] “Technical Proposal for CERN LHCf Experiment,” *In CERN-LHCC-05-032* (2005) .
- 1407 [30] “Total Cross Section, Elastic Scattering and Diffraction Dissociation at the LHC,”
1408 *In CERN-LHCC-99-007* (1999) .
- 1409 [31] **ALICE** Collaboration, K. Aamodt *et al.*, “The ALICE experiment at the CERN
1410 LHC,” *JINST* **3** (2008) S08002.
- 1411 [32] **ALICE** Collaboration, L. B. et al, “Definition of the ALICE coordinate system and
1412 basic rules for sub-detector components numbering,” *In Internal Note
1413 ALICE-INT-2003-038* (2003) .
- 1414 [33] **ALICE** Collaboration, J. e. a. Alme, “The ALICE TPC, a large 3-dimensional
1415 tracking device with fast readout for ultra-high multiplicity events,” *In Nuclear
1416 Instruments and Method in Physics Research* **A622** (2010) 316–367.
- 1417 [34] “Technical Design Report on Forward Detectors: FMD, T0 and VZERO,” *In
1418 CERN-LHCC-2004-025* (2004) .
- 1419 [35] R. Glauber, “Lectures in Theoretical Physics,” *By Interscience Publishers.* **1** (1959)
1420 315.
- 1421 [36] A. S. K.C. Chung, C.S. Whang and G. Pech, “Transverse and forward energy
1422 distributions in untra-relativistic heavy-ion collisions by an absorption model,”
1423 *Physics Review* **C57** (1998) 847–856.
- 1424 [37] **ALICE** Collaboration, J. Adam *et al.*, “Centrality dependence of particle
1425 production in p–Pb collisions at $\sqrt{s_{\text{NN}}}= 5.02 \text{ TeV}$,” *Phys. Rev.* **C91** (2015) 064905,
1426 [arXiv:1412.6828 \[nucl-ex\]](https://arxiv.org/abs/1412.6828).
- 1427 [38] **ALICE** Collaboration, B. Abelev *et al.*, “Centrality determination of Pb–Pb
1428 collisions at $\sqrt{s_{\text{NN}}}= 2.76 \text{ TeV}$ with ALICE,” *Phys. Rev.* **C88** (2013) ,
1429 [arXiv:1303.0737 \[nucl-ex\]](https://arxiv.org/abs/1303.0737).
- 1430 [39] “ALICE Technical Design Report of the Trigger, Data Acquisition, High-Level
1431 Trigger, Control system,” *In CERN-LHCC-2003-062.* (2003) .
- 1432 [40] “The Grid - Blueprint for a New Computing Infrastructure,” *By Morgan Kaufmann
1433 Publishers.* (1999) .
- 1434 [41] e. a. Bagnasco. S, “AliEn: ALICE Environment on the GRID,” *In Jounal of Physics:
1435 Conference Series* **119** (2008) n.062012.

- 1436 [42] R. Brun and F. Rademakers, “ROOT - An object oriented data analysis framework,”
 1437 *In Nuclear Instrument and Methods in Physics Research Section A* **389** (1997)
 1438 81–86.
- 1439 [43] **ALICE** Collaboration, B. Abelev *et al.*, “Performance of the ALICE Experiment at
 1440 the CERN LHC,” *Int. J. Mod. Phys. A* **29** (2014) 1430044, [arXiv:1402.4476](#)
 1441 [nucl-ex].
- 1442 [44] **ALICE** Collaboration, B. Abelev *et al.*, “Pseudorapidity Density of Charged
 1443 Particles in p–Pb Collisions at $\sqrt{s_{\text{NN}}}= 5.02$ TeV,” *Phys. Rev. Lett.* **110** (2013)
 1444 032301, [arXiv:1210.3615](#) [nucl-ex].
- 1445 [45] **ALICE** Collaboration, K. Aamodt *et al.*, “Strange particle production in
 1446 proton-proton collisions at $\sqrt{s}= 0.9$ TeV with ALICE at the LHC,” *Eur. Phys. J.*
 1447 **C71** (2011) 1594, [arXiv:1012.3257](#) [nucl-ex].
- 1448 [46] S. Roesler, R. Engel, , and J. Ranft, “The Monte Carlo Event Generator
 1449 DPMJET-III, Advanced Monte Carlo for Radiation Physics, Particle Transport
 1450 Simulation and Applications,” *Conference Proceedings, MC2000, Lisbon, Portugal,*
 1451 October 23–26 (2000) 1033–1038, [hep-ph/0012252](#).
- 1452 [47] R. Brun, F. Carminati, and S. Giani, “GEANT detector description and simulation
 1453 tool,” *CERN-W5013* (1994) .
- 1454 [48] R. Barlow, “Systematic Errors: Facts and Fictions,” *Presented at Advanced*
 1455 *Statistical Techniques in HEP, Durham, March 2002* (2002) 333p,
 1456 [hep-ex/0207026v1](#).
- 1457 [49] **ALICE** Collaboration, B. Abelev *et al.*, “Centrality dependence of π , K and p
 1458 production in Pb–Pb collisions at $\sqrt{s_{\text{NN}}}= 2.76$ TeV,” *Phys. Rev. C* **88** (2013) ,
 1459 [arXiv:1301.4361](#) [nucl-ex].
- 1460 [50] **STAR** Collaboration, B. I. Abelev *et al.*, “Hadronic resonance production in d–Au
 1461 collisions at $\sqrt{s_{\text{NN}}}= 200$ GeV measured at the BNL Relativistic Heavy-Ion Collider,”
 1462 *Phys. Rev. C* **78** (2008) 044906, [arXiv:0801.0450](#) [nucl-ex].
- 1463 [51] A. Velásquez, “Mean p_{T} scaling with m/n_q at the LHC: Absence of (hydro) flow in
 1464 small systems?,” *Nucl. Phys. A* **943** (2015) 9–17, [arXiv:1506.00584](#) [hep-ph].
- 1465 [52] **ALICE** Collaboration, B. Abelev *et al.*, “Multi-strange baryon production in pp
 1466 collisions at $\sqrt{s}= 7$ TeV with ALICE,” *Phys. Lett. B* **712** (2012) 309,
 1467 [arXiv:1204.0282](#) [nucl-ex].
- 1468 [53] T. Sjöstrand, S. Mrenna, and P. Skands, “A brief introduction to PYTHIA 8.1,”
 1469 *Comput. Phys. Comm.* **178** (2008) 852–867, [arXiv:0710.3820](#) [hep-ph].

¹⁴⁷⁰ **Acknowledgements**